UNIVERSITY OF SOUTHAMPTON

Faculty of Engineering and Physical Science

Optoelectronics Research Centre

Ultrafast Thulium-Doped Fibre Laser for Healthcare Applications

by

Panuwat Srisamran

ORCID ID 0009-0003-2796-4168

A thesis for the degree of Doctor of Philosophy

09 July 2025

UNIVERSITY OF SOUTHAMPTON

Abstract

Faculty of Engineering and Physical Science

Optoelectronics Research Centre

Doctor of Philosophy

Ultrafast Thulium-Doped Fibre Laser for Healthcare Applications

by Panuwat Srisamran

The short-wavelength infrared (SWIR) window, with wavelengths ranging from ~1650 to 1900 nm, provides outstanding performance in deep tissue, non-invasive biomedical detection applications, thanks to its high optical transparency and low scattering loss in most biomedical samples. The SWIR can be utilised in multiphoton microscopy (MPM) to acquire high-resolution biomedical images with superior signal-to-background ratios. However, MPM relies on detecting nonlinear scattering signals that require a high-peak-power pump source. Therefore, reliable sources with appropriate optical properties are essential to manifest high-performance, deep-penetration detection in biomedical samples. Ultrafast SWIR pulses, with a temporal width in the hundreds of fs regime, hold high potential to function as pumps in the MPM due to their capabilities to deliver high peak powers, while average powers are kept at low levels, preventing tissue heating issues. Mode-locked (ML) thulium-doped fibre (TDF) lasers (ML-TDFLs) are promising options for generating ultrafast SWIR pulses.

In this thesis, ML-TDFLs with different cavity designs are presented. I have successfully demonstrated an all-fiberised ML-TDFL enabled by a semiconductor saturable absorber mirror (SESAM). This cavity generates a stable dissipative-soliton ML operation at a central wavelength of 1875 nm and delivers a pulse energy of 10.3 nJ with a compressed pulse duration of 548 fs. To mitigate the wavelength limitation from the SESAM, I developed another all-fiberised ML-TDFL based on carbon nanotubes (CNTs) saturable absorber (SA). This cavity offers a single-pulse ML operation at a central wavelength of 1847 nm and generates a compressed pulse duration of 381 fs. The cavity has been deployed as a seed laser in an imaging laser system, utilised an efficient pump source in biomedical imaging experiments. Moreover, I have successfully developed an all-fiberised ML-TDFL in an all-polarisation-maintaining (all-PM) configuration that enhances cavity robustness and supports a 'turnkey' laser design. Several advanced techniques have been integrated into the cavity to realise the balance of both conservative effects (between dispersion and nonlinearity) and dissipative effects (between gain and loss), to facilitate the dissipative-soliton operation. This all-PM cavity generates a self-start, stable ML operation at a central wavelength of 1876 nm with a pulse energy of 1.1 nJ and a compressed pulse duration of

391 fs. The mode-locking can be stably maintained in a normal laboratory environment for significantly extended period without requiring any active controlling mechanisms. Additionally, an all-fiberised PM chirped pulse amplification (CPA) system seeded by such all-PM ML cavity has been developed and deployed as an imaging laser prototype. This laser system operates at a central wavelength of 1840 nm and produces an output pulse energy of ~40 nJ (an average power of ~600 mW) with a compressed pulse duration of 493 fs. The laser has been delivered to our external project partner and been utilised as a reliable laser source in biomedical imaging experiments. Finally, the study of an all-PM ML-TDFL has been further explored in a cavity enabled by a nonlinear amplifying loop mirror (NALM) SA. The cavity provides stable dissipative-soliton ML operation at a central wavelength of 1860 nm with a pulse energy of 1.5 nJ and a compressed pulse duration of 539 fs. This all-fibre cavity demonstrates the possible solution to resolve any technical difficulties of using material-based SAs.

Table of Contents

List of Figures

List of Tables

Research Thesis: Declaration of Authorship

Print name: Panuwat Srisamran

Title of thesis: Ultrafast Thulium-Doped Fibre Laser for Healthcare Applications

I declare that this thesis and the work presented in it are my own and has been generated by me as the result of my own original research.

I confirm that:

1. This work was done wholly or mainly while in candidature for a research degree at this University;
2. Where any part of this thesis has previously been submitted for a degree or any other qualification at this University or any other institution, this has been clearly stated;
3. Where I have consulted the published work of others, this is always clearly attributed;
4. Where I have quoted from the work of others, the source is always given. With the exception of such quotations, this thesis is entirely my own work;
5. I have acknowledged all main sources of help;
6. Where the thesis is based on work done by myself jointly with others, I have made clear exactly what was done by others and what I have contributed myself;
7. Parts of this work have been published as the journal and conference publications listed in List of publications (in Chapter 8)

Signature: ..... Date:.....

Acknowledgements

The four-year ‘journey’ as a PhD student at the ORC has been an unforgettable experience of my lifetime. I really appreciated all the help that supports my study in ultrafast fibre lasers, which will be a cornerstone for my career path.

I would like to express my deepest gratitude to my supervisors, Dr. Lin Xu, Dr. Yongmin Jung, and Prof. David Richardson. Dr. Lin Xu, as the main supervisor, has been the most important person throughout my PhD journey. He has always been available to discuss, support, and answer my questions. He provides not only technical support with his wealth of knowledge and experience in this research field but also guidance through many issues I encountered in my PhD study. Dr. Yongmin Jung, as my co-supervisor, always provides valuable feedback and suggestions to my research with his wealth of expertise that refining my PhD project. Prof. David Richardson provided invaluable guidance and support with his vast knowledge. He also shared his experience guiding my PhD journey, especially in the first year of my PhD. I really appreciated their time and determination to help me develop my research skills.

I would like to express my gratitude to the members of my research group at the ORC. They were great colleagues who provided a supportive environment for my research and were always willing to help with any problems I encountered. I greatly appreciated my time spent with them over these four years. Additionally, I would like to express my gratitude to members of the ‘2-μm laser team’ including Duanyang Xu, Ibrahim Abughazaleh, and Matthew Gerard. Duanyang Xu, as a former PhD student, always kindly provided his support to my research, especially at the start of my PhD. Ibrahim Abughazaleh and Matthew Gerard are the team members that always available to ask for help and make the PhD experience more enjoyable. I also would like to extend my thanks to other colleagues at the ORC who have helped me either directly or indirectly.

I would like to express my sincere gratitude to members of the research group at Cambridge Graphene Centre (CGC), University of Cambridge, Prof. Andrea C. Ferrari, Dr. Jing He, Dr. Boyang Mao, and Dr. Jeremiah Marcellino who have kindly provided the carbon nanotubes saturable absorbers that can be used to develop mode-locked lasers. Furthermore, they also provided supports, contributions, and feedback on my research to report the manuscript entitled *“Nanojoule-energy-level, polarization-maintaining, dissipative-soliton mode-locked thulium fiber laser at 1876 nm”*.

Special thanks to my Thai friends in Southampton who made this four-year time ‘feel like home’. I would like to extend this gratefulness to my family in Thailand that always been there anytime I needed them.

Finally, I would like to acknowledge the Development and Promotion of Science and Technology Talents Project (DPST), Royal Thai Government for the financial support through my PhD study at the University of Southampton. I also extend my gratitude to the staffs at the Royal Thai Embassy, London for their support and always being helpful.

List of Abbreviations

ACF	Autocorrelation function
AOM	Acousto-optic modulator
ASE	Amplified spontaneous emission
CFBG	Chirped fibre Bragg grating
CIR	Circulator
CNTs	Carbon nanotubes
CPA	Chirped pulse amplification
CW	Continuous-wave
DBR	Distributed Bragg reflector
DCF	Dispersion compensating fibre
EDF	Erbium-doped fibre
EDFA	Erbium-doped master oscillator fibre amplifier
EDFL	Erbium-doped fibre laser
FBG	Fibre Bragg grating
FSR	Free-spectral range
FWHM	Full width at half-maximum
GDD	Group delay dispersion
GVD	Group velocity dispersion
HWP	Half-waveplate
ISO	Isolator
LD	Laser diode
LF	Lyot filter
ML	Mode-locked
ML-TDFL	Mode-locked thulium-doped fibre laser

MMF	Multimode fibre
MOFA	Master oscillator fibre amplifier
MPM	Multiphoton microscopy
MQW	Multiple Quantum well
MRI	Magnetic resonance imaging
NA	Numerical aperture
NALM	Nonlinear amplifying loop mirror
NLSE	Nonlinear Schrödinger equation
NOLM	Nonlinear optical loop mirror
NPR	Nonlinear polarisation rotation
OC	Output coupler
OSA	Optical spectrum analyser
OSNR	Optical signal-to-noise ratio
PC	Polarisation controller
PM	Polarisation-maintaining
PM-DCF	Polarisation-maintaining dispersion compensating fibre
PM-ISO	Polarisation-maintaining isolator
PM-OC	Polarisation-maintaining output coupler
PM-SMF	Polarisation-maintaining single-mode fibre
PM-TDF	Polarisation-maintaining thulium-doped fibre
PM-WDM	Polarisation-maintaining wavelength-division-multiplexer
RF	Radio frequency
SA	Saturable absorber
SESAM	Semiconductor saturable absorber mirror
SMF	Single-mode fibre

SNR	Signal-to-noise ratio
SPM	Self-phase modulation
SSFS	Soliton self-frequency shift
SWIR	Short-wavelength infrared
SWNTs	single-wall carbon nanotubes
TBP	Time-bandwidth product
TC	Tuneable coupler
TDF	Thulium-doped fibre
TDFA	Thulium-doped fibre amplifier
UHNA	Ultra-high numerical aperture
UR	Unidirectional ring
WDM	Wavelength-division multiplexer

Chapter 1 Introduction

In this chapter, I explain the research area in the first section. The research motivation is discussed in the second section, and the final section gives an overview of the thesis structure.

1.1 Research area

Laser sources operating at 2-μm wavelengths have gained increasing interest in the laser engineering research community over the past decades due to their capabilities to support various applications [1]. For example, 2-μm lasers can be developed for applications in spectroscopy [2, 3] and LIDAR (Light Detection And Ranging) [4, 5] or using corresponding absorptions of atmospheric gases near 2 μm in environmental detections [6]. Moreover, these lasers can be developed to generate high output powers and demonstrate their applications in material processing or micromachining [7, 8]. One of the outstanding applications of 2-μm lasers is in biomedical applications [1, 9]. Figure 1.1 presents the wavelength-dependent attenuation coefficient of biomedical samples, revealing the highest optical transparency in the short-wavelength infrared window (SWIR: ~1650-1900 nm) [10, 11]. Different biomedical applications can be supported based on the central wavelength of the laser within this 2-μm region. For instance, the laser with a wavelength near water (O-H) absorption peak at ~1930 nm has the potential to enable applications in surgery [12, 13] and laser lithotripsy [14, 15]. In contrast, several lasers have been developed to operate in the SWIR wavelengths, away from the water absorption peak, and support nonlinear imaging applications due to their nature of having long penetration depth in the biomedical samples. For instance, ultrashort pulses of ~100 fs at a wavelength of ~1675 nm have demonstrated an outstanding performance in acquiring multiphoton microscopy (MPM) at penetration depths in the mm scale [10]. Another 1820 nm ultrashort pulse with a duration of 150 fs has reported its function as a light source for 3-photon fluorescence microscopy [16]. Recently, our research group have reported an achievement of using an all-fiberised ML-TDFL, generating ultrashort pulses at 1840 nm with a pulse duration of 416 fs [17]. The laser has demonstrated an outstanding performance in generating high-resolution images of complex biomedical samples, using the third-harmonic generation microscopy technique. In summary, high-performance biomedical imaging can be achieved, utilising ultrafast SWIR pulses. However, the laser source must be carefully designed to provide appropriate pulse properties, i.e., operating wavelength, pulse energy, and pulse duration.

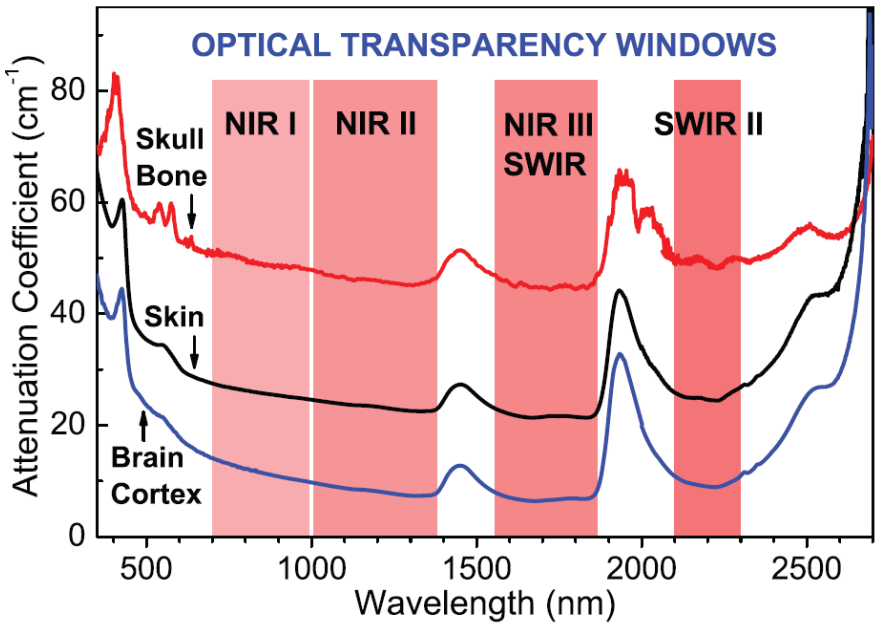

Figure 1.1 Optical transparency windows of biomedical samples. This figure has been reproduced from [11], permission granted. © 2018 WILEY-VCH Verlag GmbH & Co. KGaA, Weinheim.

Mode-locked (ML) thulium-doped fibre (TDF) lasers (ML-TDFLs) are promising options to generate ultrafast pulses at the SWIR wavelengths, corresponding to the broad emission bandwidth of the TDF spanning from ~1650-2100 nm [18]. ML-TDFLs have demonstrated their capabilities to generate ultrashort pulses with widely-tuneable central wavelengths [19, 20]. In ML-TDFLs, output pulse properties can be controlled by managing the detailed dispersion map in the cavity [21]. Generally, single-mode silica fibres have anomalous dispersion at wavelengths beyond 1.3 μm [22]. Therefore, ML-TDFLs usually operate in an all-anomalous dispersion regime that facilitates conventional-soliton ML operation, generating with a balanced effect between the dispersion and nonlinearity in the cavities [21, 23]. Conventional-soliton ML-TDFLs have been widely demonstrated with different cavity designs [24-33]. However, these cavities generate limited pulse energy in the pJ-level and the fs-level pulse duration. Additionally, conventional-soliton pulses encounter some technical limitations because of nonlinearities in amplifiers [3, 34-37]. Development of conventional soliton for higher pulse energies can be challenging [23]. Some conventional-soliton ML-TDFLs have been demonstrated using large-mode area fibres or special cavity designs to achieve high pulse energies [38-40]. However, these resulted in complex and cumbersome laser cavities. The limitation of conventional soliton can be settled by employing dispersion compensation fibres (DCFs) with normal dispersion into the cavity, managing the net cavity dispersion to be close to zero [41-43]. In this regime, the cavity can support a stretched pulse (also called 'dispersion-managed') ML operation, in which the oscillating pulse experiences a 'breathing effect' while propagating through these opposite dispersion fibres [21, 44, 45]. Consequently, Kelly sidebands can be suppressed, and the cavity can generate higher pulse energies approaching the nJ-level [46]. Output pulses from dispersion-managed cavities can have

different chirps, depending on the position of the output coupler [21]. Nevertheless, a pulse compressor can be employed to de-chirp the pulse back to the transform-limited value in the hundreds of fs level [47, 48]. ML-TDFLs have been widely demonstrated in the dispersion-managed regime, achieving excellent output pulse properties [49-55]. The pulse energy can be further increased in the net-normal-dispersion cavity, where the dissipative soliton can be realised [21]. In this ML regime, the oscillating pulses have higher tolerance to nonlinear phase accumulation [56], thereby enabling higher achievable pulse energies than other soliton types [57]. However, dissipative solitons require careful cavity design to facilitate the balance of both conservative effects (dispersion and nonlinearity) [58] and dissipative effects (spectral gain and loss) [59]. Such dissipative solitons can achieve nJ-energy-level pulses with positively-chirped pulses with few-picoseconds durations [21]. Accordingly, dissipative solitons also require pulse compressors to de-chirp the pulses back to the Fourier-transform limited value in the hundreds of fs regime. ML-TDFLs have been previously studied and demonstrated with dissipative solitons [19, 60-66]. An outstanding work has been reported in 2015, in which a net-normal-dispersion ML-TDFL generated output pulses at a central wavelength of 1925 nm with a pulse energy of 8 nJ [60]. The output pulses can be compressed down to 130 fs, equivalent to a high peak power of ~40 kW. However, this cavity consists of partially free-space components, which might pose a challenge for employment in practical applications. It is worth noting that dissipative-soliton ML-TDFL can be realised in all-normal-dispersion cavity, using fluoride fibres (ZBLAN) that have normal dispersion at 2-μm region [67]. By utilising ZBLAN fibres, stable ML operation can be realised at a central wavelength of 1833 nm with a pulse energy of 0.9 nJ and a compressed pulse duration of 107 fs [67]. However, these fluoride-glass fibres are hard to be developed for the fully-fiberised cavity due to the difficulties in splicing them to standard silica-glass fibre.

The dissipative-soliton pulses generally exhibit a positive chirp, which is suitable for a seed laser in a chirped pulse amplification (CPA) system to generate higher pulse energies. In CPA, the seed pulse is stretched in the temporal domain to reduce the peak power and to minimise the undesired nonlinear-induced effects during the amplification [68-70]. Thus, the pulse can be efficiently amplified to achieve high pulse energies. At the output end of the CPA system, the pulse duration can be de-chirped back to ultrashort pulse durations in the hundreds of fs-level with a compressor. This technique can produce a high-energy, ultrashort pulse at 2-μm wavelengths [71-74]. For instance, a 470-μJ pulse operating at a central wavelength ~1950 nm has been generated using a large-core (81 μm) TDF in the final amplifier in a semi-free space configuration [74]. The pulse has a compressed duration of 200 fs, therefore, equivalent to the peak power exceeding 2 GW. With a proper design, the CPA system can be developed in a compact, all-fiberised configuration and generate a high pulse energy of 1.25 μJ with a compressed pulse duration of 297 fs, yielding a peak power of 4.2 MW [72]. Recently, our group have reported an all-fiberised

laser system associated with the CPA technique to generate 105-nJ ultrashort pulse at 1840 nm with a compressed pulse duration of 416 fs, which has demonstrated outstanding performance in biomedical imaging experiments [17].

Saturable absorbers (SAs) are another key component that needs to be considered when designing the ML cavities. SAs create the ML initiation by eliminating low-intensity noise regarding to their nature of reduced optical loss at higher pulse intensity [75, 76]. SAs can be classified into two groups [77]. Material-based SAs provide saturable absorption using the intrinsic properties of their molecules [76], offering the ability to manipulate the optical properties, i.e., operating wavelength and modulation depth, by controlling their physical properties [32, 78]. However, material-based SAs encounter technical difficulties of having limited supporting wavelengths [79], low damage threshold [76], and long-term degradation [80]. These difficulties can be resolved in fibre-based SAs that supply intensity-dependent loss based on the Kerr-nonlinearity of oscillating pulses in optical fibres [81]. Technically, fibre-based SAs have high power handling and can function at any wavelength [82]. However, a major drawback of the fibre-based SA is the self-starting mechanism in which high pump powers are required to supply sufficient modulation depths and initiate pulse-mode operation [81, 83].

Cavity robustness is another key factor to be considered, especially in ML laser source design and engineering. Cavities with passive (non-polarisation-maintaining (non-PM)) fibres suffer from physical perturbations, i.e., temperature variation or mechanical stress. Consequently, such a fiberised ML cavity requires polarisation controllers (PCs) to start or maintain ML operation [21], which might pose challenges for practical applications. Robust, turnkey fiberised ML cavities utilising PM fibres/components are preferred. By intentionally applying stress across its core, PM fibres end up having high birefringence between two orthogonal optical axes named the ‘fast axis’ and the ‘slow axis’. Consequently, PM fibres have high tolerances to physical perturbations and can preserve the polarisation of the propagating light, aligning to the optical axis [84, 85]. Therefore, ML cavities with all-PM fibres/components are expected to have high robustness [86, 87]. All-PM dissipative-soliton ML cavities have been successfully demonstrated in the context of 1 μm [88, 89] and 1.5 μm [90, 91]. However, in the 2-μm window, it is still challenging to achieve dissipative solitons with all-PM fibres due to limited options for PM-DCFs [42, 47]. For example, a dissipative soliton has been demonstrated using a 3-m length of specially designed and in-house-fabricated PM-TDF to function as both gain and positive dispersion fibre in the cavity [92]. However, the laser operates at a central wavelength of 1995 nm and has a low output pulse energy of ~44 pJ due to high splicing losses between the PM-TDF and standard PM-SMFs. At present, developing all-PM dissipative soliton lasers with nJ-level-pulse-energy still poses a scientific challenging.

1.2 Research motivation

Non-invasive, high-accuracy medical diagnosis has been an important research topic in the past decades, as it is the key starting point for all other subsequential medical treatments. To date, several techniques have been employed in clinical trials to acquire crucial information, requiring an in-depth analysis that leads to successful medical treatments. For instance, X-ray imaging refers to a technique that illustrates topological images based on different absorption efficiencies of organs in the body [93, 94]. However, imaging contrast is greatly reduced once samples with similar absorption coefficients are scanned. Magnetic resonance imaging (MRI) is another already widely used detection technique used for medical diagnosis. By detecting the interaction of atoms to an external strong magnetic field, detailed images for medical diagnosis can be acquired [95]. However, this examination process can take a long time. Additionally, metallic objects are prohibited in the diagnosis room since they cause a failed scan. These limitations pose difficulties for the patients. Detecting the reflected echoes of high-frequency sound waves from organs can be used to acquire ultrasound scanning images [96]. However, the detection depth and contrast are lower than MRI [97]. Consequently, other rapid, accurate, non-invasive detection techniques are preferred.

Optical-based techniques are promising approaches for high-throughput biomedical scanning applications. For example, MPM offers high-resolution imaging in biomedical samples [98, 99]. The technique is based on the non-invasive, nonlinear interaction of samples in raster-scanned areas to pump photons. This technique has been widely used in biomedical research [100-106]. MPM detects nonlinear generated light that is generated with high peak-power pump signals. Therefore, this effect typically occurs near the focal point of the objective lens [98]. By utilizing longer wavelengths, MPM offers deep penetration distance and high signal-to-background ratios [107, 108]. Figure 1.1 presents the optical transparency of biomedical samples, revealing the lowest attenuation coefficient in the SWIR window [11], which improves power delivery and MPM efficiency [10].

In 2013, Horton *et al*. have demonstrated an achievement of MPM imaging at the mm-level penetration depth in biomedical samples [10]. Ultrashort (~100 fs) pulses at a central wavelength of 1675 nm have been generated via the soliton self-frequency shift (SSFS) of ML pulses at 1.5 μm, utilising nonlinear optical fibres. However, SSFS system needs to be carefully designed to maintain stable pulse energy and achieve high energy-conversion efficiency [109, 110]. ML-TDFL is another promising solution to generate ultrashort SWIR pulses due to the broad gain spectrum covering from ~1650-2100 nm [18]. Generally, ML-TDFLs have been demonstrated at central wavelengths beyond 1900 nm, in which Tm^{3+} -ions have high optical gain. For instance, a 8-nJ

pulse energy has been directly generated from the dissipative-soliton cavity at a central wavelength of 1925 nm and a pulse duration of ~130 fs [60]. Another ML-TDFL system, along with a CPA setup, has been demonstrated to generate ultrashort (297 fs) pulses with high energy exceeding 1.27 μJ at a central wavelength of 1925 nm [72]. However, wavelengths beyond 1900 nm tend to encounter a water (O-H) absorption peak [111]. Therefore, these pulses at long wavelengths are not suitable for deep penetration depth in tissue. Due to the quasi-three-level nature of TDFs, achieving high pulse energy in the SWIR wavelengths is challenging [112]. A ML-TDFL has been demonstrated at a central wavelength of 1746 nm and generates short pulse duration of ~370 fs, however, with a pulse energy of 0.2 nJ [19]. By incorporating pulse amplification techniques, ultrashort high-pulse energy with wavelength between 1700-1900 nm can be demonstrated. For instance, a 128-nJ pulse at a central wavelength of ~1766 nm and a duration of 174 fs has been demonstrated from a cavity with a W-type normal dispersion TDF [113]. However, this system requires specially designed fibres with a complex fabrication process. Another 1820-nm ML-TDFL has been demonstrated with a pulse energy of 1.1 μJ and been utilised as a light source for MPM in biomedical samples [16]. However, this laser system was based on fluoride-glass fibres, which are hard to connect to standard silica-glass fibres. Thus, this system ended up with a bulky cavity design and required free-space optical components. Recently, our group have reported an all-fiberised ML-TDFL with an operating wavelength of 1840 nm [17]. The ultrashort (416 fs) pulses with an energy of 105 nJ have demonstrated excellent performance in acquiring high-resolution MPM images from complex biomedical samples. However, the system was built on non-PM fibres which pose challenges for practical applications due to its sensitivity to physical perturbations.

In this thesis, I report on the development of ML-TDFLs that generate ultrashort pulses in the SWIR to support biomedical imaging applications, which aligns with one of the research goals of the InLightenUs project. I have demonstrated the generation of ultrafast SWIR pulses utilising an all-fiberised cavity design, exhibiting pulse energies exceeding 10 nJ. Additionally, I have explored different SAs to extend the capability of pulse generation at short wavelengths toward 1800 nm for a Tm-doped gain medium. ML-TDFL has been demonstrated using the carbon nanotube (CNT)-SAs, presenting a stable ML operation at a central wavelength of 1847 nm. This cavity was employed to provide seed pulses in a laser system that were delivered for biomedical imaging experiments. Another important part detailed in this thesis is the development of all-PM dissipative-soliton ML-TDFLs, in which the SWIR pulses can be generated with pulse energies exceeding the nJ-level. This all-PM cavity demonstrates an outstanding robustness with reliable output pulse properties. Further to this, I developed an 1840-nm all-PM ML-TDFL laser system, which is a robust, ‘turnkey’, laser system that has been delivered to be used as a light source in biomedical imaging, performed by an external project partner at the University of Nottingham.

Finally, I have demonstrated an all-PM ML-TDFL with a nonlinear amplifying loop mirror (NALM) to mitigate the limitations of previously used material-based SAs.

1.3 Thesis structure

This thesis is composed of 8 chapters.

Chapter 1 discusses the research area, research motivation, and the thesis structure.

Chapter 2 explains the related theories of thesis work. The topics cover a basic understanding of optical fibres, pulse propagation in optical fibres, passively mode-locked fibre laser, saturable absorbers, Lyot filter, dispersion management in the mode-locked cavity, and chirped-pulse amplification.

Chapter 3 presents the experiment to develop an all-fiberised ML-TDFL, enabled by a semiconductor saturable absorber mirror (SESAM). Detailed information on the experiment to achieve a pulse energy exceeding 10 nJ is explained, along with the relevant simulations to predict the dynamic pulse behaviours.

Chapter 4 describes the characterisation of carbon nanotubes (CNTs), which is another material-based SA that holds high potential for short-wavelength operation toward 1800 nm. This chapter also includes an experiment to develop an all-fiberised ML-TDFL using CNT-SAs. This cavity was utilised as a seed laser for the imaging laser system that has been used as a light source in biomedical imaging experiments at the Institute of Life Science (IfLS, University of Southampton).

Chapter 5 focuses on the development of an all-fiberised ML-TDFL with PM fibres/components. With an all-PM architecture, ML-TDFL demonstrates a self-start, turnkey ML operation with high tolerance to physical perturbations. Furthermore, to the best of my knowledge, this is the first demonstration of the nJ-energy-level dissipative-soliton, all-PM ML-TDFL enabled by CNT-SA. This work has been published *in Optics and Laser technology*. The technical findings in this chapter encompass the develop of other all-PM ML cavities that has high potential to be used in practical applications.

Chapter 6 discusses the development of a 1840-nm all-PM ML-TDFL laser system, which covers the development of a reliable erbium-doped fibre amplifier (EDFA) source, an all-PM ML-TDFL operating at 1840 nm, and an all-PM CPA system. This laser provides a reliable laser signal with a robust, turnkey ML operation. I developed this laser in our laboratory and delivered it to our external research partner at the University of Nottingham to be used as a light source for biomedical imaging experiments.

Chapter 7 presents a realisation of all-PM ML-TDFL using NALM. This all-fibre cavity has a potential to resolve technical difficulties associated with using material-base SAs (i.e., SESAM or CNTs). To the best of my knowledge, this is the first demonstration of the nJ-pulse-energy dissipative soliton using all-fibre, all-PM ML-TDFL with NALM-SA. This work has been published in *Optics Express*.

Chapter 8 concludes the summary of my thesis and discusses the possible future research directions.

Chapter 2 Theoretical background

In this chapter, I explain theory related to the experiments in this thesis. Section 2.1 briefly explains the optical fibre, including polarisation-maintaining (PM) and gain fibres. In section 2.2, the effect of pulse propagation inside optical fibres will be discussed. Section 2.3 focuses on relevant components to support the generation of passive mode-locking, along with the saturable absorbers. Section 2.4 explains the Lyot filter that can control operating wavelength and is required for dissipative-soliton operation. Different mode-locked operating regimes are explained in section 2.5. Finally, the last section explains the chirped pulse amplification technique, including pulse stretcher and compressor, as a technique to achieve high pulse energies with ultrashort pulse durations.

2.1 Optical fibres

Total internal reflection is the fundamental principle to facilitate wave-guiding in optical fibres [114]. Figure 2.1 presents an idealised schematic of an optical fibre structure, revealing two different areas named 'core' and 'cladding'. Typically, the fibre core is designed to have a higher refractive index than the surrounding cladding [114], which can be achieved by doping some index-raising materials, i.e., germania, alumina, or boron oxide, into the structure [115]. Consequently, total internal reflection can be realised inside the fibre core, guiding light along its length. Fibre cores can also be doped with laser-active dopants, i.e., ytterbium, erbium, and thulium, to feature as a gain fibre [116, 117]. Some relevant gain fibres will be explained later in this section.

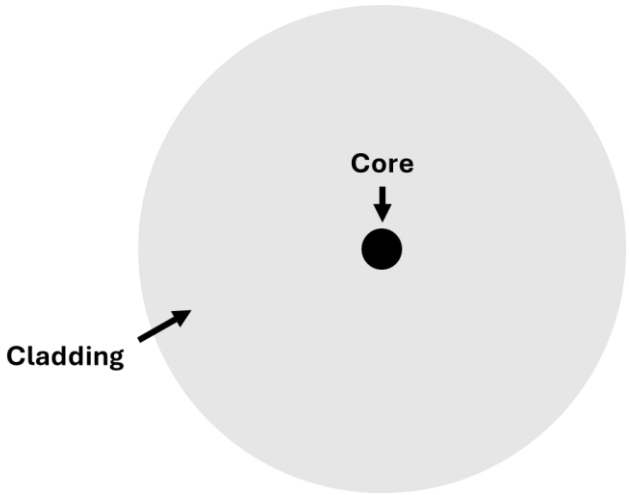

Figure 2.1 Idealised schematic of a 'step-index' optical fibre cross-section.

Single-mode fibre (SMF) refers to an optical fibre that supports wave guiding for fundamental mode only [114]. In SMF, the propagation constant remains unchanged for light with two

orthogonal polarisation states. In an ideal case, the properties of propagating light should be preserved while propagating in such optical fibres. Practically, that condition is hard to achieve. The propagating light typically encounters some losses, which might be caused by the nature of light scattering and manufacturing defects of the fibres [118]. Moreover, propagating light might encounter birefringence induced by physical perturbations, leading to variation of the polarisation [119]. Consequently, the variation could potentially lead to instabilities in some applications, i.e., mode-locked fibre lasers [21].

2.1.1 Polarisation-maintaining (PM) fibres

Polarisation-maintaining (PM) fibres are fabricated by intentionally introducing high birefringence into the fibre core [85]. In PM fibres, stress-induced areas are implemented in the cladding (across the core area) to apply an unequal tension along two orthogonal axes, named the 'fast axis' and the 'slow axis' (Figure 2.2) [120]. Polarisation of the propagating light can be preserved once aligned with one of these axes [84]. Due to the birefringence of PM fibre improving the tolerance to external perturbation, mode-locked cavities with all-PM fibres can be expected to have high robustness [86, 87]. In this thesis, the mode-locked cavities will be demonstrated in all-PM configurations.

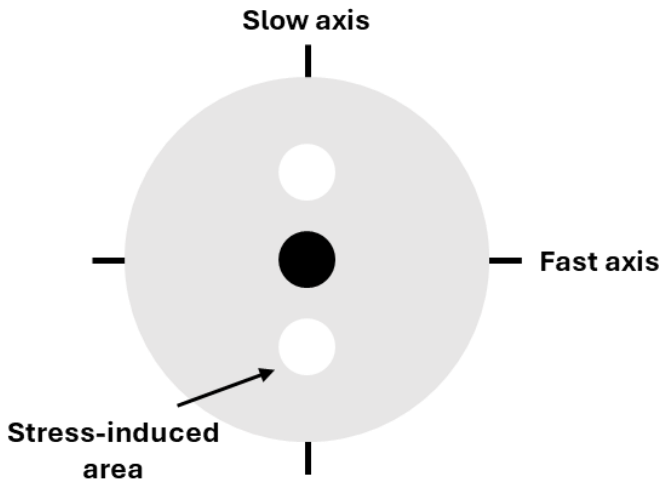

Figure 2.2 Idealised schematic of a polarisation maintaining (PM) fibre cross section.

2.1.2 Erbium-doped fibres

Erbium-doped fibres (EDFs) are one of the commonly used rare-earth doped fibres, especially in telecommunication applications. EDF provides optical gain at wavelengths in the ~1.5 μm region [121]. Typically, this gain fibre can be efficiently pumped by 0.9-1 μm, corresponding to an ion

transition from $^4I_{15/2}$ → $^4I_{11/2}$ (Figure 2.3) [122]. The excited ion can rapidly transition with a non-radiative emission from $^4I_{11/2}$ → $^4I_{13/2}$ and be captured in the latter state due to its longer relaxation time. Consequently, a population inversion can be achieved to support the transition of $^4I_{13/2}$ →$^4I_{15/2}$ relevant to emission at wavelengths around 1.5 µm [123]. EDFs require a high pump intensity to achieve an efficient emission in this quasi-three-level structure. However, the absorption-cross section of the EDF is relatively small [123]. Furthermore, the dopant concentration of erbium (Er^{3+})-ion needs to be limited (typically ~1000 ppm for standard-doped EDF) to avoid possible quenching processes, which leads to low output efficiency [124]. Practically, the absorption efficiency of EDF can be improved by co-doping with ytterbium (Yb^{3+})-ion that has larger absorption-cross section [123]. In the co-doped structure, pump signal can be efficiently absorbed by Yb^{3+}-ion and transfer to Er^{3+}-ion (Figure 2.3) [122], hence, enhance pump absorption coefficient.

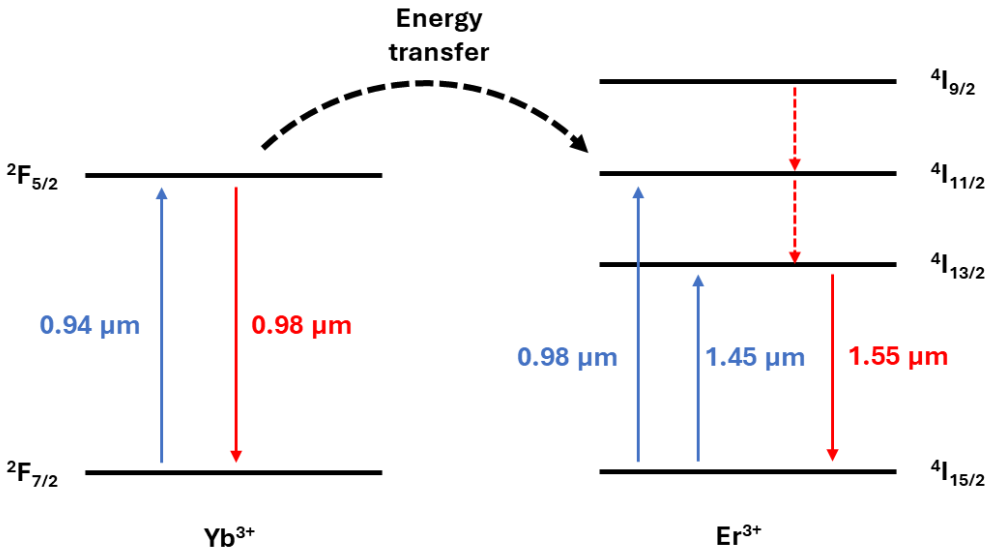

Figure 2.3 Energy level diagram of (left) ytterbium ions and (right) erbium ions. Red dash lines represent nonradiative emission.

In this thesis, erbium-ytterbium-doped fibres are detailed when used as gain fibres in amplifiers or lasers. These systems were pumped with continuous-wave (CW) laser at ~0.9 µm, generated by high-power laser diodes, to enable emission at ~1.5 µm. The emitted light is then used as a pump for thulium-doped fibre lasers.

2.1.3 Thulium-doped fibres

Thulium-doped fibres (TDFs) are promising gain materials to enable emission wavelengths near 2 µm [18, 125]. The energy diagram (Figure 2.4) illustrates that the ground-state electrons in thulium (Tm^{3+})-ions can be excited with three different pump schemes [125]. Tm^{3+}-ion can be excited by pump wavelength at ~0.8 µm, corresponding to the transition between $^3H_6$→$^3F_4$. The

excited ion can decay to the metastable state at $^3H_4$ by a non-radiative decay due to the short-life time of $^3F_4$ and the close spacing between $^3H_5$ and $^3H_4$ energy levels [126, 127]. In high-dopant concentration fibres (i.e., >2.0 wt%), this pump scheme can enable the 'cross-relaxation' process, where an activated thulium ion shares its energy with another ion in its ground state [128]. Consequently, these ions transition to an excited state at the $^3H_4$ level. This process is also called 'two-for-one' as two excited ions are created by absorbing one pump photon, leading to higher quantum efficiencies [129, 130]. However, this pump wavelength encounters a high thermal load due to the quantum defect between the absorption-emission photons [131]. A pump wavelength at ~1.2 µm, corresponding to the transition of $^3H_6 \rightarrow {}^3H_5$, tends to encounter excited state absorption that effectively increase laser threshold [132]. The TDF can be efficiently pumped using an in-band pump scheme with wavelengths of ~1.5-1.8 µm, corresponding to ion transition $^3H_6 \rightarrow {}^3H_4$. This pumping scheme has a minimal quantum defect, resolving thermal effect, and provides high Stoke efficiency to be ~0.75-0.85 [133]. TDF systems have been demonstrated to have high output efficiencies using this pump wavelength [134]. Furthermore, high-brightness beams at this pump wavelength can be efficiently supported by erbium-ytterbium-doped fibre amplifiers (EDFAs) [135]. This pump scheme will be used in experiments.

As depicted in Figure 2.5, TDF has an extended emission bandwidth, ranging from 1.6-2.2 µm, corresponding to the transition $^3H_4 \rightarrow {}^3H_6$ [18, 125]. It is worth noting that the broad emission is caused by the increased number of Stark components in the energy level of the Tm^{3+}-ions [126]. The absorption cross section is presented in Figure 2.6.

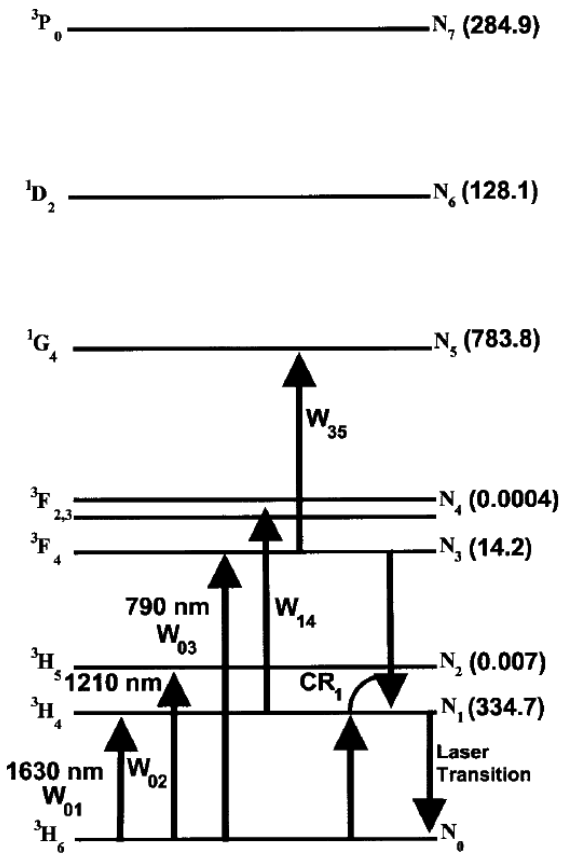

Figure 2.4 Energy level diagram of thulium ions. The number related to the lifetime (in μs) of each energy level is presented in the parenthesis. This figure has been reproduced from [125], Institute of Electrical and Electronics Engineers (IEEE) does not require permission for reuse in thesis. ***© 1999 IEEE****.*

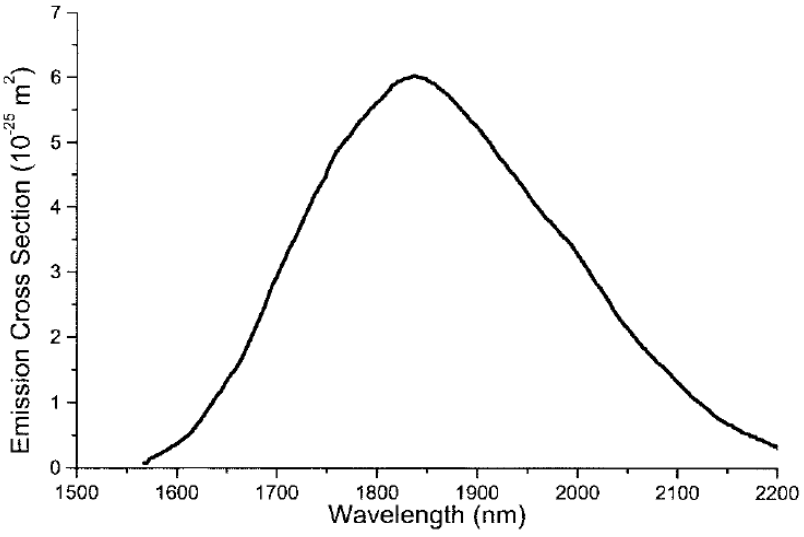

Figure 2.5 Emission spectrum of thulium-ion transition from $^3H_4 \rightarrow {}^3H_6$. This figure has been reproduced from [125], Institute of Electrical and Electronics Engineers (IEEE) does not require permission for reuse in thesis. ***© 1999 IEEE****.*

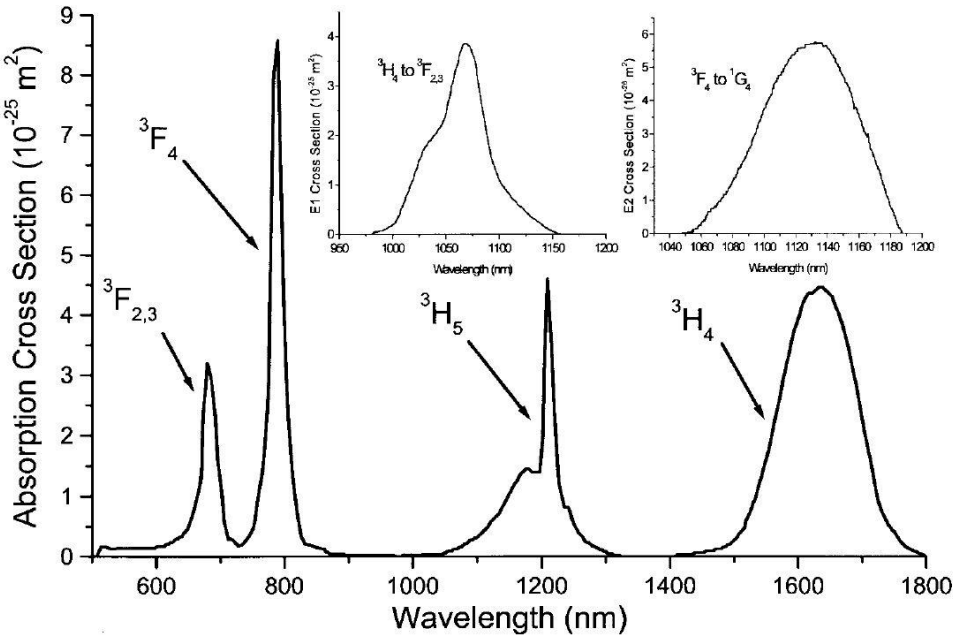

Figure 2.6 Ground state absorption cross-section spectrum, and (inset) excited state absorption of thulium ions. This figure has been reproduced from [125], Institute of Electrical and Electronics Engineers (IEEE) does not require permission for reuse in thesis. ***© 1999 IEEE****.*

2.2 Pulse propagation in optical fibres

In this section, I explain the relevant theory of pulse propagation in optical fibres, which is an important behaviour in generating fiberised mode-locked cavities.

2.2.1 Nonlinear Schrödinger equation

Pulse propagation in optical fibres can be explained using the nonlinear Schrödinger equation (NLSE), which is expressed as [136]:

$$\frac{\partial A}{\partial z}+\frac{\alpha}{2}A+\frac{i\beta_2}{2}\frac{\partial^2 A}{\partial T^2}-\frac{i\beta_3}{6}\frac{\partial^3 A}{\partial T^3}=i\gamma\left(|A|^2A+\frac{i}{\omega_0}\frac{\partial}{\partial T}(|A|^2A)-T_RA\frac{\partial}{\partial T}|A|^2\right) \qquad (2.1)$$

where A denotes the pulse envelope that varies in response to propagation distance z at time t. α represents the linear loss in optical fibre. β_2 and $\beta_3$represent the second-order and third-order group velocity dispersion (GVD), respectively. $T=t-z/v_g$ is the temporal parameter in the moving reference frame. γ is the nonlinear parameter of optical fibre. ω_0 is the central frequency. T_R represents Raman response function.

Generally, the NLSE can be simplified when considering a wide temporal pulse, i.e., $T_0>5\ ps$. In this case, the parameters $(\omega_0T_0)^{-1}$ and T_R/T_0 become very small (<0.001). Therefore, the last two terms in equation (2.1) are neglected. Furthermore, the third-order dispersion term can also be

disregarded when considering the wavelength away from the zero-dispersion wavelength. The simplified NLSE can be written as [136]:

$$i\frac{\partial A}{\partial z} + i\frac{\alpha}{2}A - \frac{\beta_2}{2}\frac{\partial^2 A}{\partial T^2} + \gamma|A|^2 A = 0, \tag{2.2}$$

From equation (2.2), pulse propagation in optical fibres can be explained by the simplified NLSE, which incorporates effects of the fibre loss ($i\frac{\alpha}{2}A$), its GVD $\left(\frac{\beta_2}{2}\frac{\partial^2 A}{\partial T^2}\right)$, and nonlinearity ($\gamma|A|^2A$). The nonlinear parameter (γ) can be calculated by [136]:

$$\gamma = \frac{\omega n_2}{cA_{eff}}, \tag{2.3}$$

where ω denotes the electric field frequency, n_2 represents the nonlinear refractive index, c is the speed of light in vacuum, and the effective mode-area $\left(A_{eff}\right)$ is defined as [136]:

$$A_{eff} = \frac{\left(\int\int_{-\infty}^{\infty}|F(x,y)|^2 dxdy\right)^2}{\int\int_{-\infty}^{\infty}|F(x,y)|^4 dxdy}. \tag{2.4}$$

where $F(x,y)$ represents the modal distribution function of the fundamental fibre mode. The general solution of equation (2.2) can be written as [136]:

$$A(z,\tau) = \sqrt{P_0}e^{\left(-\frac{\alpha z}{2}\right)}U(z,\tau), \tag{2.5}$$

where P_0 is the initial peak power. $U(z,\tau)$ is the normalized amplitude function. $\tau = \frac{T}{T_0} = \frac{t-z/v_g}{T_0}$ is the normalized time scale to the input pulse width T_0. Hence, $U(z,\tau)$ satisfies:

$$i\frac{\partial U}{\partial z} = \frac{\mathrm{sgn}(\beta_2)}{2L_D}\frac{\partial^2 U}{\partial \tau^2} - \frac{\exp(-\alpha z)}{L_{NL}}|U|^2 U, \tag{2.6}$$

where $\mathrm{sgn}(\beta_2) = \pm 1$ corresponds to the GVD sign. This equation reveals that the propagating pulses experience effects that influence by both dispersion and nonlinearity. Therefore, it is useful to define two relative length scales, relevant to each effect as [137]:

$$L_D = \frac{T_0^2}{|\beta_2|}, \tag{2.7}$$

$$L_{NL} = \frac{1}{\gamma P_0}. \tag{2.8}$$

where L_D and L_{NL} represent the dispersion length and the nonlinear length, respectively. The relative influence of each effect can be estimated by comparing these length scales. For any propagation length (L), neither dispersion nor nonlinearity have a significant effect when $L \ll L_D$ and $L \ll L_{NL}$. The dispersion effect is dominant when $L \sim L_D \ll L_{NL}$. In contrast for $L \sim L_{NL} \ll L_D$, the nonlinearity effect becomes powerful. An interplay between these effects leads to 'modulation instability', which will be explained later in this section.

2.2.2 Group velocity dispersion

To evaluate the effect of the GVD, assuming that the pulse propagates in a lossless fibre that has $L \sim L_D \ll L_{NL}$. Hence, the pulse propagation is dominated by the GVD without the nonlinearity. The nonlinear parameter γ can be set to zero. Therefore, the NLSE can be expressed as [137]:

$$i\frac{\partial A}{\partial z} = \frac{\beta_2}{2}\frac{\partial^2 A}{\partial T^2} \tag{2.9}$$

Defining $U(z,T)$ as the normalized amplitude, hence, it satisfies [137]:

$$i\frac{\partial U}{\partial z} = \frac{\beta_2}{2}\frac{\partial^2 U}{\partial T^2} \tag{2.10}$$

This equation can be solved via the Fourier transform (in the frequency domain) and gives the solution of [137]:

$$\widetilde{U}(z,\omega) = \widetilde{U}(0,\omega)\exp\left(\frac{i}{2}\beta_2\omega^2 z\right). \tag{2.11}$$

The solution indicates that the GVD effect does not generate new frequencies, however, it changes the phase of each frequency component in the original pulse. For the incident Gaussian pulse with the full width at half-maximum (FWHM) of T_0 ($T_{FWHM} = 1.665T_0$), the normalized amplitude function of incident pulse can is given by [137]:

$$U(0,T) = \exp\left(-\frac{T^2}{2T_0^2}\right) \tag{2.12}$$

Therefore, the normalized amplitude function at propagation distance (z) can be calculated by [137]:

$$U(z,T) = \frac{T_0}{\sqrt{T_0^2 - i\beta_2 z}}\exp\left(-\frac{T^2}{2(T_0^2 - i\beta_2 z)}\right) \tag{2.13}$$

while the phase variation can be expressed as [137]:

$$\phi(z,T) = -\frac{\mathrm{sgn}(\beta_2)\frac{z}{L_D}}{1+\left(\frac{z}{L_D}\right)^2}\frac{T^2}{2T_0^2} + \frac{1}{2}\tan^{-1}\left(\mathrm{sgn}(\beta_2)\frac{z}{L_D}\right) \tag{2.14}$$

Hence, the frequency chirp ($\delta\omega$) can be defined as [137]:

$$\delta\omega(T) = -\frac{\partial\phi}{\partial T} = \frac{\mathrm{sgn}(\beta_2)\frac{z}{L_D}}{1+\left(\frac{z}{L_D}\right)^2}\frac{T}{T_0^2}. \tag{2.15}$$

The chirp implies that the frequency changes linearly across the pulse with behaviour corresponding to the sign of β_2. The frequency chirp of some fibres used in experiments are plotted in Figure 2.7, assuming a pulse width of 1 ps, at a wavelength of 1.9 μm. As depicted, these

fibres have different chirps regarding to the β_2 values. In negative β_2 fibres (TDF and SMF), the frequency chirp is positive at the leading edge of the pulse and becomes negative at the tailing edge, and vice versa in the positive β_2 fibres (DCF). This mechanism can be used to compensate the frequency chirp in the cavity or control the pulse-broadening behaviour.

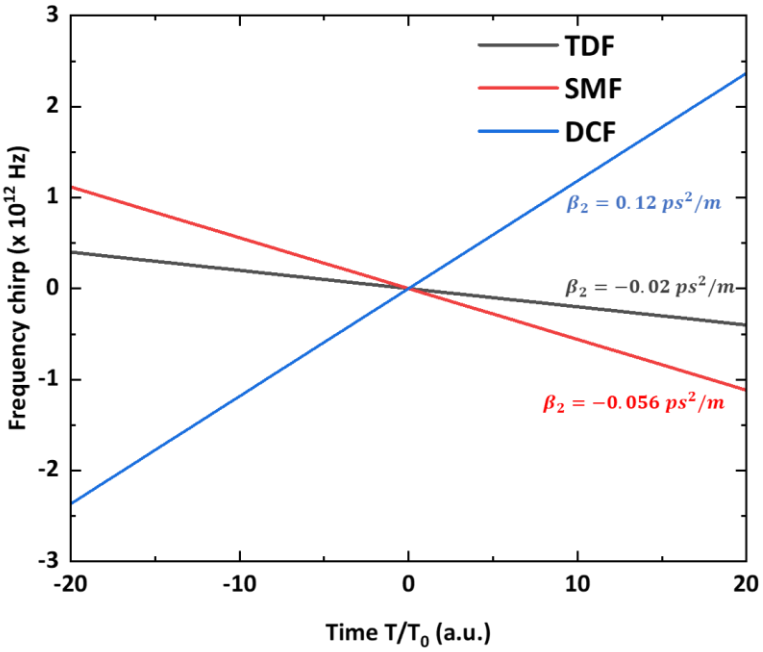

Figure 2.7 Frequency chirp induced by dispersion for different fibres in experiments, estimated by equation (2.15).

2.2.3 Self-phase modulation

Self-phase modulation (SPM) is a nonlinear effect that leads to spectral broadening. For optical fibres with $L \sim L_{NL} \ll L_D$, the nonlinear effect dominates in the pulse propagation without the GVD effect, and equation (2.2) becomes [138]:

$$\frac{\partial U}{\partial z} = i\frac{e^{-\alpha z}}{L_{NL}}|U|^2 U \tag{2.16}$$

The solution of this equation can be written as [138]:

$$U(L,T) = U(0,T)\exp\left(i\phi_{NL}(L,T)\right) \tag{2.17}$$

where the nonlinear phase shift is defined as [138]:

$$\phi_{NL} = |U(0,T)|^2\left(\frac{L_{eff}}{L_{NL}}\right) \tag{2.18}$$

$$L_{eff} = \frac{1 - e^{-\alpha L}}{\alpha} \tag{2.19}$$

L_{eff} represents the effective length, which is shorter than the actual fibre length L due to the fibre loss. Equation (2.18) reveals that the phase shift caused by SPM depends on the intensity and increases with propagation distance in fibres. The SPM-induced frequency chirp ($\delta\omega$) can be calculated by [138]:

$$\delta\omega = -\frac{\partial \phi_{NL}}{\partial T} = -\left(\frac{L_{eff}}{L_{NL}}\right)\frac{\partial}{\partial T}|U(0,T)|^2. \tag{2.20}$$

It results in the generation of new frequency components to the initial pulse, i.e., broadening the spectrum. The SPM effect strongly depends on the initial pulse shape. For a Gaussian pulse, the frequency chirp can be calculated by [138]:

$$\delta\omega = \frac{2T}{T_0^2}\frac{L_{eff}}{L_{NL}}\exp\left[-\left(\frac{T}{T_0}\right)^2\right] \tag{2.21}$$

Figure 2.8 presents the calculated frequency chirp induced by SPM from different fibres used in experiments, under the assumption of an initial peak power of 1 W, pulse duration of 1 ps, at wavelength of 1.9 μm, and nonlinear refractive index of $n_2 \approx 3.55 \times 10^{-20}$ [139]. As depicted, the chirp is negative near the leading edge. This chirp is linearly increasing across the centre of the pulse and becomes positive near the trailing edge.

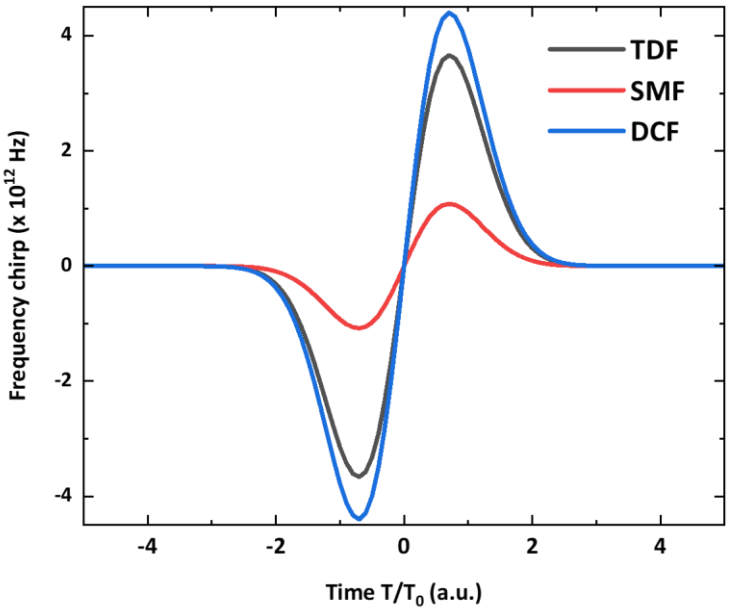

Figure 2.8 Frequency chirp induced by nonlinearity for different fibres in experiments, calculated by equation (2.21).

2.2.4 Modulation instability

An interplay between GVD and SPM can cause modulation instability, leading to the breaking up of a CW signal or quasi-CW signal into a train of ultrashort pulses. Consider the NLSE in a loss-less fibre [140]:

$$i\frac{\partial A}{\partial z} = \frac{\beta_2}{2}\frac{\partial^2 A}{\partial T^2} - \gamma|A|^2 A \tag{2.22}$$

For the case of CW signal propagation without loss, A can be assumed to be time-independent. Therefore, the solution of this equation can be given by [140]:

$$A = \sqrt{P_0}\exp(i\phi_{NL}) \tag{2.23}$$

where P_0 is the initial power and ϕ_{NL} is the nonlinear phase shift due to the SPM. The stability of this solution can be analysed by introducing a small perturbation term $a(z,T)$. The perturbed solution becomes [140]:

$$A = \left(\sqrt{P_0} + a\right)\exp(i\phi_{NL}) \tag{2.24}$$

Hence, equation (2.22) can be linearised in 'a' as [140]:

$$i\frac{\partial a}{\partial z} = \frac{\beta_2}{2}\frac{\partial^2 a}{\partial T^2} - \gamma P_0(a + a^*). \tag{2.25}$$

The solution of $a(z,T)$ can be written in a form of [140]:

$$a(z,T) = a_1 \exp[i(Kz - \Omega T)] + a_2 \exp[-i(Kz - \Omega T)] \tag{2.26}$$

where K and Ω are the wave number and frequency of the perturbation, respectively. a_1 and a_2 represent the amplitudes of the perturbations. The nontrivial solutions of this equation can be found when K and Ω satisfied the relation [140]:

$$K = \pm\frac{1}{2}|\beta_2\Omega|\sqrt{\Omega^2 + \mathrm{sgn}(\beta_2)\Omega_c^2} \tag{2.27}$$

where $\mathrm{sgn}(\beta_2) = \pm 1$ is the sign of β_2, and

$$\Omega_c^2 = \frac{4}{\beta_2 L_{NL}} \tag{2.28}$$

The stability of this solution is determined by the term $\mathrm{sgn}(\beta_2)$. K is real for all Ω with normal GVD ($\beta_2 > 0$), manifesting a stable steady state over the perturbation. However, modulation instability occurs in the anomalous GVD regime ($\beta_2 < 0$) with $|\Omega| < \Omega_c$, where K becomes imaginary. The perturbation is exponentially increasing with z, leading to the generation of sidebands at wavenumber $\beta_0 \pm K$, and frequency $\omega_0 \pm \Omega$, accordingly, breaking the CW or quasi-CW signal into a train of ultrashort pulses, which can lead to mode-locked operation.

2.3 Mode-locked fibre lasers

In this section, I explain mode-locked fibre lasers. Additionally, this section introduces saturable absorbers (SAs), which are crucial components for mode-locked operation in lasers. The section also includes a description of the Lyot filter, which is a filtering effect that is required for generating the dissipative soliton. Different regimes of the mode-locked operation are explained in the final part of this section.

2.3.1 Passively mode-locked fibre lasers

Mode-locking is a technique to generate ultrafast pulses with a duration in the hundreds of fs-level. Mode-locked (ML) operation can be manifested by fixing the phase relationship between longitudinal modes within the laser cavity [141]. Typically, there are two approaches to achieve ML operation. Actively ML method refers to the technique in which a phase-lock mechanism is introduced by external sinusoidal modulation signals (Figure 2.9) [58, 142]. In contrast, the passively ML method uses SAs with nonlinear absorption mechanisms, to obtain the phase-

locked mechanism (Figure 2.10) [143], in which the absorption is significantly reduced for high-intensity signals.

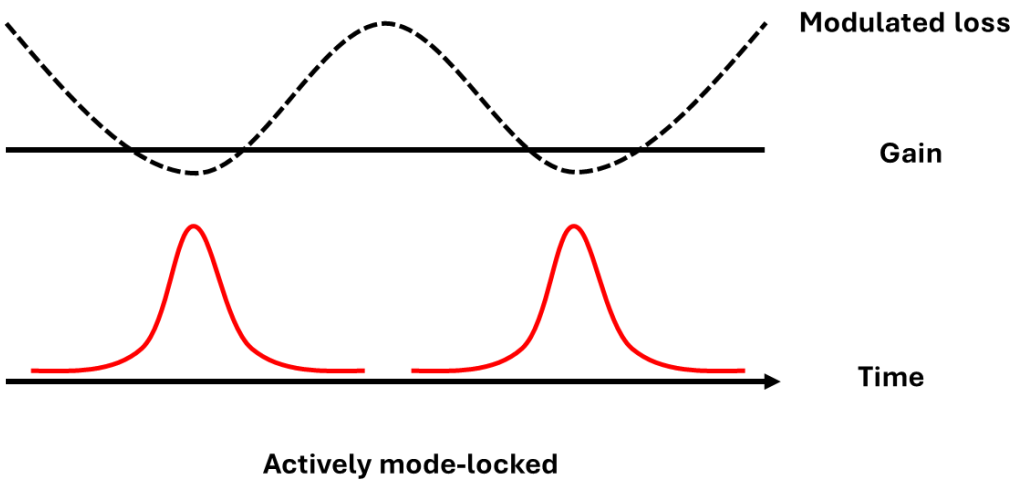

Figure 2.9 Idealised schematic for actively mode-locked operation.

An interplay between GVD and SPM in optical fibres leads to modulation instability, breaking the CW signals into a pulse train [144]. When a pulse oscillates in the cavity and interacts with the SA, only high-intensity modes can be efficiently amplified. Consequently, ML operation can be formed and generates stable ultrashort pulses. Generally, the loss modulation exhibited by SA is much faster than a modulated signal in active mode-locking, hence, generating much shorter pulses [75]. In experiments, passive mode-locking is the primary method used to generate ultrashort pulses.

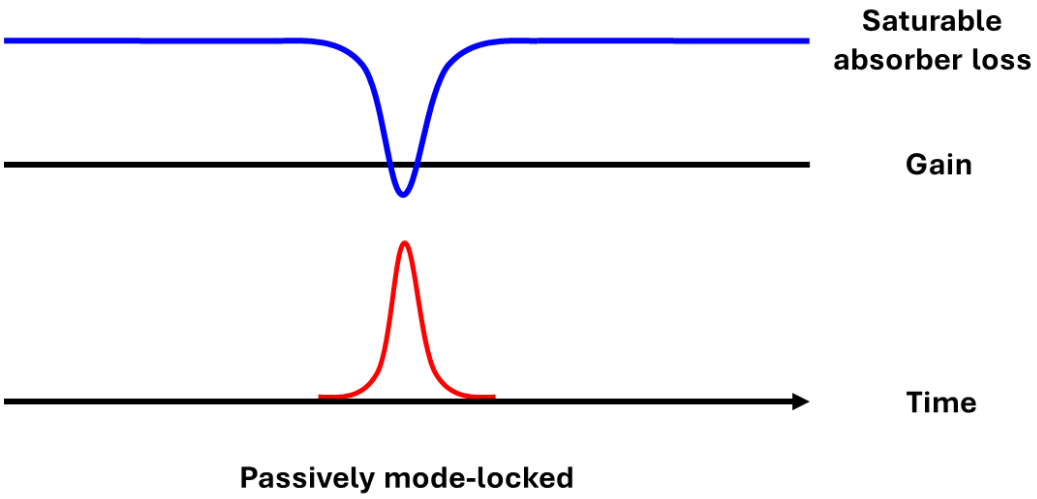

Figure 2.10 Idealised schematic for passively mode-locked operation.

2.3.2 Saturable absorbers

Saturable absorption is an important mechanism to initiate pulsed-mode operation in passively mode-locked lasers. SAs refer to optical components in which absorption is significantly reduced at higher signal intensities [76]. Generally, SAs can be categorised into two groups [77]. In material-based SA, availability of energy states in the conduction band decreases when the material is exposed to intense electric fields, leading to the saturable absorption mechanism [76]. Fibre-based SA provides the saturable absorption mechanism through properties of oscillating pulses in fibres, i.e., Kerr-nonlinearity [81].

In material-based SA, the intensity-dependent absorption of a fast saturable absorber can be demonstrated by [145]:

$$s = \frac{s_0}{1 + I/I_{sat}} \tag{2.29}$$

where I represents the intensity, and I_{sat} denotes the saturation intensity. Figure 2.11 presents the variation of intensity-dependent absorption based on equation (2.29).

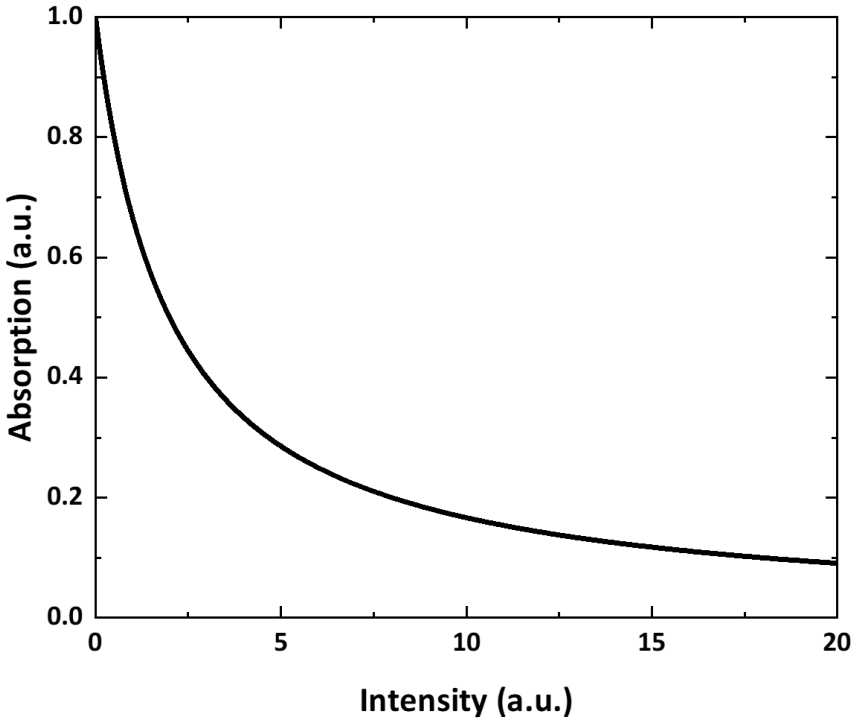

Figure 2.11 Intensity dependent absorption of saturable absorbers, correspond to equation (2.29).

Several SAs will be discussed in this section. These SAs were used in experiments to support the generation of ultrafast passively mode-locked pulses.

2.3.2.1 Semiconductor saturable absorber mirror

Semiconductor saturable absorber mirror (SESAM) is one of the material-based SAs that will be used in experiments. Figure 2.12 presents an idealised structure of a SESAM. A highly reflective distributed Bragg reflector (DBR) structure (GaAs/AlAs in this case) is grown on a GaAs substrate. The thickness of each layer can be controlled to be equal to a quarter wave, corresponding to the desired central wavelength. On the top layer of the DBR, a bulk-layer layer of semiconductor or a multiple Quantum well (MQW) structure is implemented to provide a saturable absorption [79, 146]. Therefore, an intensity-dependent reflectance for the SESAM can be achieved. SESAMs have been widely demonstrated to support mode-locked operation in several wavelength ranges [147-150].

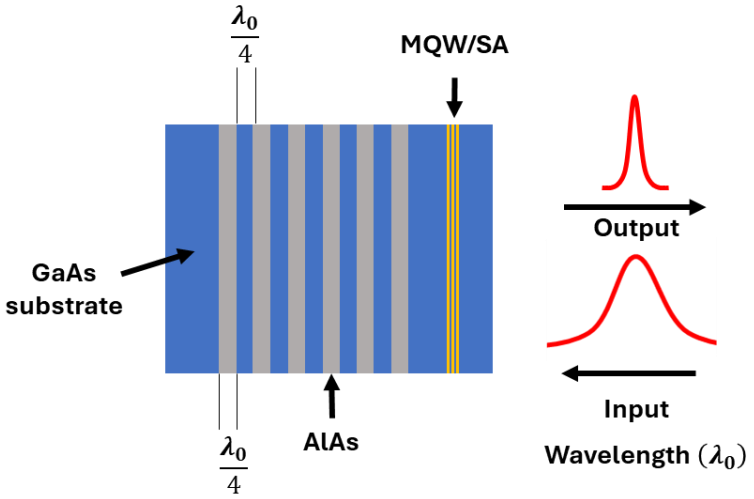

Figure 2.12 Schematic of the semiconductor saturable absorber mirror (SESAM) structure.

The intensity-dependent reflection of a SESAM with long relaxation time can be estimated by [151]:

$$R(F) = 1 - \frac{A_0 F_{sat}}{F}\left(1 - \exp\left(-\frac{F}{F_{sat}}\right)\right) - A_{ns}\,, \tag{2.30}$$

where $R(F)$ represents the intensity-dependent reflection as a function of the pulse fluence F, A_0 is the absorbance, F_{sat} is the saturation fluence, and A_{ns} is the non-saturated loss. Figure 2.13 presents the reflectivity of the SESAM (SAM-1920-36-10ps, Batop), which was used in the experiments detailed in Chapter 3, incorporated with the information provided by the supplier [151, 152]. It reveals an intensity-dependent reflection that is required to support passively mode-locked operation. However, this SESAM has limited operating wavelength as presented in Figure 2.14, which reveals a high reflection band from 1850-2000 nm [152].

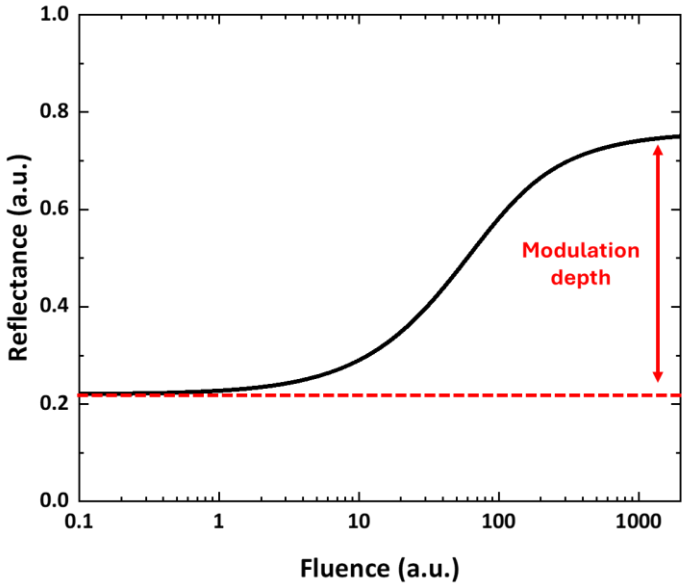

Figure 2.13 Intensity dependent reflectance of SAM-1920-36-10ps, Batop with equation (2.30) with the information provided on supplier website [152].

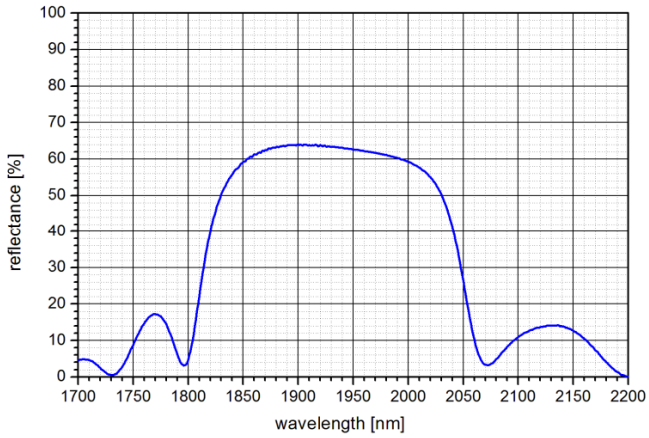

Figure 2.14 Reflectance of SAM-1920-36-10ps, Batop. This figure has been reproduced from information sheet, provided on supplier website [152].

2.3.2.2 Carbon nanotubes saturable absorber

Carbon nanotube (CNT) is another material-based SA that will be explored in experiments. CNTs have been widely demonstrated in ML lasers [54, 78, 153, 154], as they support a broad range of operating wavelengths that can be varied by controlling their physical properties, i.e., molecular structure or sample thickness [78]. Moreover, the saturable absorption mechanism of the CNT-based SA can be designed [32, 63]. Figure 2.15 (top) presents an example of wavelength-dependent transmission of CNTs used in the experiments detailed in Chapter 4. The nonlinear transmission of CNTs can be characterised using a fast SA model expressed by [32, 155]:

$$T(F) = 1 - \frac{\Delta T}{\sqrt{\frac{F}{F_{sat}} + \left(\frac{F}{F_{sat}}\right)^2}} \operatorname{atanh}\left(\sqrt{\frac{F}{F_{sat} + F}}\right) + (1 - A_{ns}) \tag{2.31}$$

where ΔT is the modulation depth, A_{ns} is the non-saturable losses, and F_{sat} is the saturation fluence. Figure 2.15 (bottom) presents the nonlinear transmission of CNTs, along with a fitted curve using equation (2.31). The details of CNTs characterisations will be explained in Chapter 4.

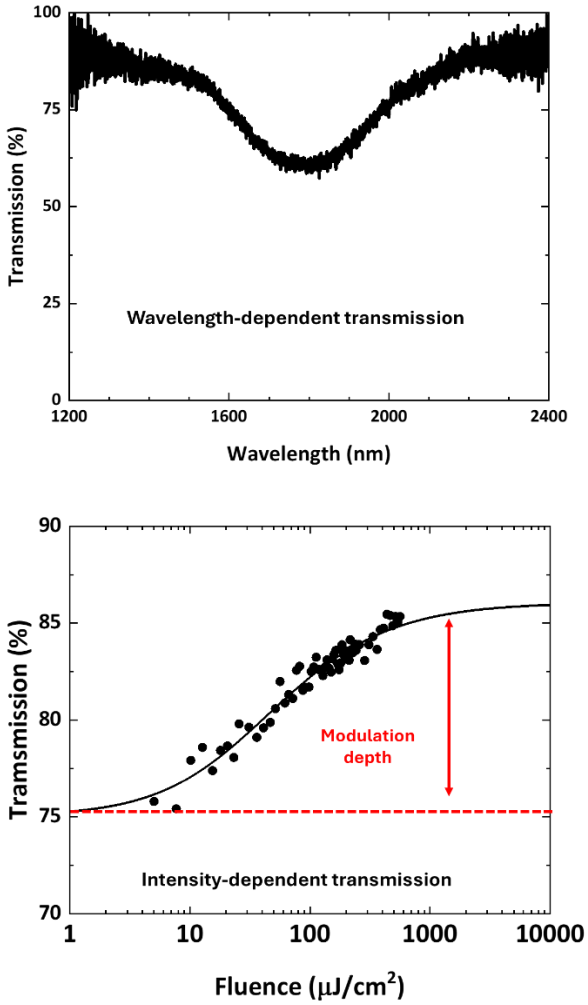

Figure 2.15 (top) Wavelength-dependent transmission of the carbon nanotubes, (bottom) intensity-dependent transmission of the carbon nanotubes, solid curve is the theoretical fit with equation (2.31) ($\Delta T = 11\ \%, F_{sat} = 28.6\ \mu J/cm^2, A_{ns} = 61.79\ \%$).

2.3.2.3 Nonlinear polarisation rotation

Nonlinear polarisation rotation (NPR) is one of the fibre-based SA techniques that has been used in mode-locked fibre lasers [156]. Figure 2.16 presents a schematic of the Kerr shutter setup, utilising the NPR. At the input, linearly polarised light transitions into elliptically polarised after being transmitted through a quarter-waveplate. The light is separated into two orthogonal components, denoting A_x and A_y. As these linearly polarisation modes propagate through the

optical fibre, they experience different nonlinear phase shifts due to the effects of intensity-dependent self-phase modulation and cross-phase modulation. These signals are combined at the output of the setup. By adjusting a half-waveplate and output polariser, only a small portion of the pulses have minimal loss and can be transmitted [157]. Therefore, this method can be used as an SA in a fiberised mode-locked cavity [23].

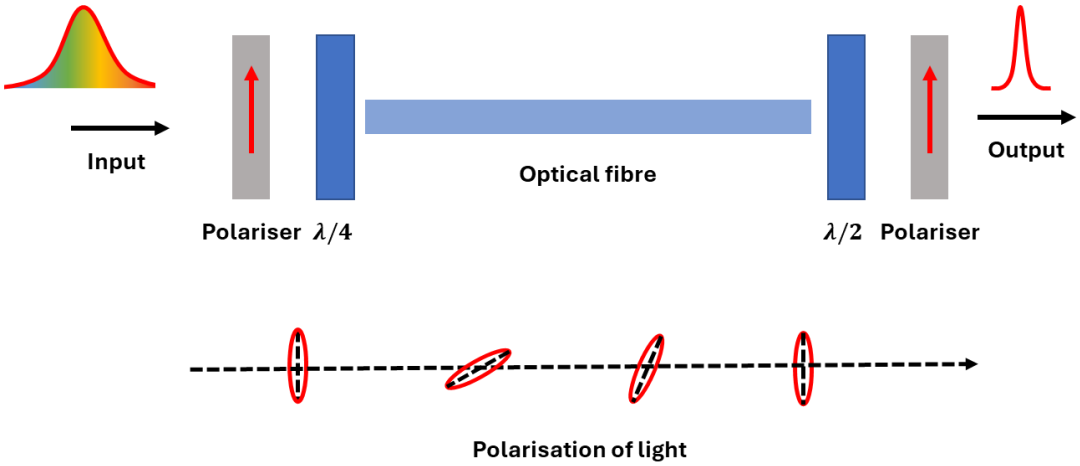

Figure 2.16 Schematic of the Kerr shutter, utilising the nonlinear polarisation rotation (NPR) technique.

2.3.2.4 Nonlinear amplifying loop mirror

Nonlinear amplifying loop mirror (NALM) is a fibre-base SA that has been demonstrated over several wavelength ranges [37, 82, 158-160]. Figure 2.17 presents a simplified schematic of a NALM-SA, consisting of a coupler, an amplifier, and an optical fibre loop. In the NALM loop, the input pulse splits into two counter-propagating directions, corresponding to the coupling ratio. Oscillating light in one direction experiences optical gain through the amplifier then propagates through the fibre loop. Meanwhile in the other direction, light propagates through the fibre loop with lower power, then is amplified. Consequently, these counter-propagating signals experience different nonlinear phase shifts. When they interfere at the coupler, the transmission (output) of the NALM loop varies with the phase difference. The NALM transmission (T) can be written as [161]:

$$T = 1 - 2r(1-r)\{1 + \cos[(1-r-gr)\gamma P_0 L]\} \tag{2.32}$$

where r is the coupling ratio, g is the gain factor, γ is the nonlinear coefficient, P_0 is the input power, and L is the NALM-SA fibre length. Figure 2.18 presents the calculated power-dependent transmittances of NALMs with different coupling ratios, revealing the saturable absorption and the modulation depth behaviour of the NALM-SA.

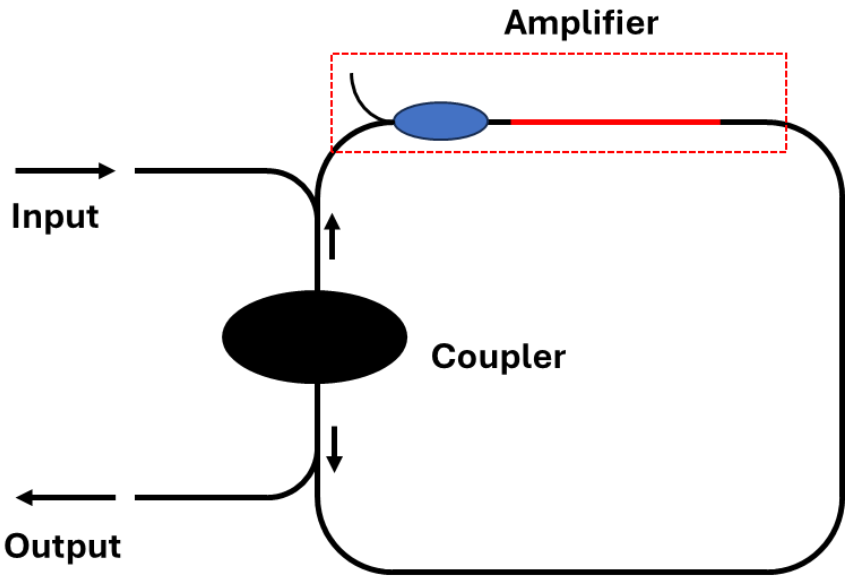

Figure 2.17 Idealised schematic for the nonlinear amplifying loop mirror (NALM).

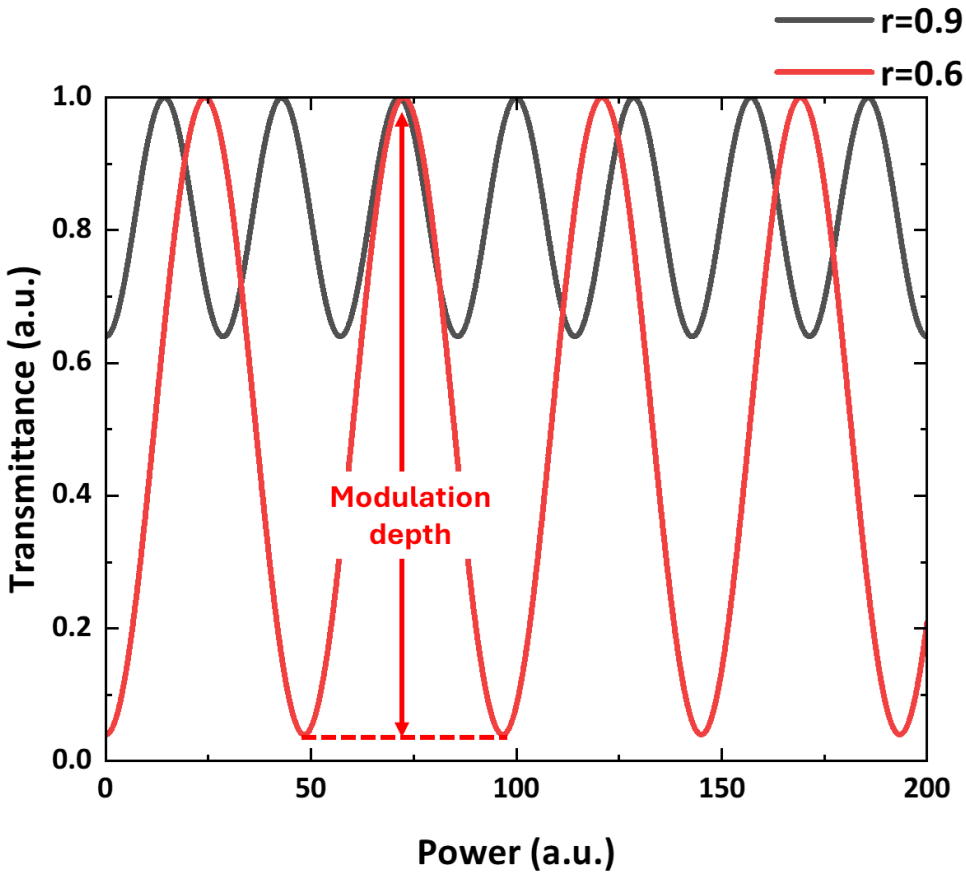

Figure 2.18 Simulated nonlinear transmission of the nonlinear amplifying loop mirror (NALM) with different coupling ratio, calculated by equation (2.32).

2.4 Lyot filter

Lyot filters (LFs) introduce a periodic bandpass filtering effect using a birefringent material [162]. Figure 2.19 shows the simplest configuration of the free-space LF. A birefringent crystal is employed between two polarisers, with a 45-degree offset between its optical (principal) axis and the polariser direction. When the linearly polarised light is incident on the crystal, it couples into polarisation basis states defined by the axes of the birefringent crystal. The transmitted light experiences different phase delays for the respective polarisation states, which are wavelength dependent. In combination with the output polariser, a bandpass filter effect can be created. [163].

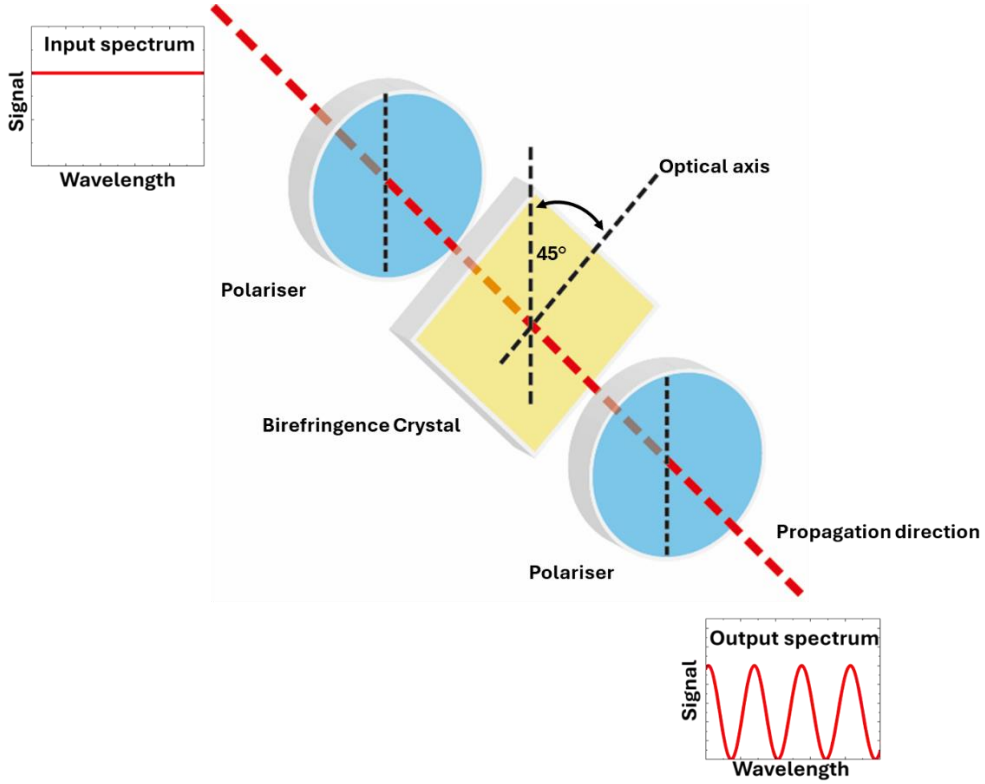

Figure 2.19 Idealised schematic of Lyot filters with birefringence crystal and polarisers.

In the context of a fiberised system, a LF can be demonstrated with high-birefringence fibres, i.e., PM fibres. Fiberised LFs can be created in several configurations [164]. Figure 2.20 presents a schematic of the fiberised LF used in experiments, facilitated by an offset-spliced method of PM fibres in the connection between a PM output coupler (PM-OC) and a PM isolator (PM-ISO). A fast-axis-blocked PM-OC is employed to ensure the linearly polarised light aligns with the slow axis. A PM-SMF, with high birefringence, is spliced to the PM-OC output pigtail with a 45-degree offset angle between their optical axes. Consequently, the linearly polarised light is coupled into both polarised states of the PM-SMF. These propagating modes experience different phase delays that are wavelength dependent. To compensate effects of possible polarisation-dependent dispersion

and prevent temporal walk-off of oscillating pulses, a section of PM-SMF with an identical length to the PM-isolator (PM-ISO) input tail is spliced with a 45-degree offset splice to the LF and a 90-degree offset splice to the PM-ISO input tail [165, 166]. Subsequently, a filtering effect is observed at the output of the fast-axis-blocked PM-ISO.

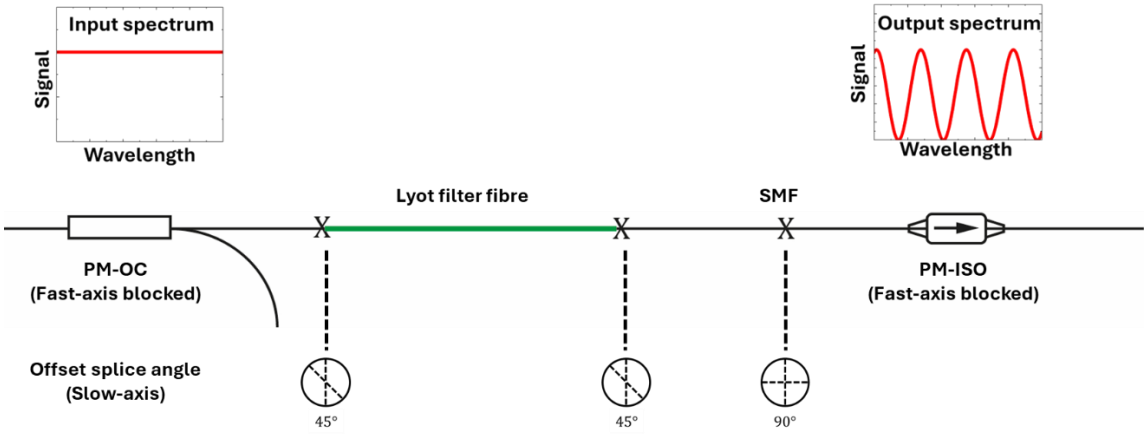

Figure 2.20 Idealised schematic of the fiberised Lyot filter using polarisation maintaining (PM) fibres. PM-OC: PM-output coupler; PM-ISO: PM-Isolator; SMF: PM single-mode fibre.

The transmission of the fiberised LF (T) can be calculated by [167, 168]:

$$T = 1 - \sin^2(2\theta)\sin^2\left(\frac{\pi L \Delta n}{\lambda}\right) \tag{2.33}$$

where θ represents an offset angle at the input of LF, L denotes the LF fibre length, Δn is the fibre birefringence, and λ is the wavelength. Figure 2.21 (grey curve) presents wavelength-dependent transmission of the LF. This behaviour can be varied by adjusting the parameters in equation (2.33). The maximum depth of LF can be varied by adjusting θ as presented in Figure 2.21. The filter period can be changed by adjusting fibre length L at a fixed birefringence Δn, or vice versa (Figure 2.22).

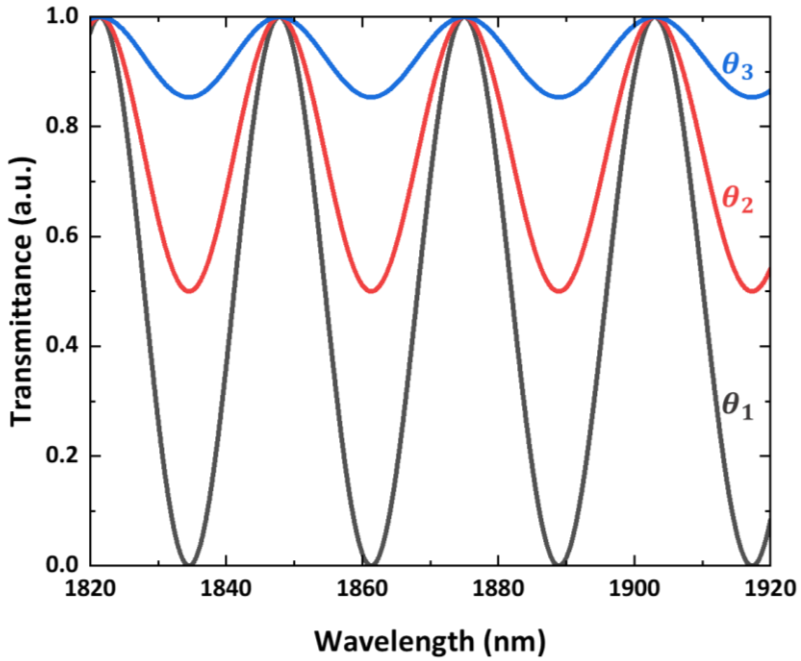

Figure 2.21 Lyot filter transmission behaviour with different input offset-angle, estimated by equation (2.33) with $\theta_1 = \pi/4, \theta_2 = \pi/8,$ *and* $\theta_3 = \pi/16$.

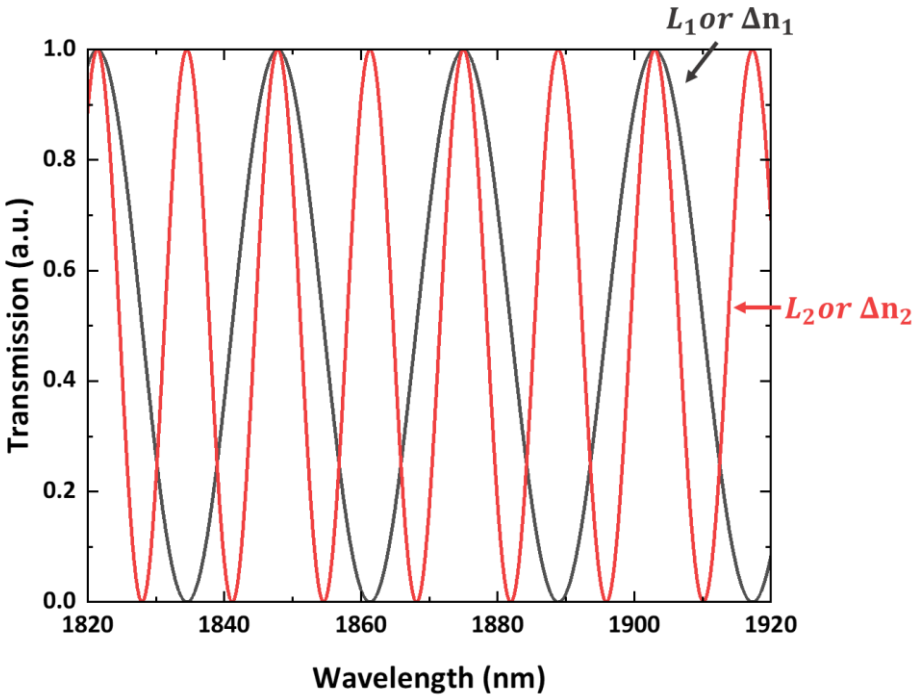

Figure 2.22 Lyot filter transmission behaviour with different fibre length at a fixed birefringence (and vice versa), estimated by equation (2.33).

The free-spectral range (FSR) of the LF can be estimated by [166]:

$$\Delta\lambda = \frac{\lambda^2}{L\Delta n} \tag{2.34}$$

The spectral bandwidth can be controlled by changing the LF fibre length. This experiment will be explained later in chapter 5.

2.5 Operating regimes of mode-locked lasers

2.5.1 Conventional-soliton mode-locked lasers

The conventional-soliton fibre lasers were first demonstrated in 1984 using anomalous dispersion fibres [169]. In conventional-soliton regime, the ML operation is generated based on the balanced conservative effects between SPM and (anomalous) GVD, resulting in stable pulse properties. For ML operation in the 2-μm region where the typical SMFs provide anomalous dispersion, conventional solitons are common ML pulse formation mechanisms that can be sustained in cavities. Figure 2.23 presents an idealised schematic of oscillating pulse properties in conventional soliton, revealing constant temporal and spectral properties. The amplitude varies in response to optical gain/loss in the cavity. The general solution of this soliton can be expressed in sech^2-pulse shape as [170]:

$$P(T) = P_{peak}\,\mathrm{sech}^2\left(\frac{T}{T_0}\right) \tag{2.35}$$

where $P(T)$ denotes the pulse profile at each temporal position T, P_{peak} represents the peak power, and T_0 is the pulse duration. In this operating regime, ML operation can be maintained only at pulse energies below the limit implied by nonlinear phase shift [23, 171]. Figure 2.24 presents an output spectrum of the conventional soliton, revealing Kelly sidebands that result from the resonant enhancement of dispersive waves into discrete resonant waves [21, 172]. These sidebands are the unique behaviour of conventional solitons and need to be kept at low powers to maintain the stable mode-locked operation [21, 173]. Due to these constraints, the conventional soliton has a limited output pulse duration in hundreds of fs with pulse energy in the pJ level.

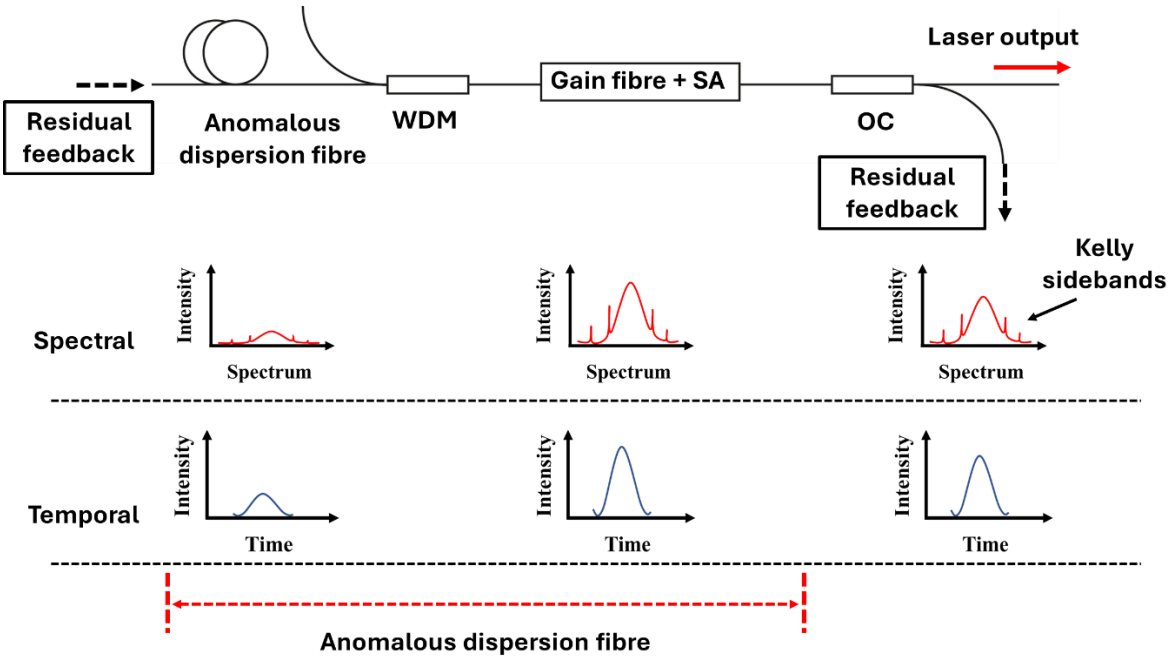

Figure 2.23 Idealised schematic presents dynamic spectral (top) and temporal (bottom) behaviours of an oscillating pulse in a conventional-soliton mode-locked laser. WDM: wavelength-division-multiplexer; SA: saturable absorber; OC: output coupler.

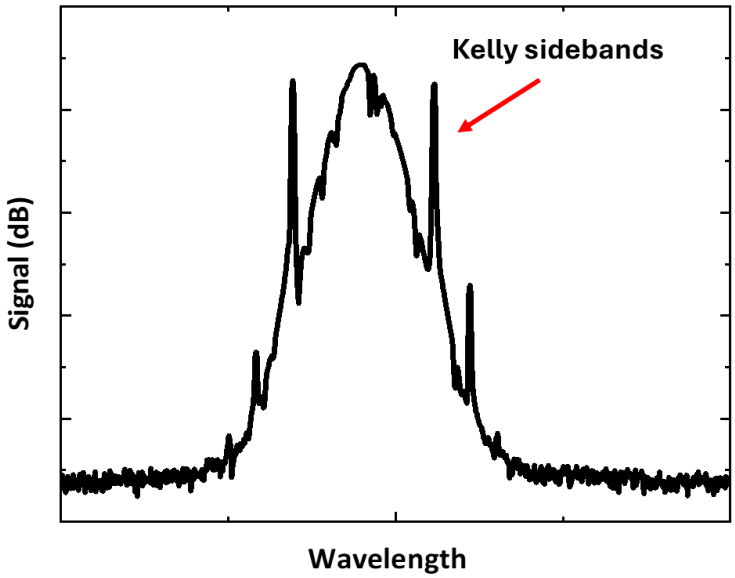

Figure 2.24 Output spectrum of conventional-soliton mode-locked laser.

2.5.2 Dispersion-managed-soliton mode-locked lasers

The limitations in conventional soliton can be mitigated by introducing dispersion compensation fibres (DCFs) in the cavity. In a cavity with the net dispersion close to zero, dispersion-managed/stretched-pulse solitons can be achieved [174]. The oscillating pulse is periodically stretched and compressed twice in each round-trip due to the comparable effect of normal and anomalous dispersion fibres [21]. This 'breathing' behaviour results in the variation of the pulse duration over an order of magnitude and can support pulse energies exceeding a few nJ [44, 45]. The output pulse chirp depends on the position of the output coupler. Furthermore, this output pulse can be compressed to achieve an ultrashort pulse in the range of hundreds of femtoseconds. Figure 2.25 represents an idealised schematic of pulse oscillation in the dispersion-managed cavity. Due to the presence of a dispersion map, the Kelly sidebands are suppressed [46]. It is worth noting that the temporal and spectral shapes of dispersion-managed pulses are close to Gaussian [23].

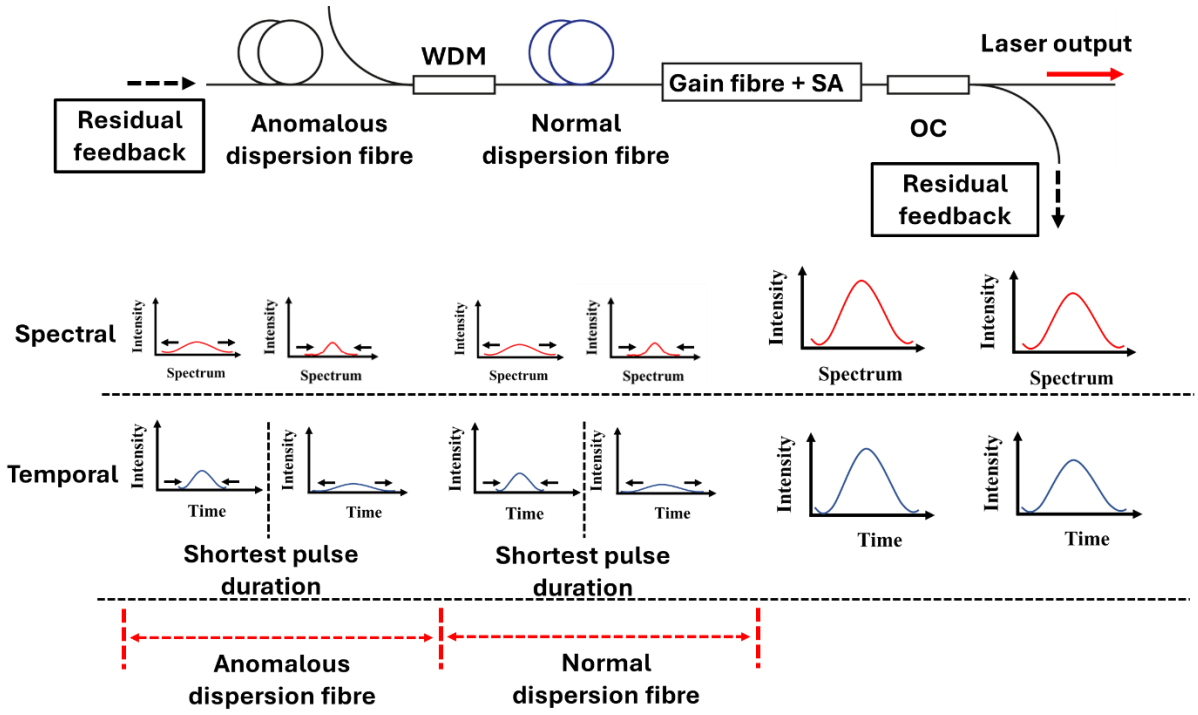

Figure 2.25 Idealised schematic presents dynamic spectral (top) and temporal (bottom) behaviours of an oscillating pulse in a dispersion-managed mode-locked laser. WDM: wavelength-division-multiplexer; SA: saturable absorber; OC: output coupler.

2.5.3 Dissipative-soliton mode-locked laser

Unlike other soliton types, dissipative solitons rely heavily on a balanced conservative effects (GVD and SPM) [58] and dissipative effects (spectral filter, gain, and loss) [59]. Dissipative solitons

have been demonstrated in both all-normal-dispersion cavities [175, 176] and net-normal dispersion cavities [177]. Figure 2.26 presents an idealised schematic of oscillating pulse behaviour in the dissipative-soliton regime. The spectral width expands due to nonlinearity in the fibre, while the temporal width obeys optical fibre dispersion, i.e., broadened by normal dispersion fibres. In each round trip, the temporal and spectral width are limited by a saturable absorber and spectral filter, thus balancing these effects [21]. Due to the dissipative effect, this soliton exhibits a steep edge and a flat-top profile [57, 178]. The typical spectral shape of the dissipative soliton is presented in Figure 2.27. Dissipative solitons have high tolerance to the accumulated nonlinear phase shift up to ~10π [57, 179]. Therefore, this soliton can generate significantly higher pulse energies than other soliton types, and the pulse duration can be compressed to achieve a pulse duration in the hundreds of fs level [59].

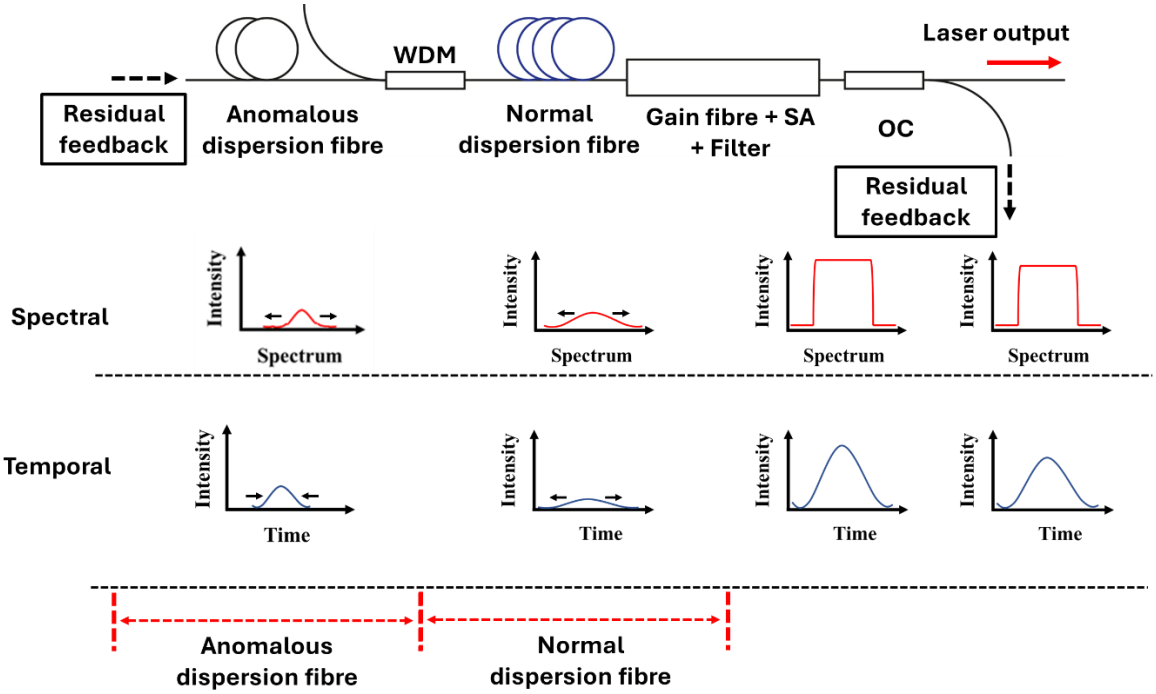

Figure 2.26 Idealised schematic presents dynamic spectral (top) and temporal (bottom) behaviours of an oscillating pulse in a dissipative-soliton mode-locked laser. WDM: wavelength-division-multiplexer; SA: saturable absorber; OC: output coupler.

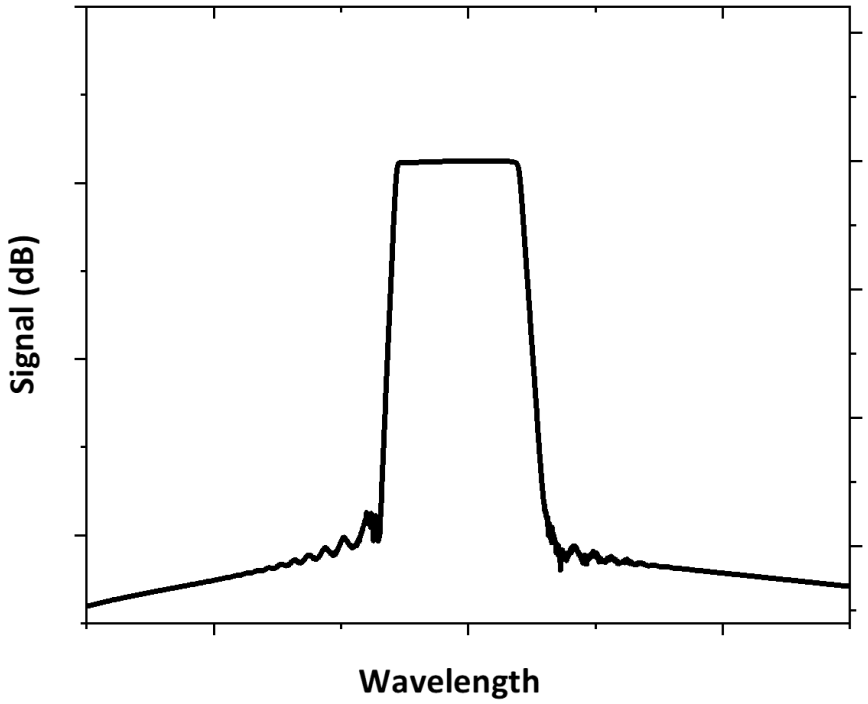

Figure 2.27 Output spectrum of dissipative-soliton mode-locked laser (from simulation).

2.6 Chirped pulse amplification

In this section, I explain chirped pulse amplification, which is an important technique to achieve desired pulse energies and has been used to support several applications.

2.6.1 Introduction

In 1985, chirped pulse amplification (CPA) was demonstrated to prevent self-focusing during pulse amplification with free-space setup [180]. This experiment achieved a high pulse energy of 2 mJ with a pulse duration of 1.5 ps. Thereafter, CPA became a promising technique that is commonly used to mitigate optical damage or nonlinear distortion in amplifiers [68-70]. CPA has recently been demonstrated to generate extremely high-power pulses, i.e., peak powers in the petawatt (10^{15} W) level [181, 182].

The CPA system consists of three main components: the pulse stretcher, the amplifier, and the pulse compressor [183]. Figure 2.28 presents an idealised schematic of the CPA system. At the input of the system, an incident pulse passes through the pulse stretcher, thus broadening in the temporal domain. Consequently, the peak power is reduced, mitigating an induced nonlinearity. The stretched pulse can be safely amplified in the amplifier to achieve higher pulse energies. Subsequently, the pulse is re-compressed to an ultrashort-pulse duration at the output end of the CPA system.

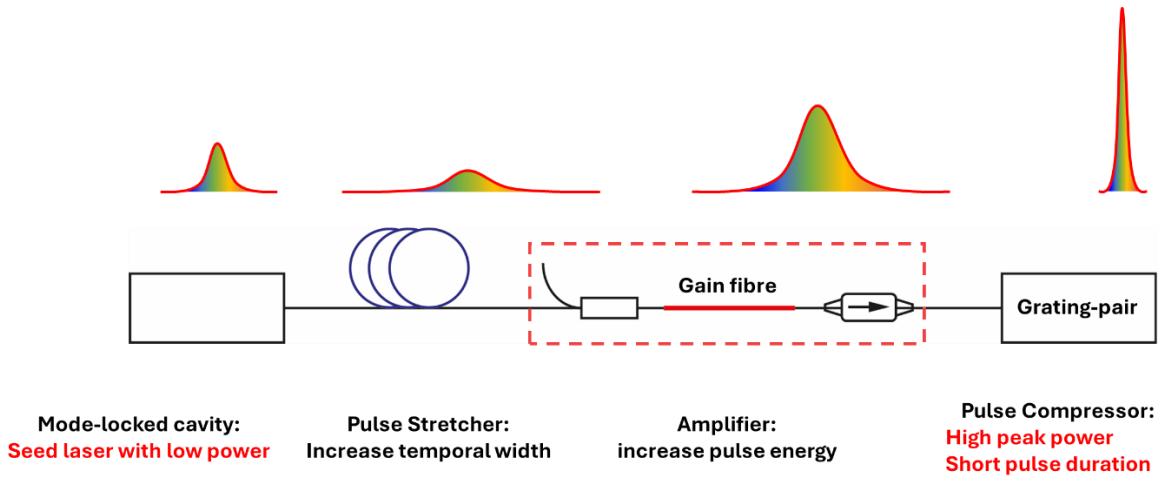

Figure 2.28 Idealised schematic of the chirped pulse amplification (CPA) system.

CPA systems can be built in a compact all-fiberised configuration. However, it requires careful design due to the confined spatial distribution and an extended propagation distance in the fibres [184, 185]. For example, an all-fiberised CPA system has been demonstrated to achieve a pulse energy of 1.25 μJ with a pulse duration of 297 fs, equivalent to a peak power of 4.2 MW [72].

2.6.2 Pulse stretcher

The pulse stretcher is the first component in a CPA system. Usually, the output power of the seed (mode-locked) cavity with a fixed optical bandwidth is controlled to have low power to minimise the nonlinearity. Each frequency component in the pulse has different group velocities in fibre. Hence, the pulse can be stretched by propagating through normal dispersive materials, i.e., dispersion compensation fibres, where the longer wavelengths travel faster than shorter wavelengths. The stretched pulse width ($\Delta\tau$) can be given by:

$$\Delta\tau = D\Delta\omega L \tag{2.36}$$

where $D = -(2\pi c/\lambda^2)\beta_2$ denotes chromatic dispersion, $\Delta\omega$ is the spectral width, and L represents the length of dispersive materials. In this thesis, experiments using the normal dispersion fibres, as stretchers, are reported.

2.6.3 Pulse compressor

At the output of the CPA system, a negative dispersion is introduced to the amplified signal to de-chirp the duration back to an ultrashort duration, i.e., close to the transform-limited value. Typically, in CPA, the pulse has high energy in the compressor and a grating-based compressor is a feasible solution for compressing high-energy pulse as it can prevent any possible nonlinearity.

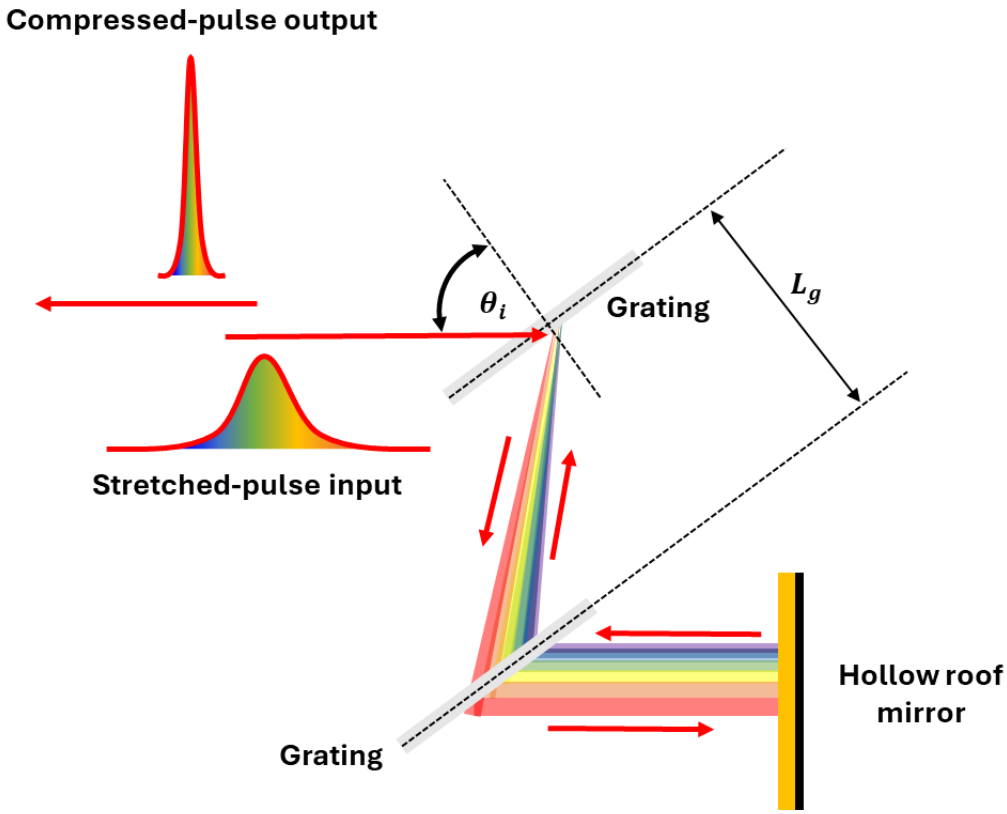

Figure 2.29 Idealised schematic of the grating-pair compressor.

Figure 2.29 presents a schematic of the grating-pair compressor in 'Treacy configuration' [186]. In this compressor, the input pulse is incident onto a transmission grating. Each frequency component of the pulse diffracts through the first grating with different angles and spreads the signal corresponding to the wavelength component. Another identical transmission grating is set at a separation distance (L_g) to stop the spreading. A reflective hollow roof mirror is used to reflect this signal back to the grating pair at a slightly different position and reverse the spectral chirp of the grating. The total optical path of each wavelength is different, i.e., longer wavelengths travel further than shorter wavelengths. Consequently, negative second-order dispersion can be induced, and the output pulse duration can be compressed. The group delay dispersion (GDD) of the grating-pair can be calculated by [187]:

$$GDD = -\frac{m^2\lambda^3 L_g}{2\pi c^2 \Lambda^2}\left[1-\left(-\frac{m\lambda}{\Lambda}-\sin\theta_i\right)^2\right]^{-3/2} \tag{2.37}$$

where m denotes the diffraction order (normally = -1), Λ represents the grating period, and θ_i represents an incident angle at the first grating. The separation distance can be varied to achieve the desired compressed pulse duration. This grating-pair configuration was used in the experiments reported in this thesis.

Chapter 3 Mode-locked thulium-doped fibre laser enabled by SESAM

In this chapter, I explain experiments undertaken to achieve ultrafast, high-energy pulses operating at a wavelength below 1900 nm, to support application in biomedical imaging, which is aligned with the aims of the InLightenUs project.

This chapter is comprised of four sections. The first section explains the background of mode-locked thulium-doped fibre lasers and their current achievements. The second section details relevant experiments to construct ML-TDFL enabled by a semiconductor saturable absorber mirror. This section also includes the development of continuous-wave pump sources at ~1560 nm. The third section discusses an improvement of the ML-TDFL to achieve a pulse energy exceeding 10 nJ. Additionally, the numerical simulation, to predict dynamic pulse behaviours, has also been explained in this section. The final section gives a summary of this chapter.

3.1 Background

High-energy (in tens of nJ level), ultrafast pulses at the short-wavelength infrared (SWIR) window, ranging from 1650-1900 nm, are preferred for deep-layer multi-photon biomedical imaging [10] due to the low attenuation and scattering in biomedical samples for this spectral region [11]. ML-TDFLs are promising for generating ultrafast pulses with a central wavelength extending from 1650-2100 nm [19, 20, 188], covering the SWIR window.

As discussed in Section 2.5, dissipative solitons are generated in ML cavities with net normal dispersion [59], offering high tolerance to nonlinear phase shifts [56]. These cavities are capable of generating a positively chirped pulse with a ps-pulse width and energy at the nJ-level [189]. Dissipative-soliton ML-TDFLs have been demonstrated using several saturable absorption techniques, including nonlinear polarisation rotation [62, 63, 66], carbon nanotubes [54, 55], graphene [47], and SESAM [53, 61, 190]. An outstanding net normal dispersion ML-TDFL has been demonstrated by Tang *et.al.* in 2015, generating a pulse energy of 8 nJ at a central wavelength of 1925 nm [60], with the temporal pulse width be compressed to 130 fs. However, this cavity only operates in a stable ML regime at wavelengths beyond 1900 nm, close to the water absorption peak [111]. Hence, it might not be suitable for biomedical imaging experiments. Moreover, the cavity consists of free-space optics, which might cause difficulties in improving its compactness for practical applications. A similar design was demonstrated in an all-normal-dispersion cavity with fluoride fibres (ZBLAN). This laser achieved stable ML operation with a pulse energy of 1 nJ at a central wavelength of 1833 nm [67]. However, fluoride-glass fibres are difficult to splice with standard silica-glass fibre. Hence, it is hard to develop this cavity for an all-fiberised design.

A ML-TDFL has been demonstrated in a fully-fiberised design using an in-house fabricated single-wall carbon nanotubes (SWNTs) SA, achieving a pulse energy of 4.8 nJ at a central wavelength of 1865 nm [191]. However, it might be challenging to be further developed this system for higher pulse energies due to the limited damage thresholds of the CNT-based SA [76]. Recently, our group have reported a fully-fiberised ML-TDFL laser demonstrated an outstanding performance in biomedical imaging experiments [17]. However, this 1-nJ pulse at a central wavelength of 1840 nm needs to be amplified through multi-stage amplifiers in a CPA system to achieve pulse energy of 105 nJ with a compressed pulse duration of 416 fs (peak power of ~252 kW), sufficient peak power for biomedical imaging experiments. The CPA needs to be carefully designed to efficiently amplify the pulse [72, 74]. It is still challenging to achieve high-energy pulses at short wavelengths <1900 nm directly from the cavity due to the quasi-three-level nature of the TDF [112]. The cavity needs to be optimised to provide the appropriate nonlinearity, dispersion, and filtering effects [59, 65]. The following sections in this chapter will discuss the detailed information of the experiment and numerical simulation of ML-TDFL to achieve high-energy, ultrafast pulses at short wavelengths using an all-fiberised cavity design.

3.2 SESAM-based thulium mode-locked fibre laser

In this section, I explain relevant experiments to study dissipative-soliton ML-TDFL. This section also includes the development of pump sources at wavelength ~1560 nm, which will be used in experiments through my PhD study.

3.2.1 Develop of continuous wave pump source

This section explains the development of CW laser sources that provide efficient output signals near 1560 nm which can be used as a pump source to enable SWIR emission in ML-TDFL.

3.2.1.1 Erbium-doped fibre laser

At the start of my PhD, there was an existing erbium-doped fibre laser (EDFL) in our laboratory. This laser was constructed by a former PhD student in the research group. The schematic of the EDFL is presented in Figure 3.1. The EDFL was pumped by two multimode-CW laser diodes (L3-PUA41, JSDU) operating at 915 nm. The pump was coupled into the EDFL through a (2+1) x 1 pump-signal combiner, providing the maximum combined power of 13 W. The signal input pigtail of this combiner was connected to a fibre Bragg grating (FBG) with a high reflectivity of ~99% at ~1560 nm. The output pigtail of this combiner was connected to a 5-m length of doubled-clad erbium/ytterbium co-doped fibre (EDF), which provides optical gain around 1560 nm. The EDF core/cladding size is 12/130 μm with a numerical aperture (NA) of 0.2/0.46. An output coupler

(OC) was connected at the EDF end, providing a reflectivity of ~6% at ~1564 nm with a FWHM of 1.2 nm and creating a complete round-trip oscillation in this fiberised laser cavity.

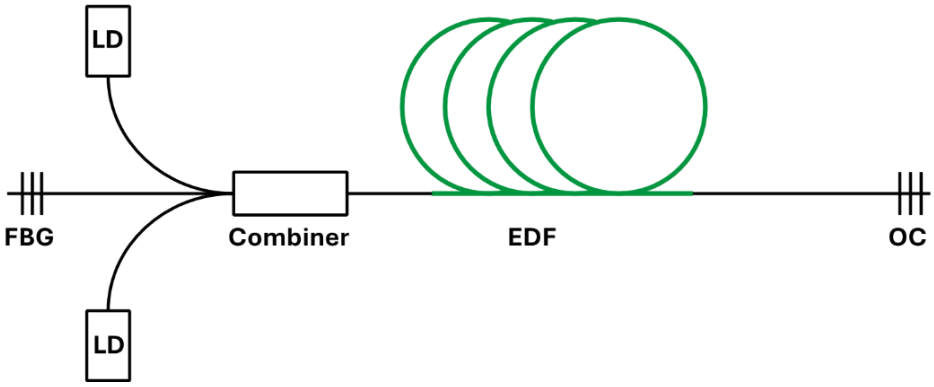

Figure 3.1 Schematic of the erbium-doped fibre laser (EDFL). FBG: fibre Bragg grating; OC: output coupler; EDF: erbium/ytterbium co-doped fibre; LD: laser diode.

Figure 3.2(a) presents an amplified spontaneous emission (ASE) spectrum of the EDF. The ASE reveals its spectral gain bandwidth, extending from 1540 to 1640 nm with a peak near 1560 nm. The EDFL laser threshold was found at pump power of 2 W. Figure 3.2(b) shows an output spectrum of the EDFL at ~1563 nm with the optical signal-to-noise ratio (OSNR) of ~50 dB. The slope efficiency of this EDFL was 22.7%, as presented in Figure 3.2(c), yielding a maximum output power of 2.8 W.

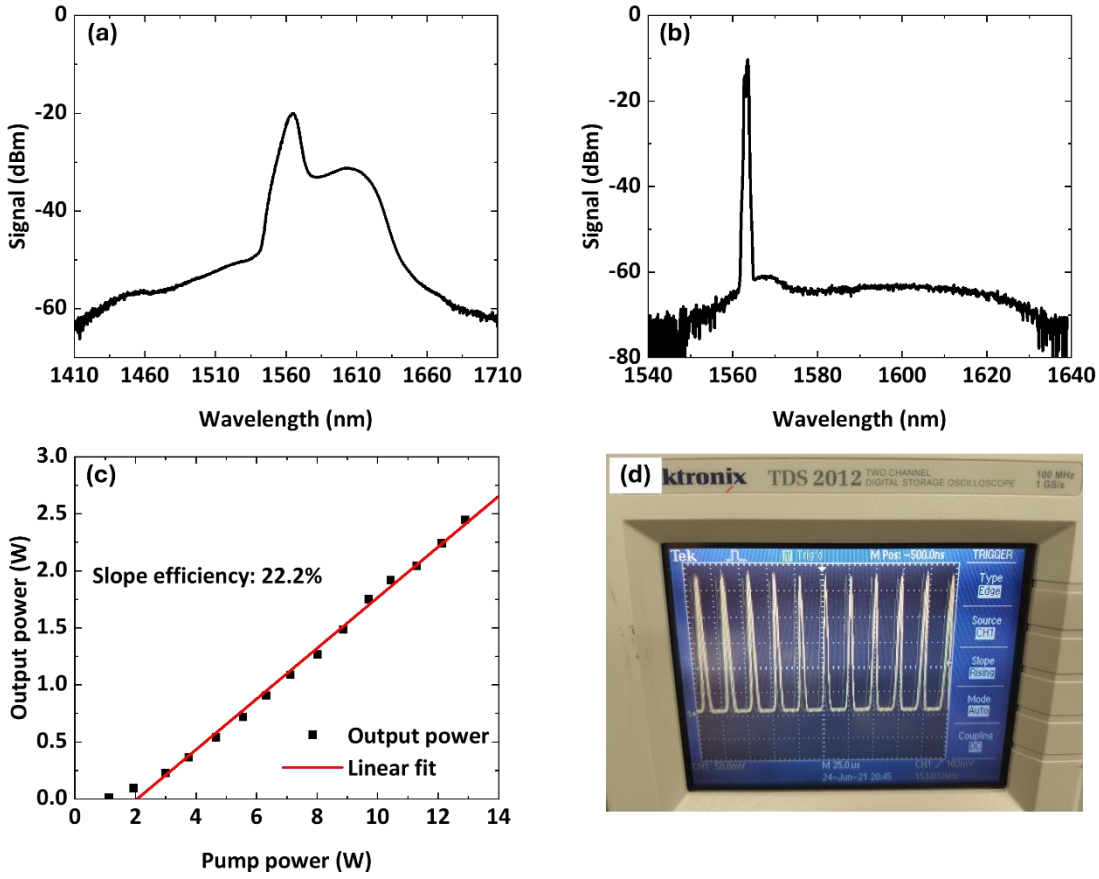

Figure 3.2 (a) Amplified spontaneous emission (ASE) spectrum of the erbium/ytterbium co-doped fibre (EDF), (b) output spectrum of the erbium-doped fibre laser (EDFL), (c) output power of the EDFL, and (d) the oscilloscope trace of the EDFL output signal with the pump powers below 3 W

The EDFL was capable of providing a stable CW signal at 1563 nm with high output power. However, self-pulsing behaviour was observed from this EDFL while operated with pump powers below 3 W, detected using a 10-GHz InGaAs photodiode (ET-5000F, EOT), as observed on an oscilloscope shown in Figure 3.2(d). This behaviour might hinder the capability of ML-TDFL study, especially once operating at low pump powers. I resolved this issue by changing to a master oscillator fibre amplifier (MOFA) design, which is explained in the next section.

3.2.1.2 Erbium-doped master oscillator fibre amplifier

An erbium-doped master oscillator fibre amplifier (EDFA) was built by modifying previously presented EDFL. The FBG was replaced by a fiberised isolator connected to a seed laser. The CW seed signal at a central wavelength of ~1563 nm with a low power of ~10 mW was provided by a multi-channel fibre optical mainframe (7900B system, ILX Lightwave). The OC at the output end of the system was replaced by an isolator and a fibre output patch chord. A schematic of the EDFA is shown in Figure 3.3.

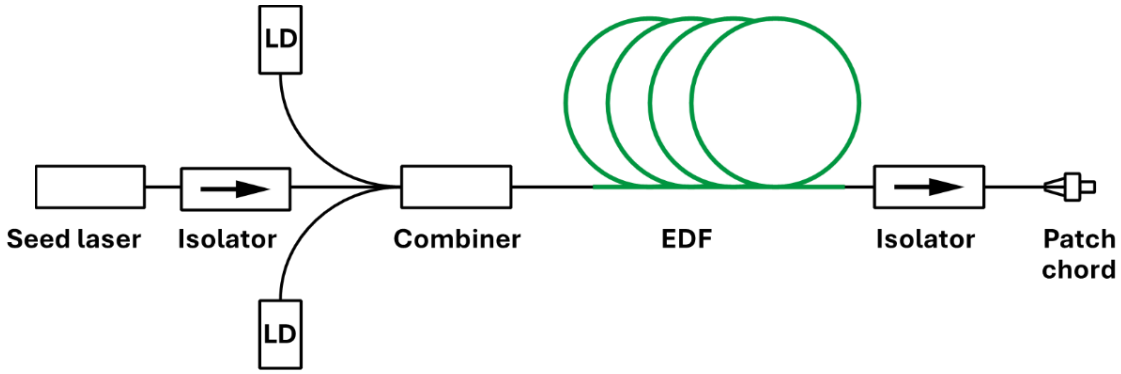

Figure 3.3 Schematic of erbium-doped master oscillator fibre amplifier (EDFA). EDF: erbium/ytterbium co-doped fibre; LD: laser diode.

The CW seed laser spectrum is illustrated in Figure 3.4(a), presenting a signal at a central wavelength of ~1563 nm with an OSNR of 50 dB. This low-power (~10 mW) CW signal was amplified through the EDFA and achieved a high-power signal at a central wavelength of ~1563 nm with an OSNR of 45 dB, as presented in Figure 3.4(b). The output efficiency of the EDFA is depicted in Figure 3.4(c) with a slope efficiency of 17.8% and achieved the maximum output power of ~2 W.

The EDFA has a lower slope efficiency and maximum output power compared to the previous EDFL. However, this EDFA provides a stable CW output without any self-pulsing behaviour. Figure 3.4(d) shows an oscilloscope trace at low pump powers, indicating a stable CW output signal.

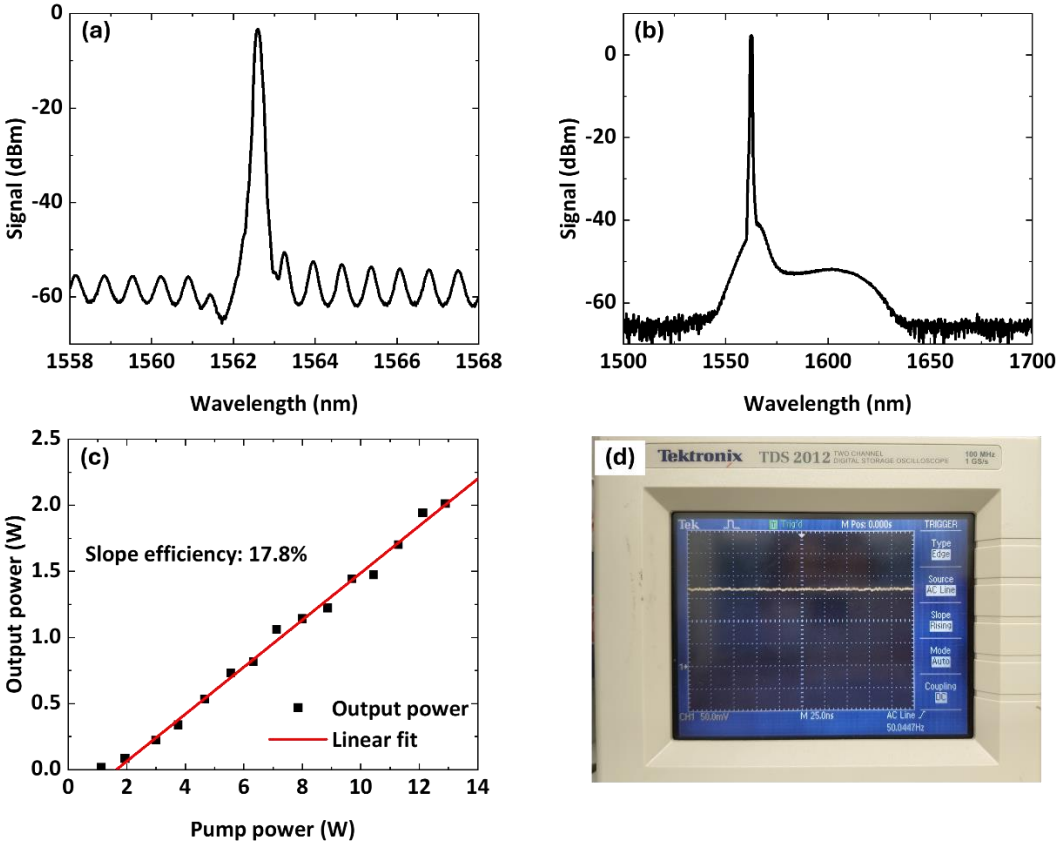

Figure 3.4 (a) Spectrum of the seed laser, (b) output spectrum of the erbium -doped master oscillator fibre amplifier (EDFA), (c) output power of the EDFA, and (d) oscilloscope trace of the EDFA at pump powers below 3W

3.2.2 Mode-locked thulium-doped fibre laser

A schematic of an all-fiberised ML-TDFL is presented in Figure 3.5(a). The CW-seeded pump was provided by the EDFA, developed in the previous section. The pump was coupled into the TDF through a 1560/1960 nm wavelength-division-multiplexer (WDM). A 0.95-m length of the ORC fabricated TDF was utilised to enable the SWIR emission. This gain fibre was specially designed with a core/cladding diameter of 8.3/100 µm, 0.2 NA, matched well with commercially available single-mode fibres (SMF; $\beta_2 = -0.056\ ps^2/m$ at 1.9 µm) [191], and had high pump absorption (~20 dB/m at 1580 nm) [192]. An output coupler (OC) was connected to extract 75% of the oscillating energy as a laser output. The residual pigtail was spliced to an in-line polarisation controller (PC) to adjust the polarisation of the oscillating pulses. A circulator (CIR) was employed to ensure a unidirectional oscillation in this cavity. A SESAM (SAM-1920-36-10ps-1.3-0, Batop) was attached to the flat fibre-end facet thus providing a non-saturable reflection of 60% and a modulation depth of 20%. This SESAM has limited reflectivity wavelengths ranging from ~1850-2000 nm [152]. The net cavity dispersion can be controlled by employing a 4.7-m length of dispersion compensation fibre (DCF; UHNA4, Coherent; $\beta_2 = 0.12\ ps^2/m$ at 1.9 µm) [193]. This cavity has a total cavity length

of 11.1 m with a net dispersion of 0.2 ps^2. The cavity was set on a 45 x 45 cm breadboard, as shown in Figure 3.5(b).

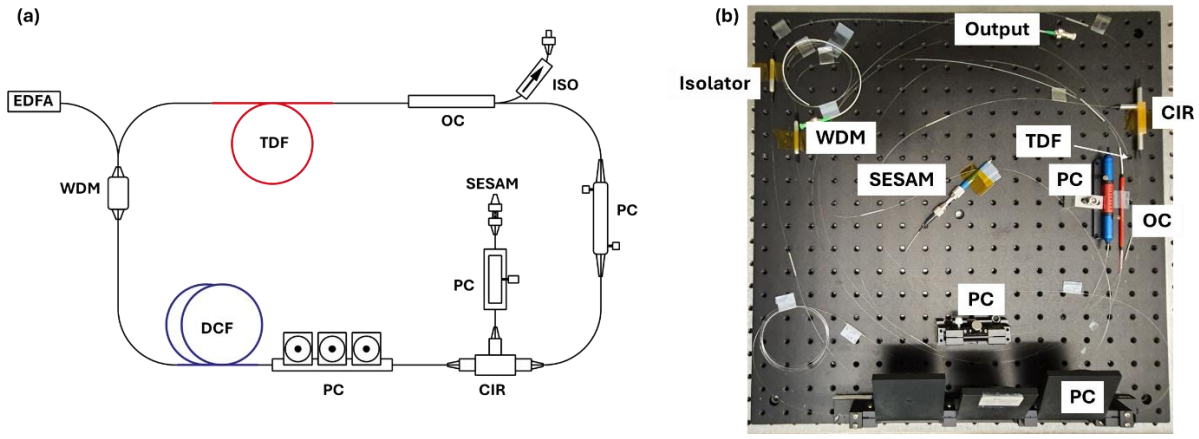

Figure 3.5 (a) Schematic of the mode-locked thulium-doped fibre laser (ML-TDFL), and (b) picture of the ML-TDFL. WDM: wavelength-division multiplexer; TDF: thulium-doped fibre; OC: output coupler; PC: polarisation controller; DCF: dispersion compensation fibre; CIR: circulator; EDFA: erbium-doped master oscillator fibre amplifier; SESAM: semiconductor saturable absorber mirror.

Output spectra at different powers are presented in Figure 3.6(a), exhibiting a sharp-edge, flat-top shape as typical for the dissipative soliton [21, 175]. The spectral bandwidth increased with higher output powers and achieved a 3-dB bandwidth of 35.1 nm with a central wavelength of 1875 nm at the maximum power. The ML laser threshold was found at the pump (EDFA) power of 709 mW, generating an output power of 45.7 mW, as presented in Figure 3.6(b). The output power increased with pump power and reached the maximum output power of 119.3 mW at a pump power of 946 mW, yielding a slope efficiency of 34.5%. The ML became unstable with higher pump powers beyond this point.

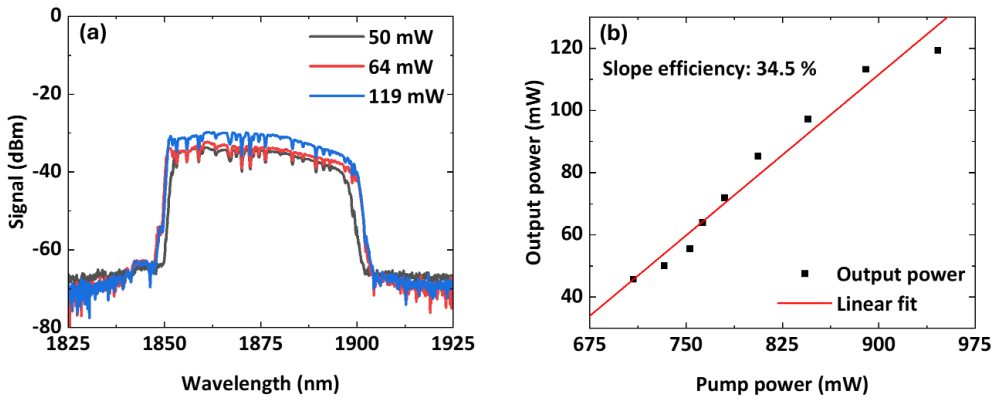

Figure 3.6 (a) Output spectra with different output powers, and (b) output power efficiency of the cavity.

An oscilloscope trace of output pulses was acquired using a 10-GHz InGaAs photodiode (ET-5000F, EOT) with a 200-MHz oscilloscope (DSO-X- 2024A, Agilent). Figure 3.7(a) presents the

result, revealing the stable pulse train with a round-trip time of 54.2 ns, corresponding to the repetition rate of 18.45 MHz. This result is consistent with the estimated value calculated from the total cavity length. Figure 3.7(b) presents a 40-kHz span of a radio frequency (RF) spectrum acquired by an RF spectrum analyser (E4446A, Agilent) with a resolution bandwidth of 3 Hz. The RF spectrum had a high signal-to-noise ratio (SNR) of ~66 dB at the fundamental frequency near 18.44 MHz, indicating stable single pulse ML operation without noise. The sideband peaks of the RF spectrum can be attributed to an effect of relaxation oscillation [194]. Figure 3.7(c) presents a 1-GHz span range spectrum without any notable parasitic oscillation in the cavity. Hence, the output pulse energy was 6.5 nJ.

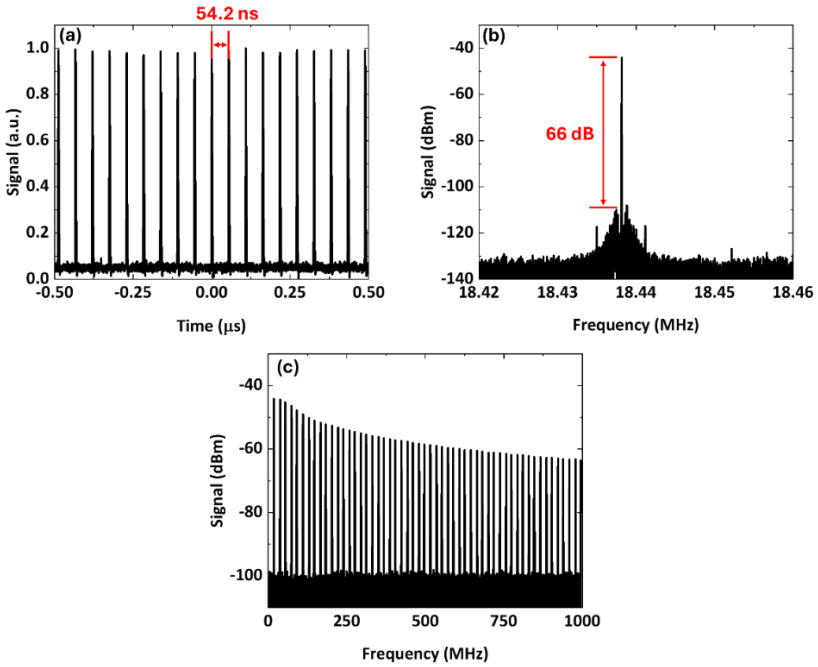

Figure 3.7 (a) Oscilloscope trace of the output pulses, (b) radio frequency (RF) spectrum of the output with the span range of 40 kHz and the resolution bandwidth 3 Hz, and (c) the RF spectrum for 1 GHz spanning range with resolution bandwidth 3 kHz.

The temporal pulse width was characterised by an autocorrelator (pulseCheck NX-150, APE). Figure 3.8(a) presents an autocorrelation (ACF) trace of uncompressed pulses. The ACF pulse had a width of 12 ps, equivalent to an actual pulse duration of 8.5 ps based on a Gaussian-shape assumption. The pulse was compressed by a home-built grating-pair compressor, as shown in Figure 3.9. A SMF patch chord was connected to deliver the output signal from the cavity to a fibre connector, set on a 3-axis stage, along with an aspherical lens (C220TMD-C, Thorlabs; focal length = 11 mm) to collimate the output beam. The beam was reflected by a gold-coated mirror (PF10-03-M01, Thorlabs) to a pair of 900 line/mm transmission gratings. The first grating was set at the optimum angle of ~54.1° to the incident beam, while the second grating was mounted parallel to the first on a translational stage. Therefore, the separation distance between these

gratings could be adjusted to achieve the shortest compressed pulse duration. It is worth noting that a half-waveplate was employed in front of the gold-coated mirror to optimise the grating transmission. This compressor was set on a 30 x 60 cm breadboard, as presented in Figure 3.9(b). Figure 3.8(b) presents a compressed ACF trace with a width of 364 fs, equivalent to the Gaussian-shape pulse duration of 258 fs.

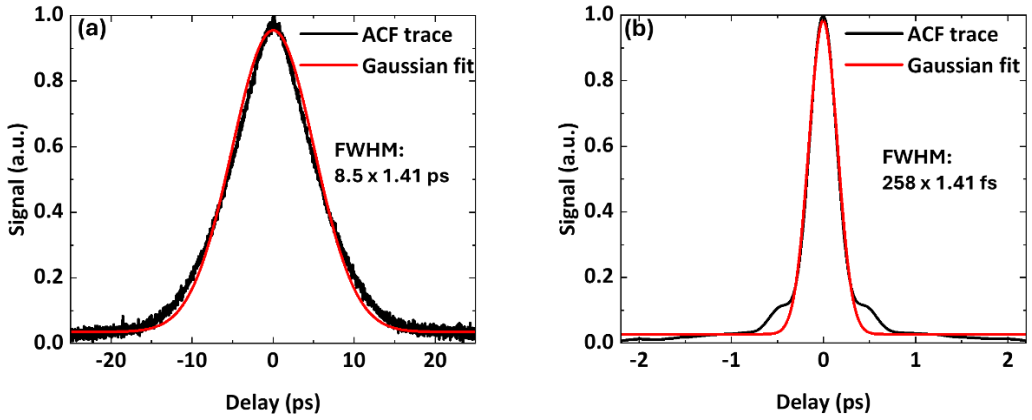

Figure 3.8 (a) Uncompressed pulse duration, and (b) compressed pulse duration of the output pulse.

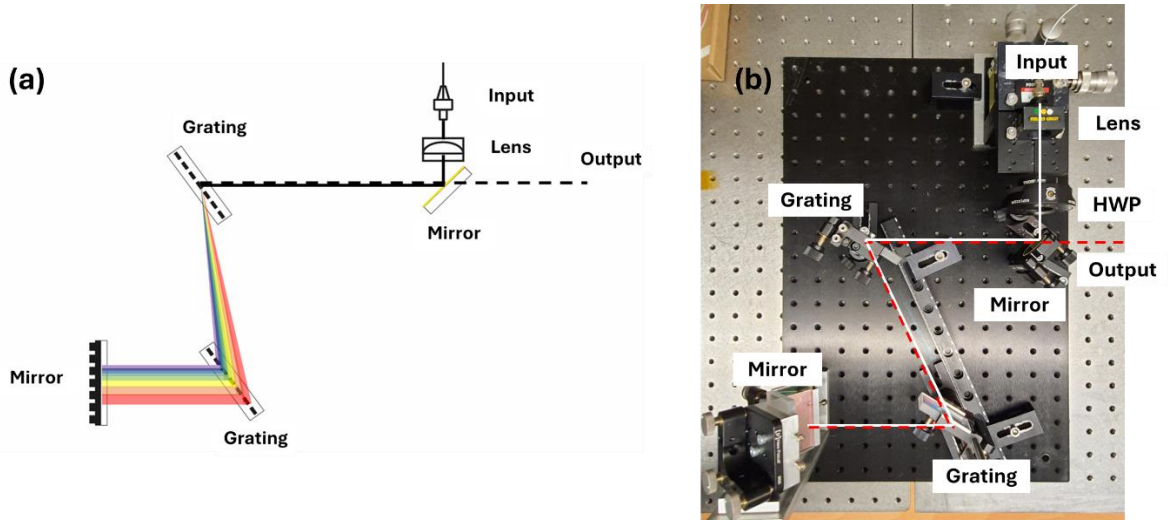

Figure 3.9 (a) Schematic of the grating-based pulse compressor, and (b) picture of the pulse compressor (white solid line shows the input signal path in the compressor; red dash line shows the reflected signal path with fixed elevation; HWP: half-waveplate.

By adjusting the PCs, the central wavelength can be varied within a range from 1866-1875 nm. Figure 3.10 presents the ML output spectra with various PC positions at a fixed pump power.

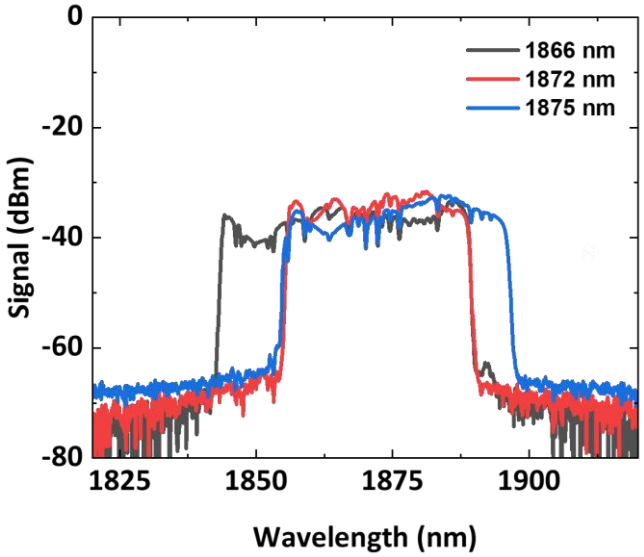

Figure 3.10 Output spectra show the capability of wavelength tuning by adjusting the polarisation controller in the cavity. This experiment was undertaken with the pump power of ~760 mW

The influence of the net cavity dispersion on the mode-locking was explored by varying the DCF length while the rest of the cavity was kept unchanged. Figure 3.11(a) presents the output spectra at different net cavity dispersions, operating at a fixed pump power. The spectrum was narrowing with increasing dispersions, shown in Figure 3.11(b), as expected for the dissipative-soliton behaviour [55].

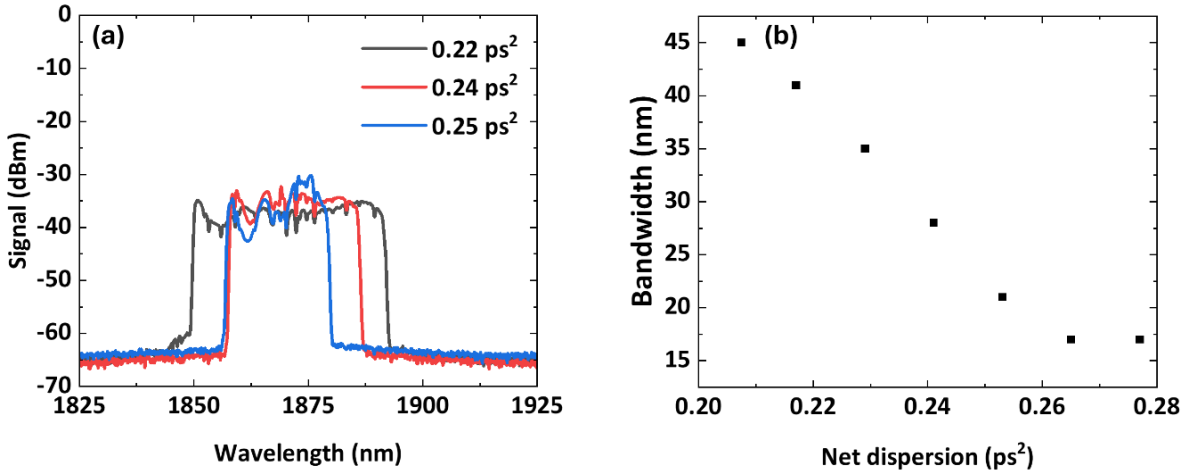

Figure 3.11 (a) Output spectra with different net dispersions, and (b) the 10 dB bandwidth with different net dispersions. The experiment was undertaken with the pump power ~760 mW.

3.3 High-pulse-energy thulium mode-locked fibre laser enabled by SESAM

In this section, I explain an experiment to optimise the SESAM-based ML-TDFL to achieve high pulse energies. This section also includes a numerical simulation to predict the dynamic pulse behaviour of the oscillating pulses.

3.3.1 High pulse energy mode-locked thulium-doped fibre laser

A schematic of a 10-nJ-level, ML-TDFL is presented in Figure 3.12(a). Compared to the cavity in previous section, the TDF length in this cavity was shortened to 0.65 m to prevent longer wavelength generation through the re-absorption process [112] and to support the generating of higher pulse energies [65]. It is worth mentioning that the ML operation cannot be achieved with shorter TDF lengths. A fast-axis-blocked PM isolator was employed to function as a polariser in a Kerr shutter, utilising the NPR as explained in Section 2.3.2.3 [156].This configuration supports a combined SA methods that would help to initiate and stabilise the ML operation by tuning the PCs. The net cavity dispersion was controlled by a 5-m length of the DCF. This cavity, constructed on the breadboard as presented in Figure 3.12(b), has a total length of 11.6 m and a dispersion of 0.24 ps^2.

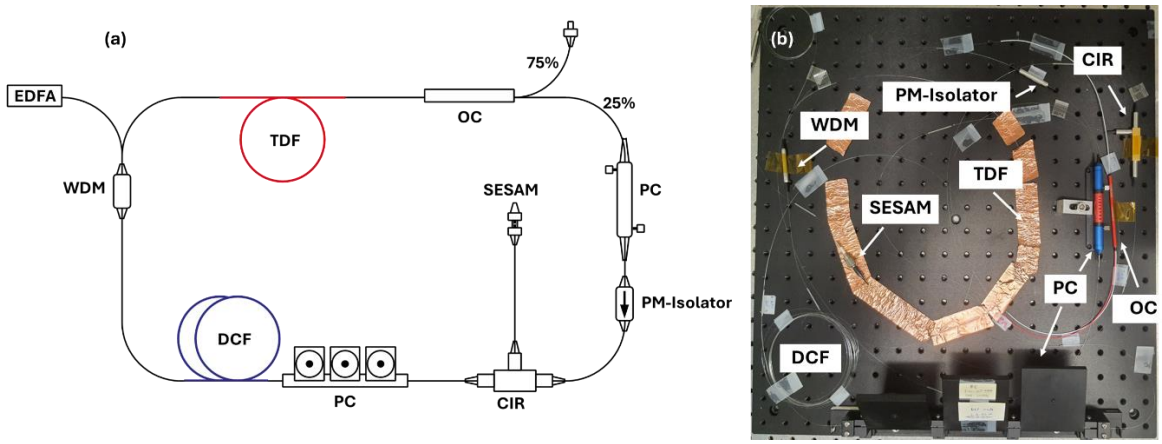

Figure 3.12 (a) Schematic of the high-pulse-energy, mode-locked cavity, and (b) picture of the cavity WDM: wavelength-division multiplexer; TDF: thulium-doped fibre; OC: output coupler; PC: polarisation controller; PM-Isolator: polarisation-maintaining isolator; DCF: dispersion compensation fibre; CIR: circulator; EDFA: erbium-doped master oscillator fibre amplifier; SESAM: semiconductor saturable absorber mirror.

Stable ML operation was achieved at a pump power of 1 W, generating an output power of 102.6 mW. The output power increased at higher pump power with a slope efficiency of 24.8%, and provide a maximum output power of 180.8 mW, as presented in Figure 3.13(a). The output spectrum was gradually expanding at higher output power and had a central wavelength of

1875 nm with a 10-dB bandwidth of 26.9 nm (3-dB bandwidth of 15.1 nm) at the maximum output power as presented in Figure 3.13(b).

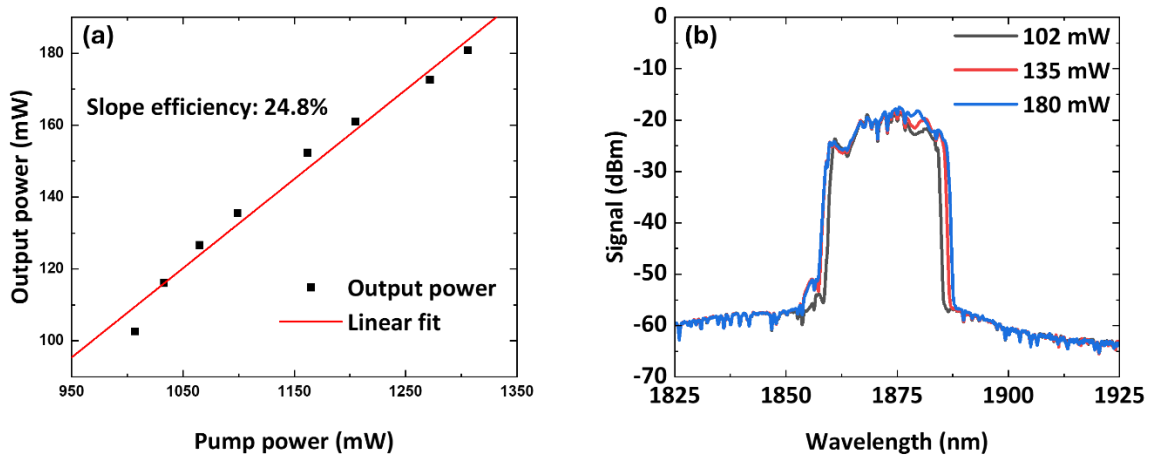

Figure 3.13 (a) output power efficiency of the cavity, and (b) output spectra at different powers.

The RF spectrum, acquired with a span of 50 kHz at a resolution bandwidth of 3 Hz, is presented in Figure 3.14(a). The spectrum reveals the fundamental repetition frequency near 17.57 MHz with an SNR of 85 dB. The result indicates a stable, single-pulse ML operation. Moreover, the repetition rate agrees with the estimated value, calculated based on the total cavity length. Figure 3.14 (b) presented a 1-GHz spanning RF spectrum without any parasitic instability. Hence, the output pulse energy can be calculated to be 10.3 nJ.

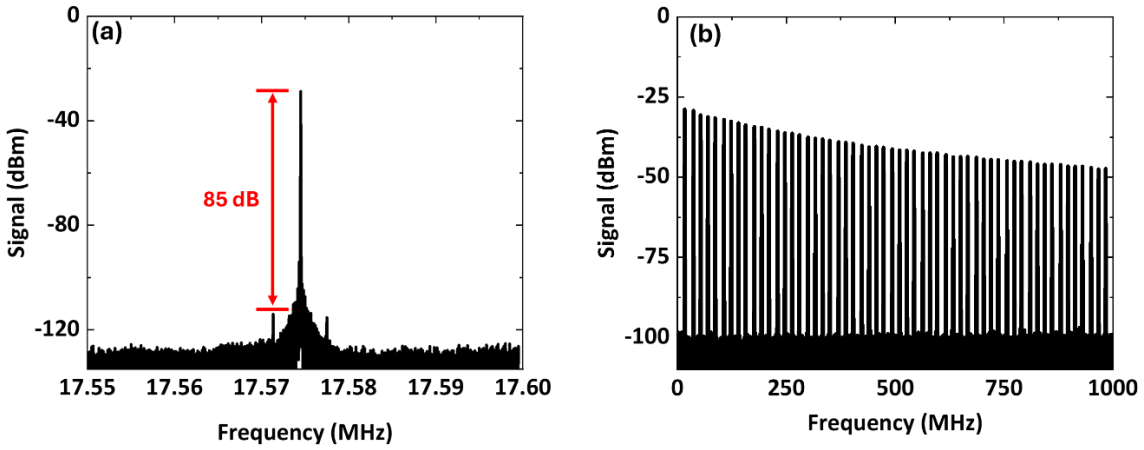

Figure 3.14 (a) radio frequency (RF) spectrum of the output with the span of 50 kHz and a resolution bandwidth of 3 Hz, and (b) the RF spectrum for 1 GHz spanning range with a resolution bandwidth of 3 kHz.

Figure 3.15(a) presents an ACF trace of uncompressed pulses with a width of 17.5 ps, equivalent to a Gaussian-shaped pulse width of 12.4 ps. The pulse could be compressed by the grating-pair compressor to 548 fs as shown in Figure 3.15(b). It is worth mentioning that the time-bandwidth

product (TBP) of the compressed pulse is 1.59 times larger than the Fourier transform limit, which might be caused by a nonlinear chirp that cannot be compensated by the compressor [195]. The pulse compressibility can be improved by managing higher-order dispersion in the cavity [49, 64].

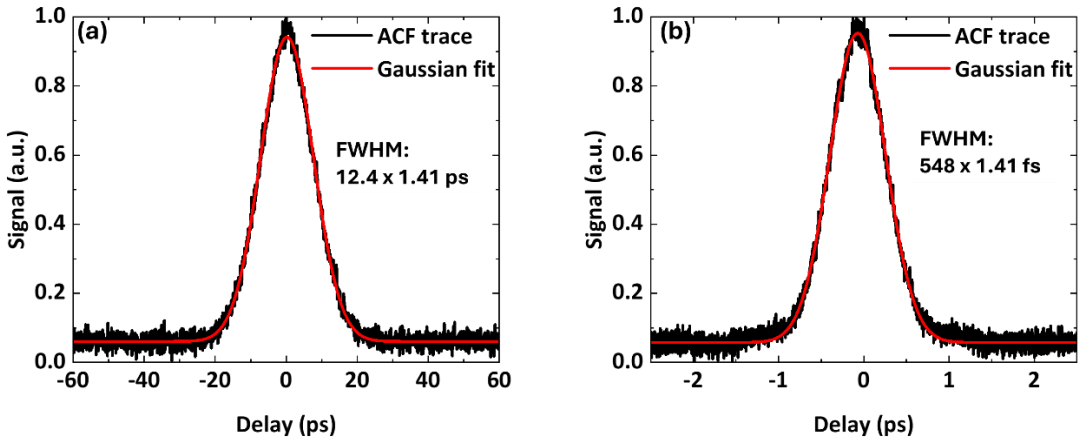

Figure 3.15 (a) Uncompressed pulse duration, and (b) compressed pulse duration of the output pulse.

3.3.2 Simulation of the dynamic pulse behaviour

Detailed information of the fibres/components from the experiment were considered as boundary conditions in a simulation model. Oscillating pulses in the cavity were theoretically predicted using a commercial simulation software (Fiberdesk), with the pulse behaviour determined using the nonlinear Schrödinger equation, solving through a split-step Fourier method. In the simulation, the TDF was assumed to provide a Gauss-shaped gain profile with a central wavelength of 1900 nm with a bandwidth of 150 nm. The PM-isolator was also assumed to induce an NPR with a modulation depth of 20% and a saturation power of 1 kW, i.e., maximum transmission (assumed to be 100%) is achieved once interacting with pulses at the saturation power. The SESAM provided an unsaturated reflectivity of 60%, a modulation depth of 20%, a saturation fluence of 50 μJ/cm^2, and a temporal response of 10 ps. This SESAM has a limited reflection bandwidth. Hence, we assumed that the pulse experiences Gaussian-shaped filtering at a central wavelength of 1871 nm with a bandwidth of 35 nm.

The seed pulse was defined to have an initial pulse energy of 10 pJ and a pulse duration of 1 ps. In the simulation, a seed pulse makes several round-trips through the modelled cavity and experiences the effects of dispersion, nonlinearity, gain, and loss from the various sections. Stable ML results were recorded once the simulation model has returned steady state output pulse properties. When it converges, the oscillating signal achieves a stable dissipative-soliton

pulse behaviour, exhibiting a flat-top, sharp-edge spectrum [175]. The modelled output spectrum has a bandwidth of 23.9 nm and is comparable to the experimental result, as presented in Figure 3.16. The red curve in Figure 3.17(a) presents dynamic variation for the spectral width while the pulse is oscillating inside the cavity. It reveals a balanced spectral gain-loss mechanism that is crucial for the dissipative-soliton operation. The spectrum is broadening in the passive and gain fibres, dependent upon the nonlinearity and optical gain, respectively. It is worth mentioning that the spectrum is greatly expanded in the DCF, which has a relatively small core compared to normal SMF fibres, resulting in higher induced nonlinearity inside this fibre. Once the pulse interacts with SAs (NPR and SESAM), the spectrum is narrowed corresponding to their saturable absorption mechanisms, i.e., low-power parts of the oscillating pulse are blocked due to the SA effect [75]. The spectrum is also further limited at the Gaussian filter function, employed at the SESAM in this simulation model, fulfilling the balanced dissipative effect. The oscillating pulse duration is presented as the blue curve in Figure 3.17(a). The duration is gradually compressed in anomalous-dispersion fibres (SMF and TDF) and is stretched in the normal-dispersion DCF section. This behaviour indicates that the oscillating pulse has positively chirped as expected for the dissipative soliton [21]. The pulse duration is also shortened at SAs and filters, where low-intensity parts (especially at the pedestal) of pulses are eliminated. In the steady state, the oscillating signal has a pulse duration of 13.2 ps at the OC, comparable to the measured value in the experiment (12.4 ps). The difference in these values might be caused by the negative-dispersion SMF fibre connections that compressed the pulse, while delivering it for autocorrelation measurement. Oscillating pulse energy is presented in Figure 3.17(b), showing high power amplification in the TDF gain section and sharply reduced at the OC, where 75% of oscillating energy was extracted to be delivered as a laser output. The oscillating pulse has a maximum power of 19.1 nJ, equivalent to an output pulse energy of 14.3 nJ. It is worth mentioning that the difference between simulated and measured results might possibly be caused by extra splice losses or component insertion losses that are not precisely factored into the model.

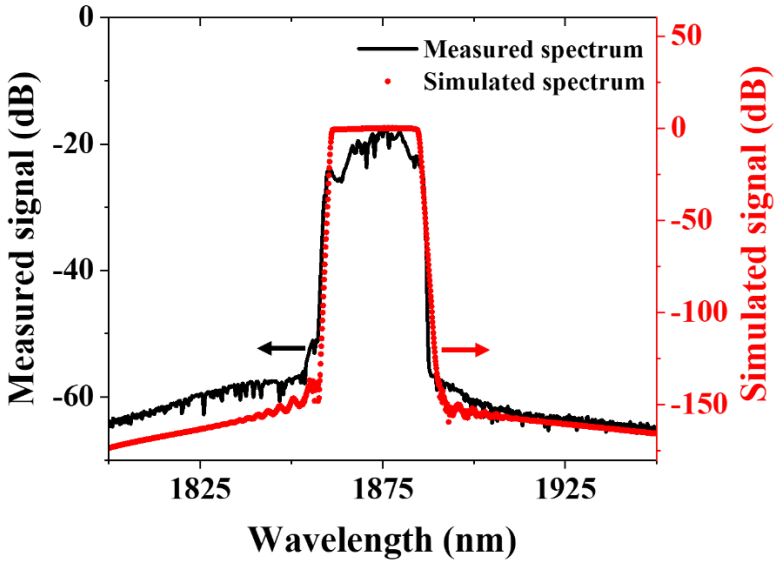

Figure 3.16 Comparison of (solid line; black) measured and (dotted line; red) simulated spectrum of the mode-locked cavity.

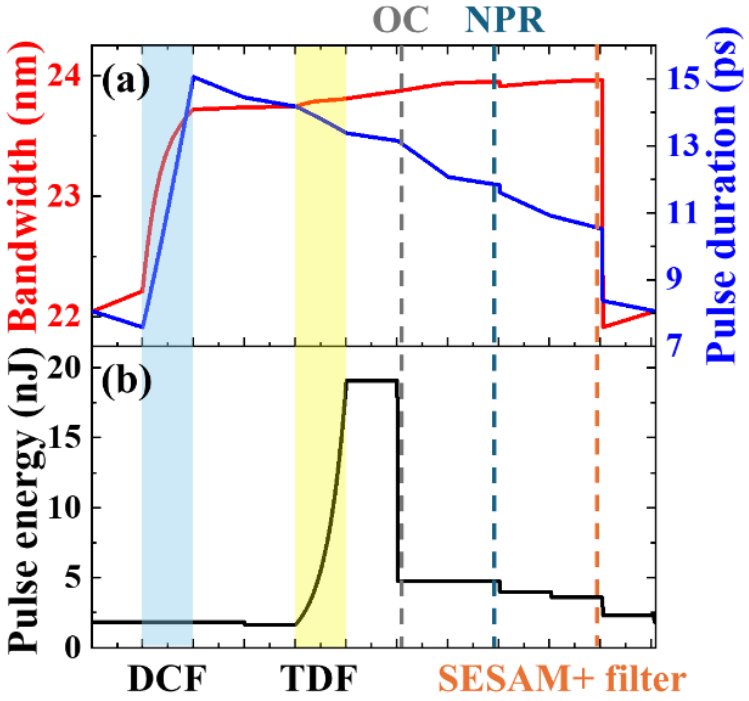

Figure 3.17 Simulated dynamic pulse behaviours of (a) (red curve) spectral bandwidth and (blue curve) pulse duration, and (b) oscillating pulse energy. DCF: dispersion compensation fibre; TDF: thulium-doped fibre; OC: output coupler; NPR: nonlinear polarisation rotation; SESAM: semiconductor saturable absorber mirror.

3.4 Summary

In summary, I presented my work on the development a light source to supply CW signal at a central wavelength of ~1560 nm, which can be used as a pump for ML-TDFL. Systems with these configurations (EDFL and EDFA) were employed for the subsequent sections of the thesis.

Additionally, I demonstrated the development of SESAM-based, all-fiberised ML-TDFL that achieves 10nJ-pulse energy at wavelengths below 1900 nm. This was achieved by using an ORC fabricated TDF and I showed that this laser has excellent potential to support biomedical imaging applications. Mode-locking was enabled by the combined SA effect between NPR and SESAM, providing a maximum pulse energy of 10.3 nJ at a central wavelength of 1875 nm. The output pulse has a Gaussian-shape pulse duration of 12.4 ps and can be compressed down to 548 fs. The dynamic pulse behaviours of the oscillating pulses were also predicted with a simulation model, based on the nonlinear Schrödinger equation.

Chapter 4 Mode-locked thulium-doped fibre laser enabled by CNT saturable absorber

In this chapter, I explain experiments to study a mode-locked thulium-doped fibre laser enabled by carbon nanotube saturable absorber. This all-fiberised cavity is expected to provide a stable ML operation at a short SWIR wavelength, which can be used as a seed in the imaging laser system to support biomedical imaging experiments.

The CNT-SAs, studied in this chapter, were fabricated by a research group at Cambridge Graphene Centre (CGC), University of Cambridge, led by Professor Andrea C. Ferrari. Under the research collaboration, the samples were delivered to our group. I characterised the optical properties of these samples and implemented them in the cavity to enable ML operation.

This chapter is structured into four sections. The first section discusses the background of material-based SA in ML-TDFL. In the second section, experiments to characterise the optical properties of provided CNT-SAs including linear and nonlinear transmission, are detailed. The development of a CNT-based ML-TDFL, as a new seed laser for biomedical imaging laser, is explained in the third section of this chapter. A summary is given in the final section.

4.1 Background

In passive mode-locking, SA is a key element to enable pulse-mode operation by enhancing high-power pulses and eliminating low-power noise [75]. As discussed previously, SA can be essentially categorised into two types: material-based SA (using material absorption) and fibre-based SA (using Kerr-nonlinearity) [77], as explained in Section 2.3.2.

ML-TDFLs have been widely demonstrated utilising several material-based SAs, for example, semiconductor saturable absorber mirror [53, 61, 190], graphene [28, 47], and carbon nanotubes [55]. In the previous chapter, I have reported the demonstration of an all-fiberised ML-TDFL generating SWIR pulses with energy exceeding 10 nJ. The ML-cavity was enabled by a SESAM, which provides an efficient saturable absorption mechanism and has high damage threshold. However, the SESAM has limited reflection bandwidth [79], i.e., covering from 1850-2000 nm. Therefore, the development of the SESAM-based ML-TDFL at wavelengths below this window is challenging. Moreover, there were no commercially available SESAMs that could support ML operation at shorter wavelengths, i.e., 1800 nm, at the time of the experiment. Having contacted the supplier to find a possible solution, it became apparent that it might not be straightforward to solve this issue in a short-time period. Alternatively, I investigated another material-based SA, i.e.,

CNTs, which could be specifically designed for the desired wavelengths and fabricated at the CGC.

CNT-based ML cavities have been demonstrated in several wavelength ranges, e.g., 1-μm [154], 1.5-μm [78, 153], and 2-μm [54] thanks to their broad spectral resonances. Moreover, the spectral response of CNTs can be controlled by varying their physical property [78]. In the context of the ML-TDFL, CNT-SAs have demonstrated their capability for controlling saturable absorption properties [32] or providing broad spectral bandwidth [188]. With a proper design, the CNT has a high potential to support ML operation at SWIR wavelengths too, i.e., toward 1800 nm.

4.2 Carbon nanotubes saturable absorbers characterisations

The CNT-SAs, discussed in this chapter, were fabricated by a research group at the CGC, University of Cambridge. The information of CNT-SA fabrication can be found in ref [196]. The samples were deposited onto polymer films that can be cut into small pieces and attached on a fibre-end facet. Under the research collaboration, CGC provided these samples with six different labels: ADSWNT, DWNT, RN220, ADCNT, Hipco-spray, and HEC-DWNT. Once these samples have arrived our group, I characterised their relevant optical properties to understand their functionality.

4.2.1 Wavelength dependent transmission

Wavelength-dependent transmission was measured to identify supporting wavelengths of CNT samples. Figure 4.1(a) presents a schematic of the experimental setup to measure the wavelength-dependent transmission. A low-power, continuous wave (CW) signal with a wavelength ranging from 0.45-5.5 μm was provided by a broadband light source (SLS202L, Thorlabs). This signal was utilised as an incident signal in this experiment, which was delivered through multimode fibres (MMFs) connected by a fibre uniter. The CNT-SA samples were cut into small pieces and can be attached to fibre-end facets, as shown in Figure 4.1(b). The sample was attached between two MMF facets that are connected at a uniter. Therefore, wavelength-dependent transmission can be measured by an optical spectrum analyser (OSA; AQ6375, Yokogawa) with wavelengths covering from 1200-2400 nm.

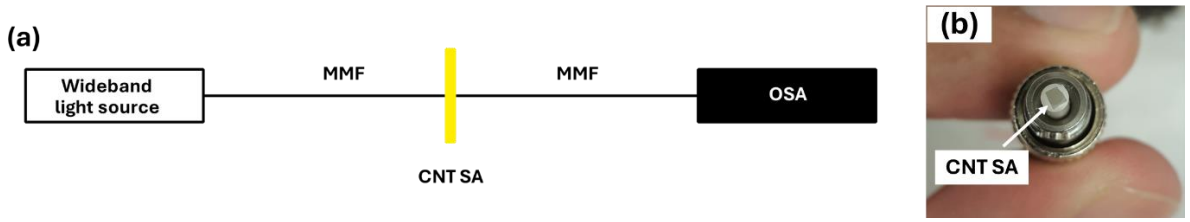

Figure 4.1 (a) Schematic of wavelength-dependent transmission measurement setup, (b) Picture of a CNT-SA on a fibre-end facet. MMF: multi-mode fibre; CNT SA: carbon nanotubes saturable absorber; OSA: optical spectrum analyser.

Figure 4.2 presents the wavelength-dependent transmission of each CNT sample, revealing different spectral responses. This behaviour is an important factor to control the operating wavelength in the ML cavity. For example, the DWNT (red line) demonstrates higher transmission at shorter wavelengths <1830 nm, compared to its longer wavelength region. Consequently, this sample has a high potential to support ML operation at short wavelengths. However, the intensity-dependent transmission must be characterised to assess their functioning as an SA. This experiment is explained in the following section.

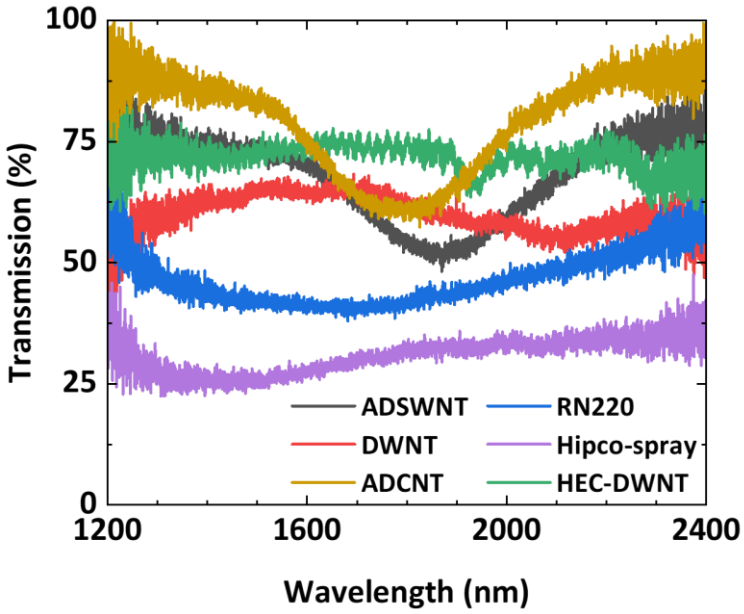

Figure 4.2 Wavelength-dependent transmission of the carbon nanotube saturable absorbers.

4.2.2 Intensity dependent transmission

Intensity-dependent transmission of the CNT samples was measured to characterise their modulation depths and saturation fluences. This information is essential for estimating the SA performance of the CNTs. A schematic of this experiment is presented in Figure 4.3. A home-built ML-TDFL was used as a seed laser to provide short pulses at a central wavelength of 1870 nm. The seed signal was amplified through a thulium-doped fibre amplifier (TDFA) to achieve sufficient

output powers for the characterisation. A 1560/1960-nm wavelength-division-multiplexer (WDM) was connected at the TDFA output to eliminate any residual pump and avoid high-power CW signal incidents on the samples. An in-line attenuator was employed to adjust the power of the signal. Subsequently, the signal was coupled through a 0.75/0.25 fiberised beam splitter, where 25% of the signal was to be measured as a reference power. The second fibre tail (with 75% of the power) was connected to a uniter. The CNT sample can be attached between two fibre facets at this uniter. The transmitted signal can be measured with the optical power meters (SC148C, Thorlabs). It is worth noting that the pulse duration has measured to be ~600 fs at the CNT position.

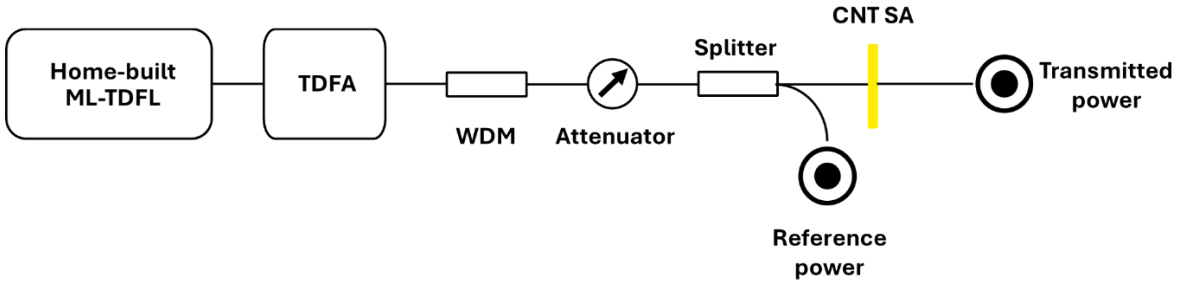

Figure 4.3 Schematic of the intensity-dependent transmission setup. ML-TDFL: mode-locked thulium-doped fibre laser; TDFA: thulium-doped fibre amplifier; WDM: wavelength-division-multiplexer; CNT SA: carbon nanotubes saturable absorber.

The intensity-dependent transmission of the CNT samples is presented in Figure 4.4 (symbols). The results show that most CNT samples provide saturable absorption characteristics, where the transmission increases at higher incident pulse fluence. From the results, different saturable absorption can be observed corresponding to the sample types. However, the sample labelled HEC-DWNT does not provide saturable absorption behaviour.

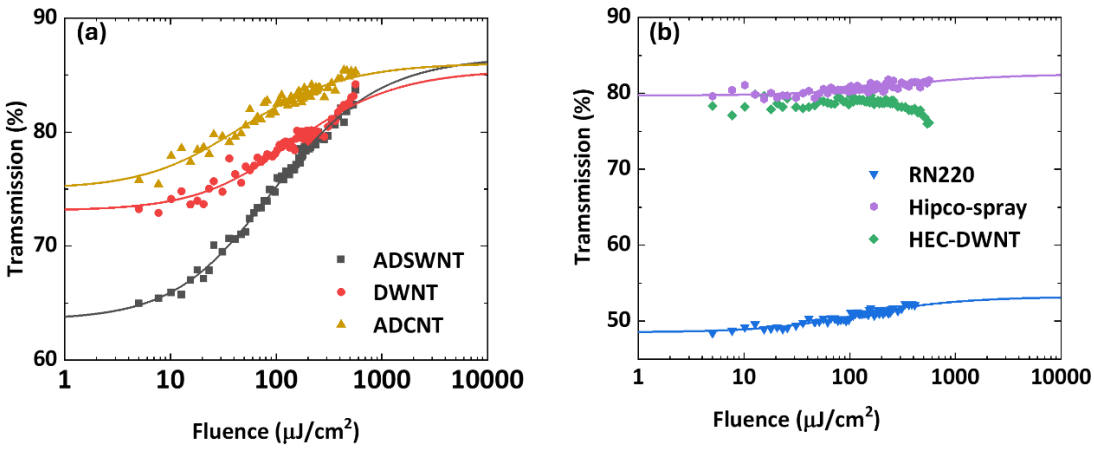

Figure 4.4 (symbols) Measured intensity-dependent transmission of carbon nanotubes saturable absorbers with labelled (a) ADSWNT, DWNT, and ADCNT, and (b) RN220, HEC-DWNT, and Hipco-spray. (Solid line) Theoretical fit.

The modulation depth and saturation fluence for each sample were acquired by fitting the experimental result to a fast saturable absorption model, equation (2.31) (see also Section 2.3.2). Solid lines in Figure 4.4 represent the theoretical fit results of each sample. The modulation depths and saturation fluences of CNT samples are presented in Table 4.1. As expected, the respective CNT samples have different modulation depths and saturation fluences, which vary depending on their characteristics. It is worth mentioning that the response of the HEC-DWNT does not fit the model as it does not show saturable absorption behaviour. For the CNT-SAs in this measurement, ADSWNT provides the highest modulation depth at 23.1%, while the Hipco-spray shows the lowest modulation depth at 2.8%. It is worth nothing that the DWNT, which has high potential to support short operating wavelengths (as mentioned in the previous experiment), provides a modulation depth of 12.3%, with a saturation fluence of 88.9 μJ/cm^2, indicating a good potential to effectively provide saturable absorption in a cavity.

Table 4.1 Modulation depth and saturation fluence from fitting the intensity-dependent transmission.

Sample	Modulation depth (%)	Saturation fluence (μJ/cm^2)
Hipco-spray	2.8	169.7
RN220	4.7	74.4
ADCNT	11.0	28.6
DWNT	12.3	88.9
ADSWNT	23.1	56.1

4.3 CNT-based thulium mode-locked fibre laser

In this section, I report the demonstration of a ML-TDFL enabled by the CNT-SA (DWNT) that has been characterised in the previous section. This laser was aimed to be utilised as a seed in biomedical imaging MOFA. Therefore, the cavity was expected to provide a stable ML operation at a wavelength of ~1850 nm with low ML threshold (<200 mW) to achieve a compact system.

A schematic of the CNT-based ML-TDFL is illustrated in Figure 4.5. A 1563-nm CW laser signal with a maximum power of 2 W was provided by the EDFA (explained in Section 3.2.1). The pump signal was coupled into the cavity through a WDM. A 0.5-m length of commercially available TDF (TmDF200, OFS; $\beta_2 = -0.02\ ps^2/m$ at 1.9 μm) was employed to enable the SWIR wavelengths. An output coupler was employed to extract 25% of the oscillating power as a laser output. Unidirectional oscillation was ensured by an isolator (ISO), connected to the 75% residual section of the OC splitter. In-line polarisation controllers (PCs) were employed to tune the polarisation, initiating the ML operation. The DWNT was inserted between two angled fibre patch chords,

functioning as the SA. As mentioned earlier, this DWNT had a good potential to support ML operation at short wavelengths, providing a modulation depth of 12.3%. A 4.5-m length of dispersion compensation fibre (UHNA4, Coherent) was used to manage the net cavity dispersion. Other sections are connected by single-mode fibres (SMFs; SMF-28, Corning). The total cavity length was 10 m with a net dispersion of 0.25 ps^2.

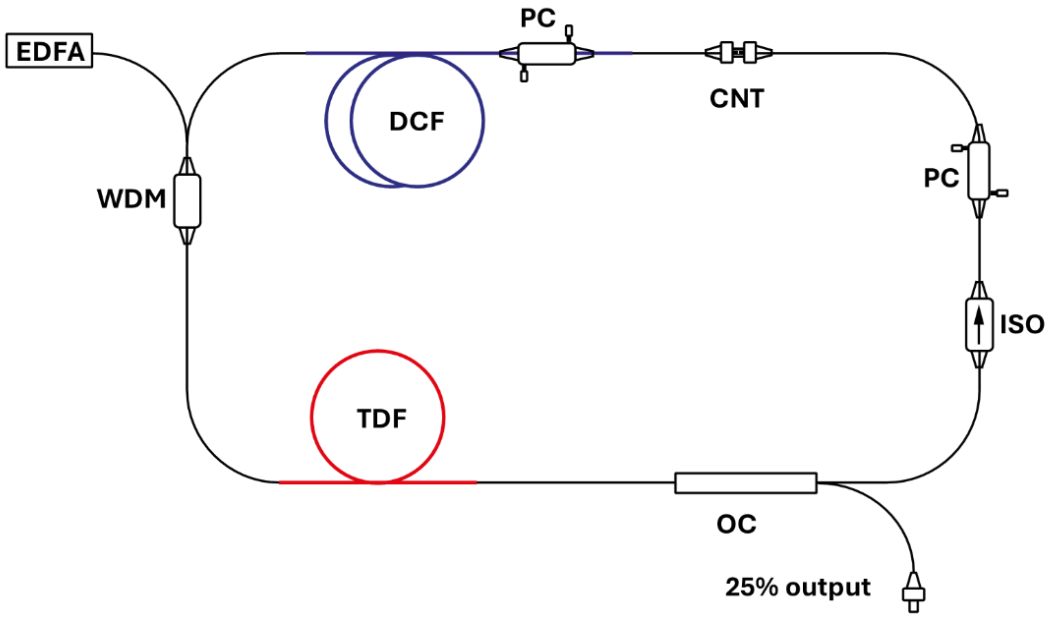

Figure 4.5 Schematic of the mode-locked thulium-doped fibre laser. EDFA: erbium-doped master oscillator fibre amplifier; WDM: wavelength-division-multiplexer; TDF: thulium-doped fibre; OC: output coupler; ISO: isolator; PC: polarisation controller; DCF: dispersion compensation fibre; CNT: carbon nanotubes saturable absorber.

Stable ML operation was achieved at a pump power threshold of 190 mW with the appropriate PC position. Therefore, the ML threshold was significantly reduced in this cavity compared to the previous SESAM-based cavity. However, the cavity had a very low (~1 mW) output power. The output signal has a sharp-edge, flat-top spectrum as the dissipative soliton. Figure 4.6(a) presents the output spectrum at a central wavelength of 1847 nm with a 10-dB bandwidth of 30 nm. The output pulse has a repetition rate of 20.37 MHz, corresponding to the estimated value from the total cavity length. Due to the low output power, a temporal pulse width could not be directly measured. Therefore, the output pulse was amplified by a home-built thulium-doped fibre amplifier (TDFA) to achieve higher output powers. It is worth mentioning that the output spectrum remained unchanged after the amplifier. Hence, the nonlinearity in the TDFA was negligible. Figure 4.6(b) presents an ACF trace of an uncompressed pulse, equivalent to an assumed Gaussian-shape pulse duration of 5.1 ps.

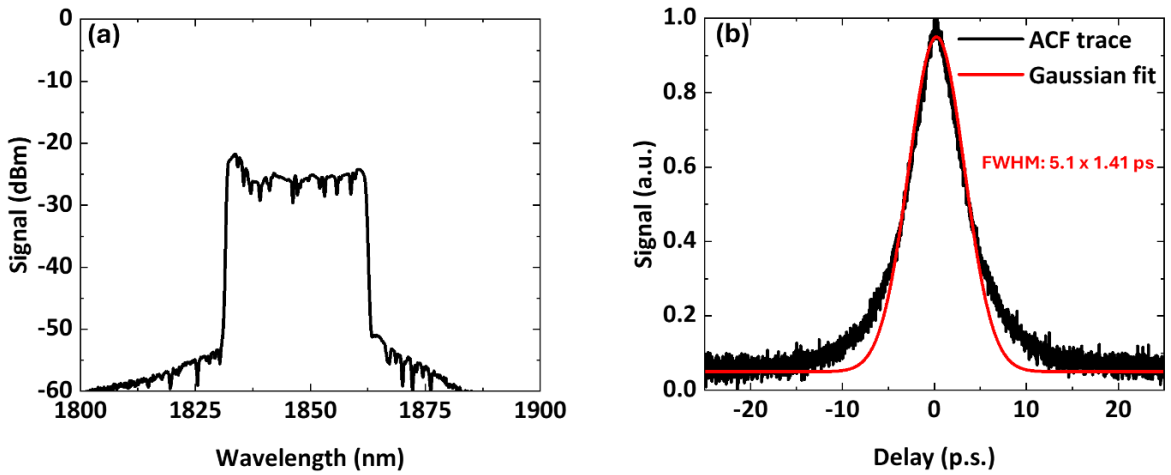

Figure 4.6 (a) output spectrum of the mode-locked thulium-doped fibre laser, and (b) the uncompressed pulse duration after amplification.

I employed this cavity in a compact, protected space to minimise the effects of physical perturbations. This laser exhibits a stable ML operation over an extended period before requiring the PC adjustment, which was suitable for integrating into the imaging laser system. This laser was handed over to Mr.Ibrahim Abughazaleh, another PhD student in the research group, and the cavity was utilised as a seed cavity in the imaging laser system. An idealised diagram of the imaging laser system is presented in Figure 4.7(a). The output pulse was amplified through a CPA system. The repetition rate of output pulses was controlled by an acousto-optics modulator (AOM) (MHP250-6.6ADM-A1, Gooch & Housego). This laser provides the maximum output power of 400 mW with the lowest repetition rate of 2 MHz. The output pulse duration could be compressed using a grating-pair compressor. Figure 4.7(b) presents an ACF trace of the compressed pulse duration, equivalent to a pulse duration of 381 fs, based on the Gaussian-shape assumption. It is worth noting that the pedestal in the compressed ACF trace might be caused by nonlinearity in the amplifiers that cannot be completely resolved by the grating-pair compressor. This laser system was delivered to our project partner at the IfLS and has been used as a pump source in biomedical imaging experiments.

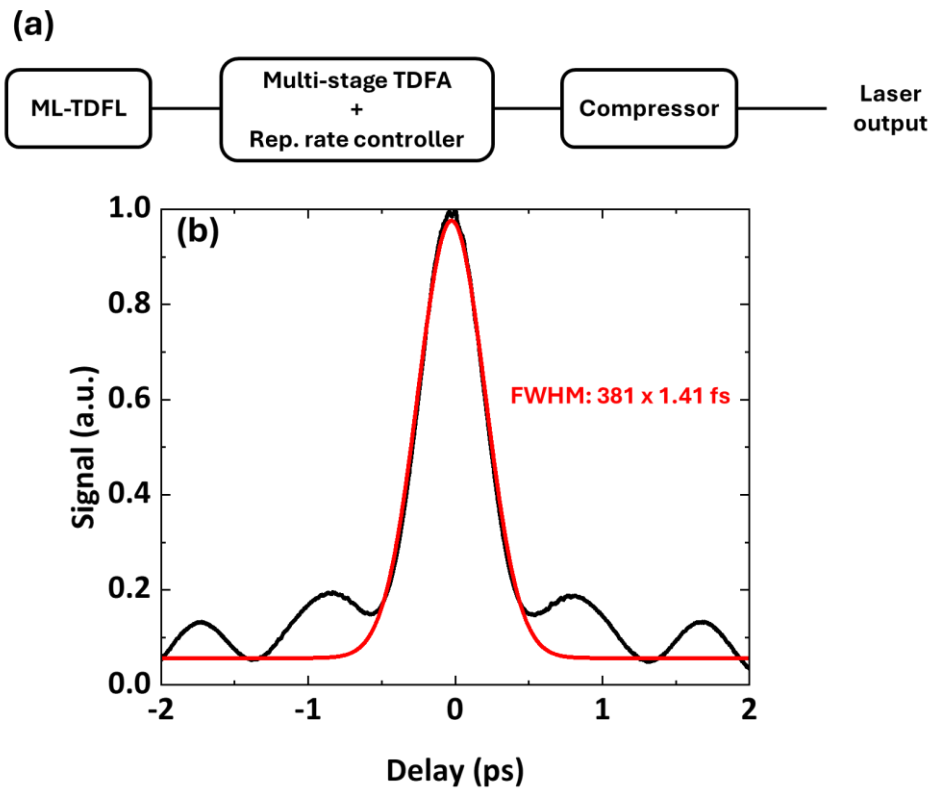

Figure 4.7 (a) Idealised schematic of the laser system, (b) compressed pulse duration of the output pulse. This part of work was carried out by Mr.Ibrahim Abughazaleh (another PhD student in the research group).

4.4 Summary

In this chapter, I detailed the experiments to characterise the CNT-SAs supplied by the research collaboration with the CGC. The CNT samples have demonstrated their ability to support ML operation at short wavelengths, i.e., toward 1800 nm with various modulation depths, depending on the sample types. These CNTs will be further used to develop ML-TDFL, explained in the following chapters of this thesis.

Additionally, I also demonstrated an all-fiberised ML-TDFL enabled by the CNT-SA. A cavity was constructed to produce stable dissipative-soliton ML operation at a central wavelength of 1847 nm. The laser was employed as a seed in the imaging laser system. The work was done by Mr.Ibrahim Abughazaleh, another PhD student in the research group supporting the generation of an output power of 400 mW at a repetition rate of 2 MHz. The pulse could be compressed to a pulse duration of 381 fs. This laser has been delivered to be utilised as the optical source in biomedical imaging experiments at the IfLS, University of Southampton.

Chapter 5 All-PM mode-locked thulium-doped fibre laser enabled by CNT saturable absorber

In this chapter, I present, to the best of my knowledge, the first demonstration of a nJ-pulse-energy, all-polarisation-maintaining (all-PM) dissipative-soliton mode-locked thulium-doped fibre laser, enabled by CNT-SAs. This chapter also explains the fiberised Lyot filter (LF), which is a required component to facilitate dissipative-soliton operation. A splicing technique to optimise the connection of PM dispersion compensation fibre (DCF) with passive PM single-mode fibres (PM-SMFs) is also explained as an important element to achieve a net normal dispersion cavity in an all-PM configuration. The all-PM dissipative-soliton cavity, developed in this chapter, provides reliable output pulse properties that have great potential to be employed as a laser source for multiphoton biomedical imaging applications. Self-starting ML operation was achieved with a central wavelength of 1876 nm and a pulse energy of 1.1 nJ. The output pulse has a (compressed) pulse duration of 391 fs.

This chapter is comprised of four sections. The first section discusses the background of all-PM ML-TDFL. While the second section explains all-PM conventional-soliton ML-TDFLs using CNT-SAs. Furthermore, an experiment to explore a fiberised LF is also discussed in this section. The third section explains the development of all-PM dissipative-soliton ML-TDFL. This section also includes the characterisation of PM-DCF and a technique to optimise its splicing with PM-SMF. The summary of this chapter is given in the final section. It is worth noting that some contents in this chapter have been published in [197], by Elsevier Ltd. under a Creative Common license.

5.1 Background

ML-TDFLs can generate ultrafast SWIR pulses corresponding to a broad emission bandwidth of the TDF [18]. However, ML-TDFLs, constructed with non-PM fibres, are sensitive to environmental or physical perturbations, resulting in the variation of output pulse properties, i.e., spectral bandwidth, pulse duration, or energy [198]. Typically, non-PM cavities require polarisation controllers (PCs) to initiate or maintain ML operation, even in laboratory environments [21]. In contrast, ML lasers constructed using PM fibres, with high birefringence, demonstrate an enhanced robustness and stability [86, 87]. Consequently, ML-TDFL based on PM fibres have good environmental insensitivity and can maintain long-term stable operation [85]. Therefore, all-PM ML-TDFLs are preferred as reliable sources in real-life applications.

In the context of all-PM configurations, ML-TDFLs have been demonstrated with different SAs, including optical loop mirrors [199], graphene [28], carbon nanotubes [32], and semiconductor saturable absorber mirror [200]. However, standard PM-SMFs exhibit anomalous dispersion in the

2-μm region, therefore, these cavities were constructed using all-anomalous dispersion fibres. Consequently, these cavities support conventional solitons, and are limited to pJ-level pulse energies [65]. To improve the output pulse properties, normal-dispersion DCFs are required for managing the net-cavity dispersion, which enhances accumulated nonlinear phase shift tolerance [21]. However, dispersion management of all-PM ML-TDFL is challenging due to the limited availability of PM-DCFs [42, 47]. For instance, a dispersion-managed PM ML-TDFL has been reported at a central wavelength of 1945 nm with a pulse energy of 220 pJ [47]. In that cavity, a 1.5-m length of in-house-fabricated PM-DCF was employed, and ML operation was enabled by a 35-layer graphene/poly(methyl methacrylate)-based SA. However, the output properties of these pulses might not be suitable for biomedical imaging applications due to water absorption of wavelengths beyond 1900 nm. Another dispersion-managed ML-TDFL has been demonstrated using a 0.7-m length of commercial PM-DCF (PM2000D) and an arc-discharge, single-wall nanotube (SWNT)-based SA [42]. The ML operation was centred at a wavelength of 1787 nm, however, with very low pulse energy (~70 pJ). Despite utilising PM-DCFs, these cavities still have anomalous dispersion [42, 47]. Therefore, the cavity operates in a stretched-pulse regime with low pulse energies in the pJ-level. In comparison, dissipative-soliton cavities with net-normal cavity dispersions offer a larger tolerance to nonlinear phase shifts than other soliton types [56]. Consequently, the cavity can generate high pulse energies at the nJ-level [59]. However, dissipative solitons require a balance of both conservative effects (dispersion and nonlinearity) [58] and dissipative effects (spectral gain and loss) [59]. Therefore, it requires careful design of dispersion maps and spectral filtering [21]. An all-PM dissipative-soliton ML-TDFL has demonstrated utilising a 3-m length of in-house fabricated PM-TDF, serving as both gain fibre and DCF [92]. The cavity achieves a stable ML operation, however, at a central wavelength of 1995 nm and an output pulse energy of ~44 pJ due to high splicing loss between PM-TDF and standard PM-SMF (~3 dB). Therefore, the development of nJ-pulse-energy dissipative soliton in all-PM ML-TDFL can be challenging.

5.2 CNT-based all-PM conventional-soliton thulium fibre laser

In this section, I explain relevant experiments to develop a conventional-soliton ML-TDFL, using PM fibres, enabled by a CNT-SA. Additionally, this section also presents an experiment to assess the functionalities of CNT samples (explained in Section 4.2) as SAs. Moreover, this section includes experiments to observe fiberised LFs, which are crucial for the development of the dissipative soliton.

5.2.1 Conventional-soliton cavity design

A schematic of a conventional-soliton, all-fiberised PM ML-TDFL enabled by CNT-SA is presented in Figure 5.1. A 1563-nm continuous-wave (CW) seeded EDFA was employed as a pump with a maximum power of 2 W. The pump was coupled into the cavity through a 1560/1840 nm PM-wavelength-division-multiplexer (PM-WDM). A 7-cm length of 5-μm-core PM-TDF (5μm-PM-TDF; PM-TSF-5/125, Coherent) was utilised to enable SWIR operation because this fibre has a high pump absorption of 340 dB/m at 1560 nm. A PM-output coupler (PM-OC) was spliced into the cavity to extract 90% of the oscillating energy as a laser output. A unidirectional oscillation was ensured by a PM-isolator (PM-ISO). The CNT-SA (DWNT) was attached between two angled fibre patch chords, connected with a uniter, at the output pigtail of the PM-ISO. All PM-SMFs used in this cavity were PM-1550 fibres (PM1550-XP, Coherent; $\beta_2 = -0.059\, ps^2/m$ at 1.9 μm) [191]. This cavity has a total length of 4.3 m with an estimated net cavity dispersion of -0.25 ps^2.

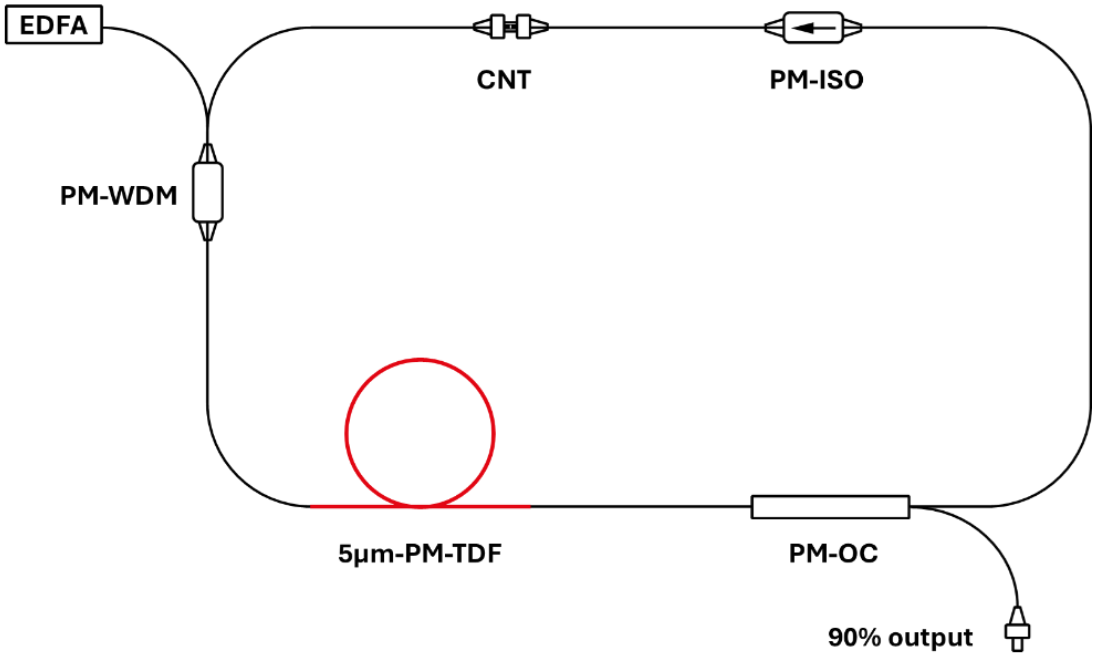

Figure 5.1 Schematic of an all-polarisation maintaining (PM), conventional-soliton thulium-fibre laser. EDFA: erbium-doped master oscillator fibre amplifier; PM-WDM: PM-wavelength-division-multiplexer; TDF: thulium-doped fibre; PM-OC: PM-output coupler; and CNT: carbon nanotubes.

Stable ML operation was generated once the pump power reached the mode-locking threshold, without requiring any polarisation controller (PC). At a pump power threshold of 300 mW, a self-start, 'turnkey' ML operation exhibits an output spectrum with Kelly sidebands, as presented in Figure 5.2 (red line). The spectrum has a central wavelength of 1892 nm with a 3-dB bandwidth of 4.6 nm. The output signal exhibits a repetition rate of 47.48 MHz, which matches well with the estimated value from a calculation based on the total cavity length. The pulse duration was measured to be ~800 fs, based on the $Sech^2$-pulse assumption. It is important to note that the

cavity robustness has significantly improved compared to the previous non-PM cavities. Thus, ML operation is sustained even in the presence of physical perturbations.

To mitigate re-absorption and enhance the cavity for short-wavelength operation, the gain fibre length was shortened to 4.5 cm [112]. Consequently, the central wavelength was shifted to 1868 nm as shown in Figure 5.2 (black line). However, the ML threshold was increased to 370 mW.

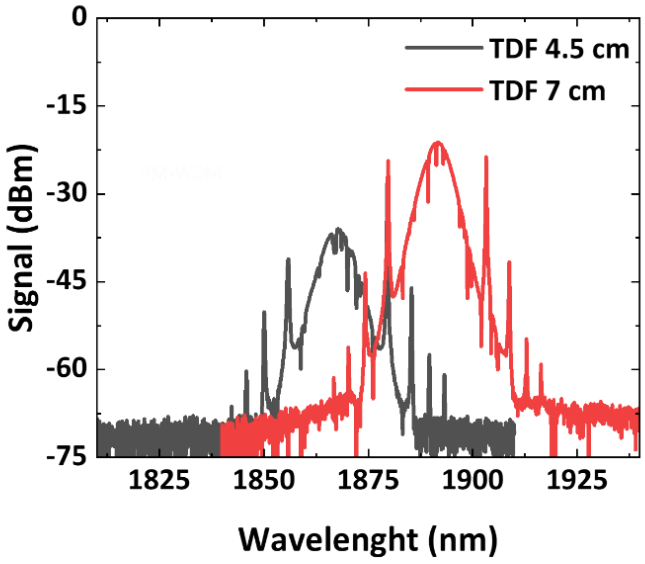

Figure 5.2 Output spectrum of the all-PM conventional-soliton thulium mode-locked fibre laser with (red curve) 7-cm TDF, and (black curve) 4.5-cm TDF.

Various CNT samples, characterised in Section 4.2, were incorporated into this cavity to assess their functioning as SAs, while other parts were kept unchanged. Therefore, different output pulse characteristics were influenced by the properties of the CNT samples. Figure 5.3 (a)-(d) presents the ML spectra with various CNT-SAs. In this experiment, there are four CNT samples that can generate stable ML operation.

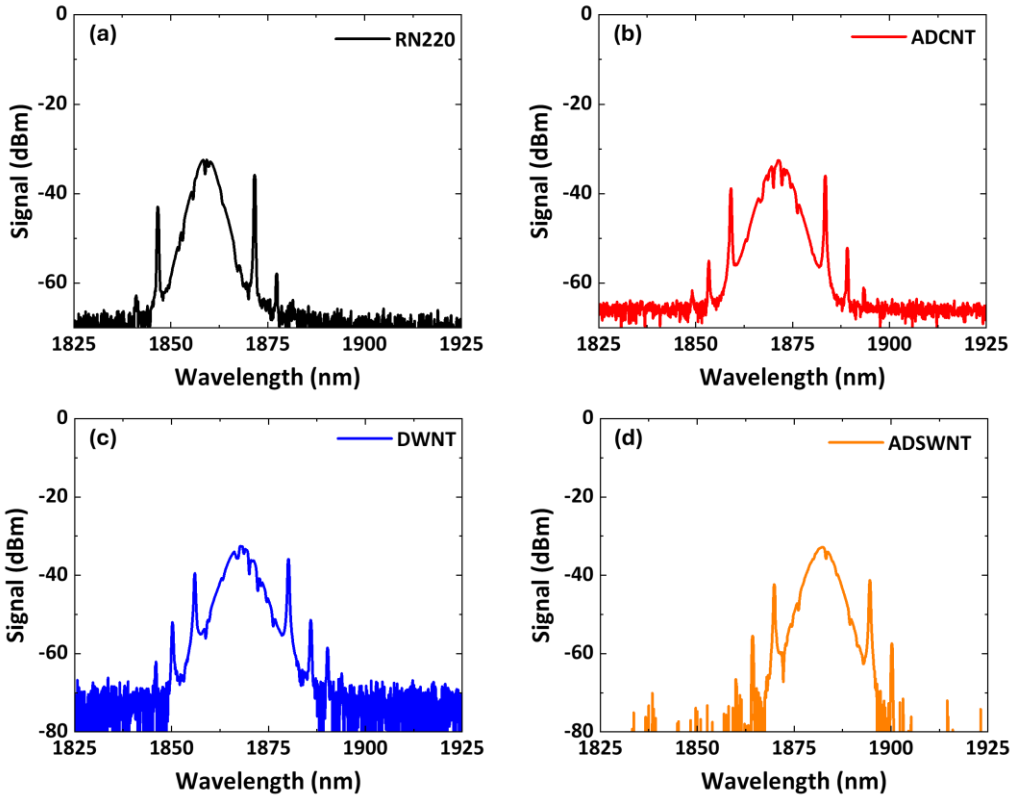

Figure 5.3 Mode-locked spectrum of the conventional soliton using (a) RN220, (b) ADCNT, (c) DWNT, and (d) ADSWNT as a saturable absorber.

The central wavelengths and ML thresholds vary across different CNT-SA types, indicating the influence of their wavelength-dependent transmission. Table 5.1 presents an overview of the output spectral properties and the ML threshold for different CNT-SAs. The results confirm that these CNT-SAs have good potential to support ML operation at wavelengths ranging from 1800-1900 nm, supporting the objective of this thesis. These CNT-SAs have therefore been used in other ML-TDFLs reported in this thesis.

Table 5.1 Mode-locked output spectrum properties and its threshold with different carbon-nanotubes saturable absorbers.

Sample	Central wavelength (nm)	Spectral bandwidth at 3 dB (nm)	Threshold (mW)
RN220	1859	4.7	540
ADCNT	1870	4.1	320
DWNT	1868	4.7	350
ADSWNT	1882	4.5	330

5.2.2 Fiberised Lyot filter experiment

The filtering effect is an important component of the dissipative-soliton ML operation. It serves not only to control the output pulse at desired central wavelengths but also to balance the

dissipative effect of spectral gain-loss in the cavity [59]. To facilitate demonstrating an all-fiberised PM ML-TDFLs, a fiberised LF has been developed utilising PM-SMFs. The theoretical details of the LF can be found in Section 2.4. A fiberised LF was implemented by using an offset-angle splice method, in which the rotation angle offset between the slow axes of two PM fibres was controlled at an appropriate value during the splicing process. Figure 5.4 presents an experimental setup to demonstrate the fiberised LF effect, constructed on a fibre connection between PM-OC and PM-ISO. A CW pump signal at 1563 nm, provided by a commercial EDFA, was coupled through a PM-WDM into a PM-TDF to generate a broad ASE spectrum. This ASE signal was employed as an input for the experiment. The ASE was coupled through a PM-OC with a fast-axis blocked function, ensuring the transmitted ASE polarisation aligned with the slow-axis. A PM-SMF, functioning as a birefringence material, was spliced to the PM-OC tail at a 45-degree offset angle between their slow axes. Accordingly, the ASE signal was decomposed into two different polarisation components and experienced different phase delays related to the refractive index in each optical axis. Another PM-SMF fibre with an identical length to the input tail of the PM-ISO was employed with a 45-degree offset splice to the LF and a 90-degree offset splice to the PM-ISO input tail. This configuration effectively compensates for the effect of polarisation-dependent dispersion and prevents any temporal walk-off of the oscillating pulse [165, 166]. Due to the wavelength-dependent behaviour of the phase delays, the periodic filtering effect can be observed at the output of the PM-ISO with a fast-axis blocked function.

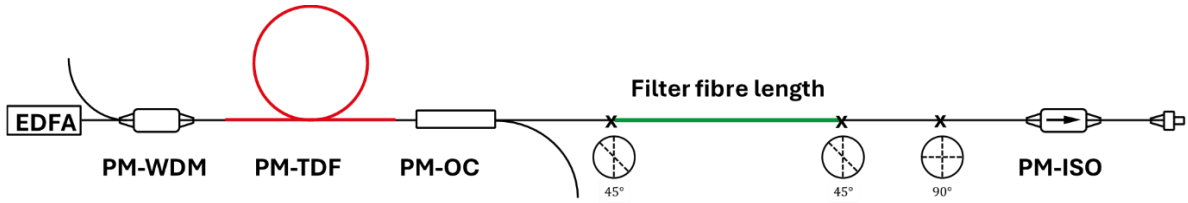

Figure 5.4 Experimental setup to observe fiberised Lyot filter effect. EDFA: erbium-doped master oscillator fibre amplifier; PM-WDM: PM-wavelength-division-multiplexer; PM-TDF: PM-thulium-doped fibre; PM-OC: PM-output coupler; and PM-ISO: PM-isolator.

Figure 5.5 (a)-(e) presents a transmitted ASE spectrum of the LF (red curve), compared with the input ASE (black curve). The periodic behaviour of transmitted ASE is more rapidly oscillating with longer LF fibre lengths, resulting in narrower free-spectral range (FSR) and full width at half-maximum (FWHM) values. Therefore, the LF bandwidth can be controlled by adjusting the fibre length.

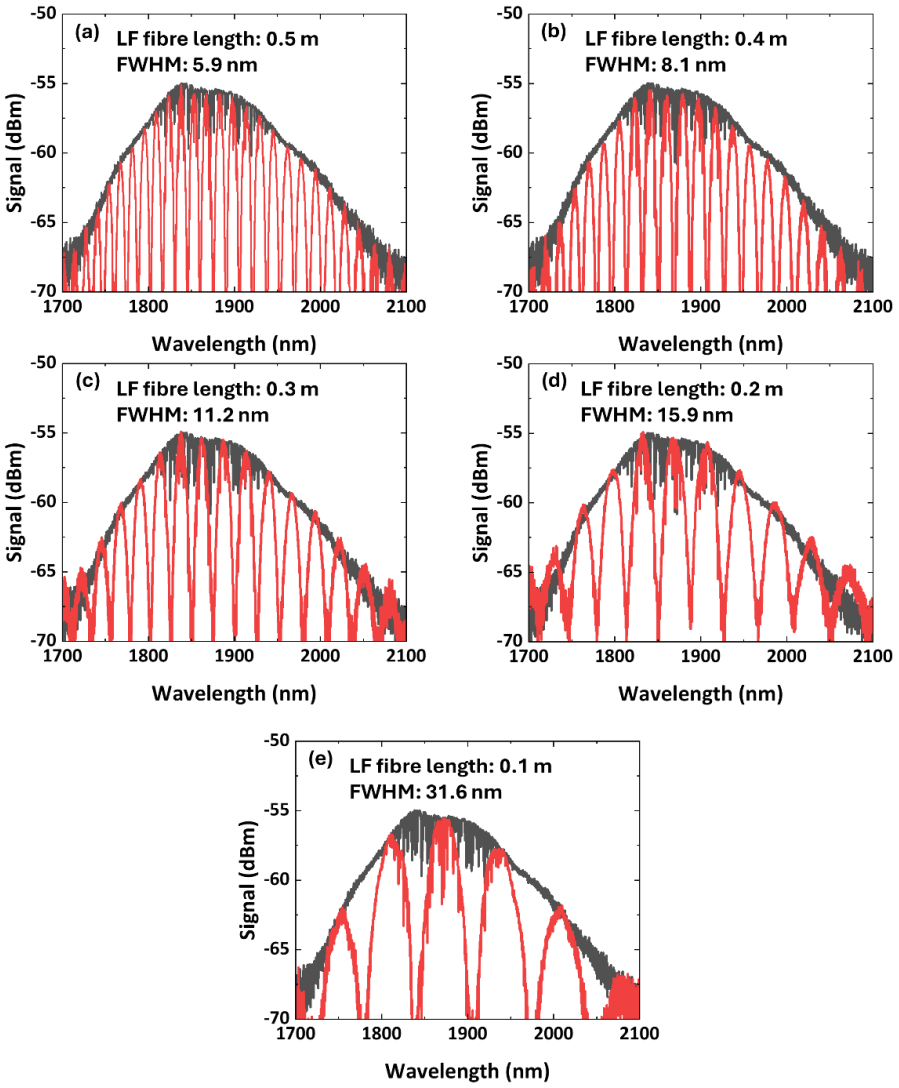

Figure 5.5 (red curve) Measured transmitted spectra of the Lyot filter (LF) fibre length of (a) 0.5 m, (b) 0.4 m, (c) 0.3 m, (d) 0.2 m, and (e) 0.1 m. (black curve) input amplified spontaneous emission. FWHM: full width at half-maximum.

The LFs were integrated in the all-PM conventional-soliton ML-TDFL, as shown in Figure 5.6. The ML spectra with various LFs are presented in Figure 5.7 (a)-(f), showing the influence of the LF on the ML spectrum. The LF reduces the effect of Kelly sidebands, especially when its fibre length is longer than 0.2 m, where the sidebands are completely eliminated. Table 5.2 gives an overview of the output pulse properties of ML operation with various LF fibre lengths. The central wavelength of ML operation varies according to the maxima of the LF transmission. Furthermore, the 3-dB bandwidth is reduced with increasing LF fibre length, corresponding to a narrower filtering effect.

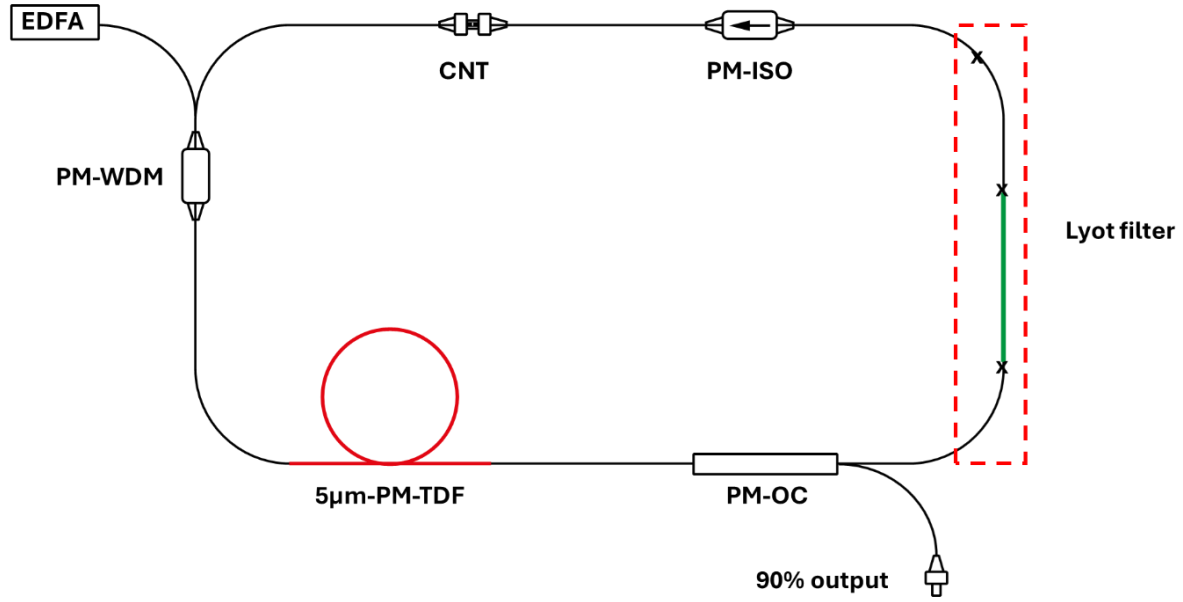

Figure 5.6 Schematic of an all-polarisation maintaining (PM), conventional-soliton thulium-fibre laser with Lyot filter. EDFA: erbium-doped master oscillator fibre amplifier; PM-WDM: PM-wavelength-division-multiplexer; TDF: thulium-doped fibre; PM-OC: PM-output coupler; and CNT: carbon nanotubes.

Table 5.2 Mode-locked output signal properties of all-polarisation maintaining cavity with different filter fibre lengths.

Fibre length (m)	Central wavelength (nm)	Spectral bandwidth at 3 dB (nm)	Threshold (mW)
0.0	1882	4.5	330
0.1	1873	4.5	345
0.2	1868	3.7	340
0.3	1887	2.8	335
0.4	1861	2.2	340
0.5	1867	2.2	330

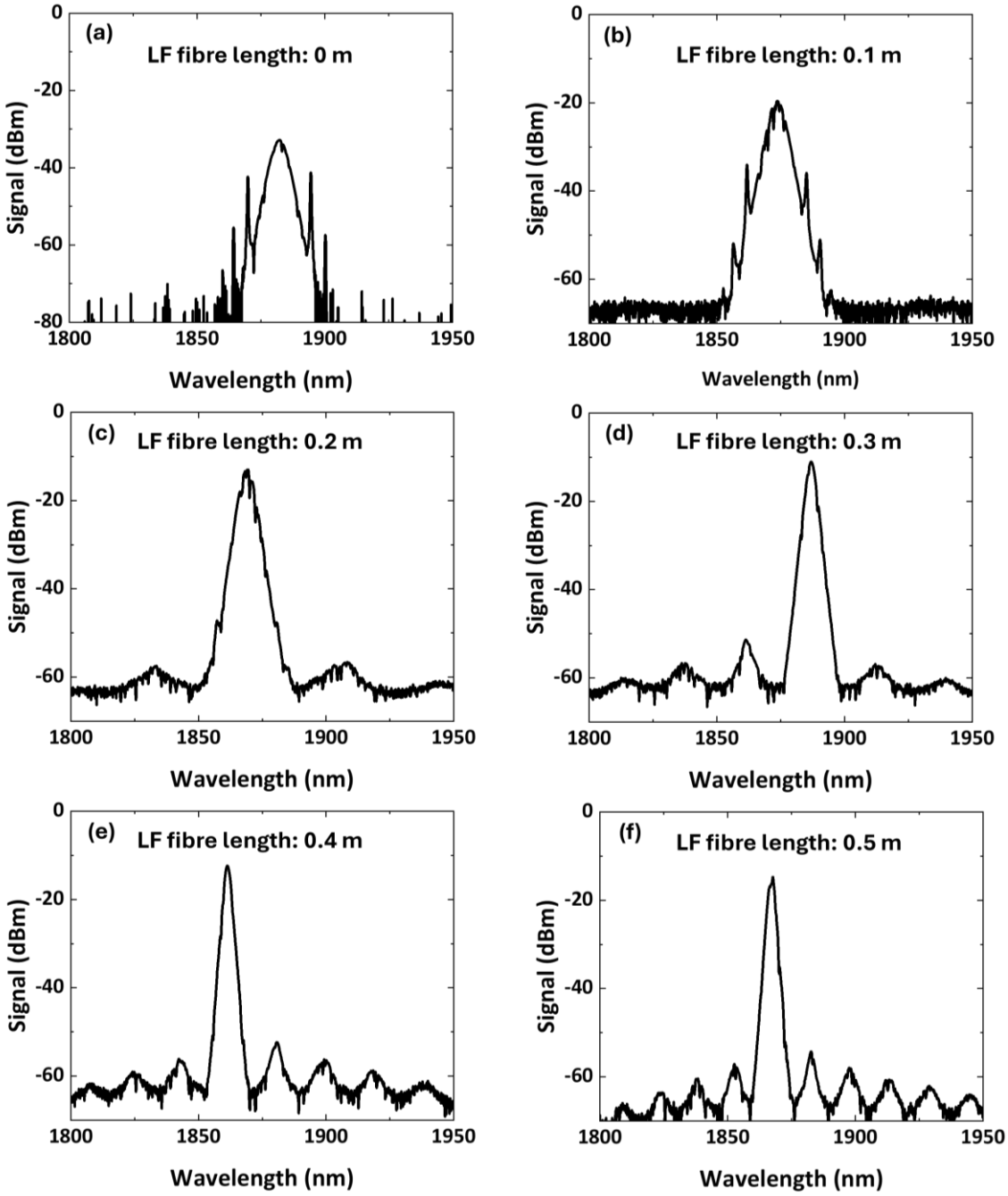

Figure 5.7 Output spectrum from an all-PM of an all-polarisation maintaining (PM), conventional-soliton thulium-fibre laser with Lyot filter length of (a) 0 m, (b) 0.1 m, (c) 0.2 m, (d) 0.3 m,(e) 0.4 m, and (f) 0.5 m.

5.3 CNT-based all-PM dissipative-soliton thulium fibre laser

In this section, I explain experiments to develop an all-PM dissipative-soliton ML-TDFL enabled by a CNT-SA. This laser is expected to provide stable, robust, turnkey ML operation with a pulse energy exceeding 1 nJ. Furthermore, this section also includes an experiment characterising PM-DCF (PM2000D, Coherent) and a splicing technique to optimise its connection with PM-SMF. These studies are important for the development of the all-PM dissipative-soliton ML-TDFL.

5.3.1 Birefringence measurement of PM fibres

In the context of PM fibre, stress-applying areas are introduced in the fibre cladding at opposite directions across the core area, introducing unequal stress along its aligned direction compared to its orthogonal direction [84], therefore inducing birefringence in the fibre [201]. As explained in the previous section, the Lyot filtering effect can be facilitated by the tilted-splice method, in which the FSR can be controlled by varying the fibre length. With a similar setup, the birefringence of PM fibres can be characterised by employing fibres with fixed lengths. Figure 5.8 depicts an experimental setup for birefringence measurement. A 1563-nm CW-seeded EDFA was employed to supply a pump at a fixed power. The pump was coupled through a WDM into an ORC fabricated TDF, enabling a broad ASE spectrum corresponding to the TDF gain wavelengths. An isolator (ISO) was employed to prevent any possible back reflection. To ensure the linear polarisation of the ASE, a PM-OC with a fast-axis blocked function was utilised in the system. Different PM fibres with a length of ~1 m were spliced to the PM-OC oriented with a 45-degree rotation between their slow axes. Another PM-SMF fibre with an identical length to the input tail of the PM-ISO was spliced with a 45-degree offset splice to the 1-m PM fibre and a 90-degree offset splice to the PM-ISO input tail. The fast-axis blocked PM-ISO functions as an output polariser.

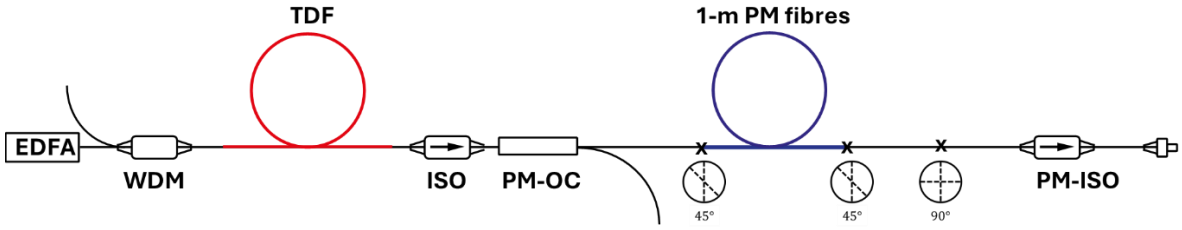

Figure 5.8 Experimental setup to characterise birefringence of polarisation maintaining (PM) fibre. EDFA: erbium-doped master oscillator fibre amplifier; WDM: wavelength-division-multiplexer; TDF: ORC fabricated thulium-doped fibre; PM-OC: PM-output coupler; and PM-ISO: PM-isolator.

The output ASE spectra passing through various PM fibres are presented in Figure 5.9. It is worth mentioning that the additional loss in the measurement of PM2000D might have resulted from the small core size of PM2000D and a free-space gap within the fibre setup, as this fibre was not spliced during the experiment. The results reveal different FSR between maxima of the transmitted ASE in these fibres, being narrower for PM1550 compared to PM2000D, indicating a higher birefringence value. The FSR values were factored in to calculate for an approximated birefringence value derived from equation (2.34) [202, 203]. The estimated birefringence value of PM1550 is ~4.2 x 10^{-4}, which is higher than the value of the PM2000D (~1.5 x 10^{-4}). Consequently, PM2000D can be predicted to have a lower tolerance to physical perturbation, hence requiring special attention to fibre handling and splicing. The detailed information regarding to the splicing method will be explained in the following section.

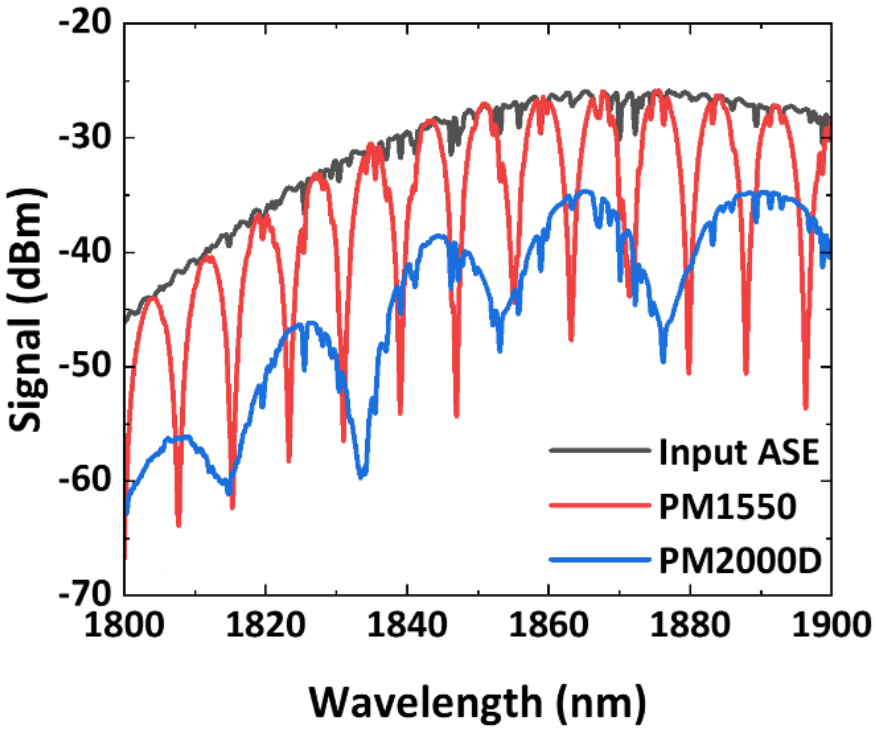

Figure 5.9 Measured amplified spontaneous spectrum (ASE) of (black curve) input ASE, (red curve) PM1550XP, and (blue curve) PM2000D.

5.3.2 Bridge-fibre splice method

To achieve a dissipative-soliton ML operation, it is essential to control the cavity dispersion to be in a net normal dispersion regime [59]. Consequently, a section of the normal-dispersion DCF is required. However, in the 2-μm regime, the options for PM-DCF are limited [42, 47]. During the time of this experiment, I have found the only commercially available fibre supplying a normal dispersion in PM configuration, which is PM2000D (Coherent). This fibre has previously been reported in ML-TDFLs, however, those experiments encounter difficulties when splicing PM2000D with other standard PM-SMFs [42, 199]. Due to a large core size mismatch (2.1-μm vs 8.5-μm), splicing between these two fibres will typically result in an unreliable PM performance and a high splicing loss [204, 205].

Figure 5.10 presents an experimental setup to optimise PM2000D splicing. A fiberised ASE source, with similar configuration to the previous section, was employed to provide a linearly polarised signal, ensuring by the fast-axis-blocked PM-OC. Subsequently, the signal was delivered into various experimental configurations to optimise the splicing of PM2000D. At the output end, a fast-axis-blocked PM-ISO was incorporated to function as a polariser, delivering the signal to the OSA for the spectrum observation.

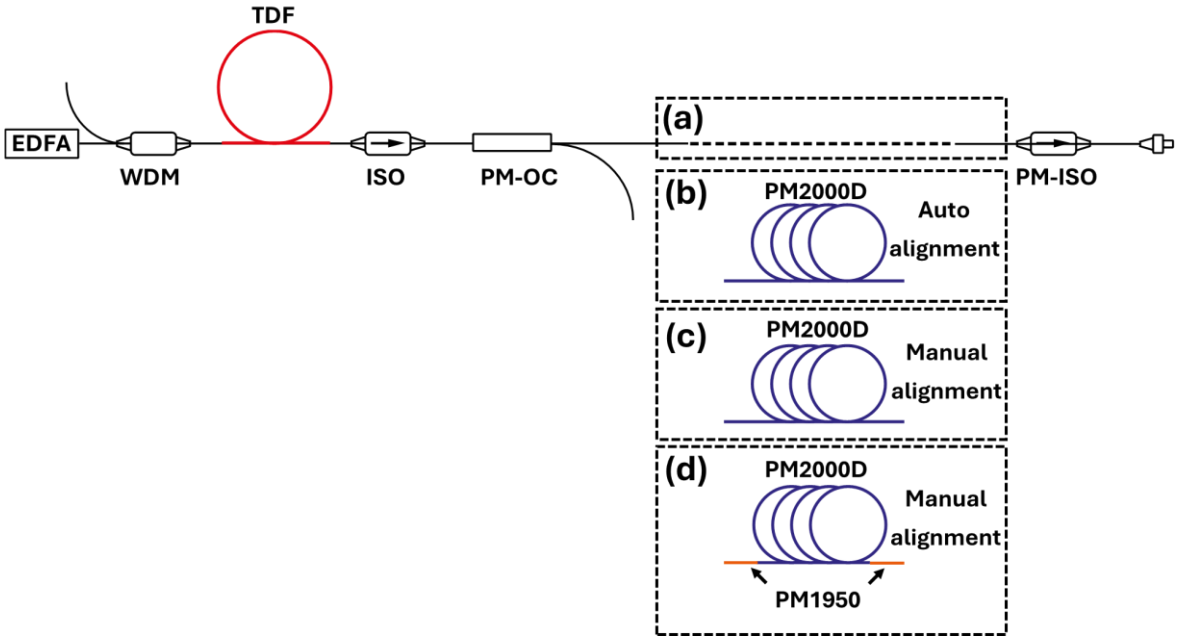

Figure 5.10 Schematic of experimental setup to optimise PM2000D splicing which (a) direct auto-alignment splice between PM-OC and PM-ISO, (b) direct splice of PM2000D with auto-alignment, (c) direct splice of PM2000D with manual alignment, and (d) bridge-splice of PM2000D with manual alignment. EDFA: erbium-doped master oscillator fibre amplifier; WDM: wavelength-division-multiplexer; TDF: ORC fabricated thulium doped fibre; PM-OC: PM-output coupler; and PM-ISO: PM-isolator.

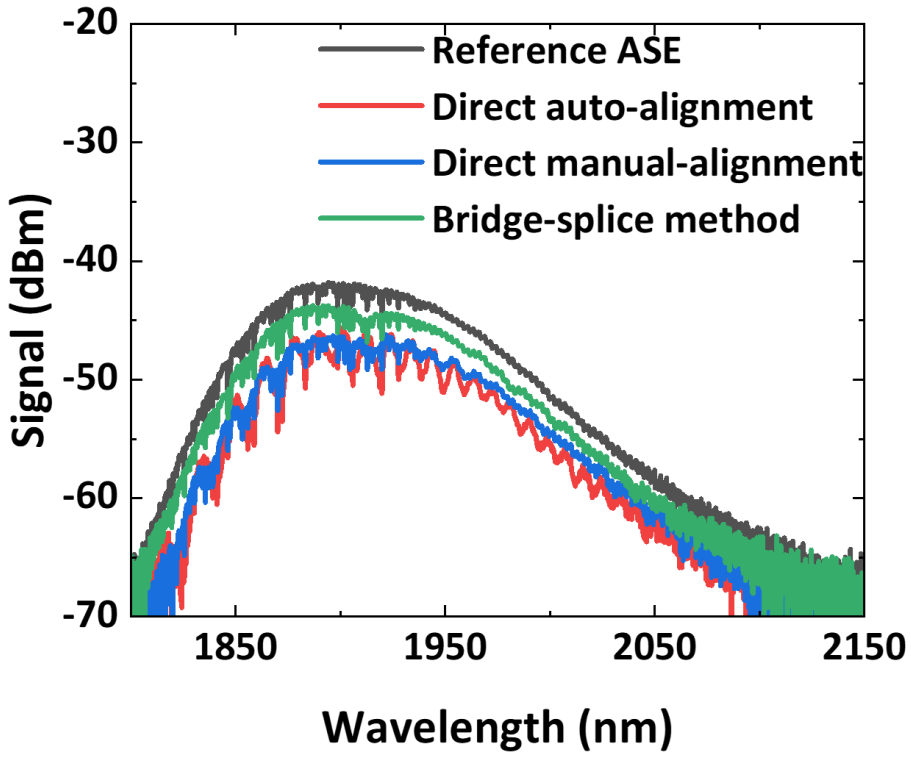

Figure 5.11 Measured output amplified spontaneous emission (ASE) for (black curve) reference ASE, (red curve) direct splice with auto alignment, (blue curve) direct splice with manual alignment, and (green curve) bridge-splice with manual alignment.

Several configurations were investigated to optimise the splicing performance of PM2000D. Figure 5.10(a) shows the experimental setup to acquire the reference ASE. The PM-OC was directly connected to the PM-ISO. The alignment of the optical axes of these PM1550 fibres was performed using the auto-aligning function of the splicer (ARCMaster FSM-100P, Fujikura). The reference ASE is presented as a black curve in Figure 5.11, which reveals a smooth ASE curve with a wavelength ranging from 1800-2100 nm. The result indicates optimal splicing performance between these PM fibres, where the optical axes were perfectly aligned.

Figure 5.10(b) presents an experimental setup for the splicing of PM2000D. A section of PM2000D was directly spliced to PM1550 pigtails of PM-OC and PM-ISO. The alignment of the optical axes at both splice points was conducted using the auto-aligning program of the splicer. The red curve in Figure 5.11 illustrates a measured transmitted ASE from this experiment. Compared to the reference ASE, the transmitted ASE has a high insertion loss due to the core-size mismatch between PM1550 and PM2000D. Additionally, the transmitted ASE exhibits ripples that indicate an unreliable PM performance in this splice configuration.

Figure 5.10(c) shows an approach of directly splicing PM2000D using the manual alignment method. In this configuration, the alignment of the optical axes between PM1550 and PM2000D was adjusted manually while the output ASE was simultaneously monitored. The blue curve in Figure 5.11 presents the best achieved output ASE spectrum resulting from this method. The spectrum exhibits a decrease in ripples compared to the auto-alignment method result (red curve). This result indicates an improvement in the PM performance. However, splicing loss remains comparable to the previous method due to the core size mismatch.

Figure 5.10(d) depicts a configuration to optimise the splicing of PM2000D with the bridge-fibre splice method. To minimise splice loss associated with the core size mismatch, short (<10 cm) sections of PM1950 (Coherent) with an intermediate core size (7 μm) have been incorporated at both ends of the PM2000D to function as bridge fibres. The alignment between PM1950 and PM2000D was manually conducted, while monitoring the transmitted ASE signal. The green curve in Figure 5.11 reveals the transmitted ASE spectrum resulting from the bridge-fibre splicing method. The spectrum exhibits a reduction in splicing loss and resolves ripples, indicating optimal splicing performance between these fibres. The bridge-splice method is used in subsequent experiments to ensure optimal splicing performance of PM2000D with passive fibres. This method is crucial for the development of dissipative-soliton ML-TDFLs in all-PM configurations, which are explored in the following sections of this thesis.

5.3.3 CNT-based all-PM dissipative soliton

A schematic of the all-fiberised PM ML-TDFL is presented in Figure 5.12. A 1563-nm CW-seeded EDFA (EDFA; EAD-5K-C, IPG Fibertech) was used as a pump, offering the maximum power of 7 W. This pump was coupled into a short (8 cm) section of PM-TDF (TDF; PM-TSF-5/125, Coherent) through a PM-WDM to enable the SWIR operation. To eliminate the residual pump, another PM-WDM was employed at the output of the PM-TDF. A fast-axis-blocked PM-OC was utilised to extract 90% of oscillating energy for a laser output, while maintaining a single polarisation of transmitted light aligned with the slow axis. Unidirectional oscillation was ensured by integrating a fast-axis-blocked PM-ISO, which also functions as a linear polariser. To facilitate dissipative-soliton ML operation, a fiberised LF was integrated at the fibre connection between the PM-OC and the PM-ISO. A 11-cm length of PM-SMF was spliced using an offset-splice method, with the configuration as detailed in Section 5.2.2. The inset of Figure 5.12(a) presents a schematic of the fiberised LF structure. The filtering effect of the fiberized LF is illustrated in Figure 5.13 (red line), revealing a periodic transmission characterisation compared with the input ASE signal. The maximum transmission peak is found at a central wavelength around 1876 nm with a FSR of 72 nm and a FWHM of 36 nm, corresponding to the estimated FWHM value of 37.7 nm [202, 203]. The LF insertion loss at the peak wavelength is ~0.4 dB. The ADSWNT CNT sample, detailed in Section 4.2, was attached between two angled fibre patch chords at the output of the PM-ISO, functioning as a SA. The ADSWNT provides saturable absorption with a modulation depth of 23.1% and a saturation fluence of 56.1 μJ/cm^2. A 4-m length of PM-DCF (PM2000D, Coherent) was spliced in the cavity to manage the net cavity dispersion. The splice points of the PM-DCF were accompanied by the bridge-splice method, as explained in Section 5.3.2, resulting in a total splicing loss of ~1.7 dB. The total cavity length was 10.6 m with an estimated net dispersion of 0.01 ps^2 (TDF: β_2 = -0.02 ps^2/m; SMF: β_2 = -0.059 ps^2/m; PM1950: β_2 = -0.02 ps^2/m DCF: β_2 = 0.098 ps^2/m at 1.9 μm) [191, 206]. Figure 5.12(b) presents a picture of the all-fiberised-PM cavity.

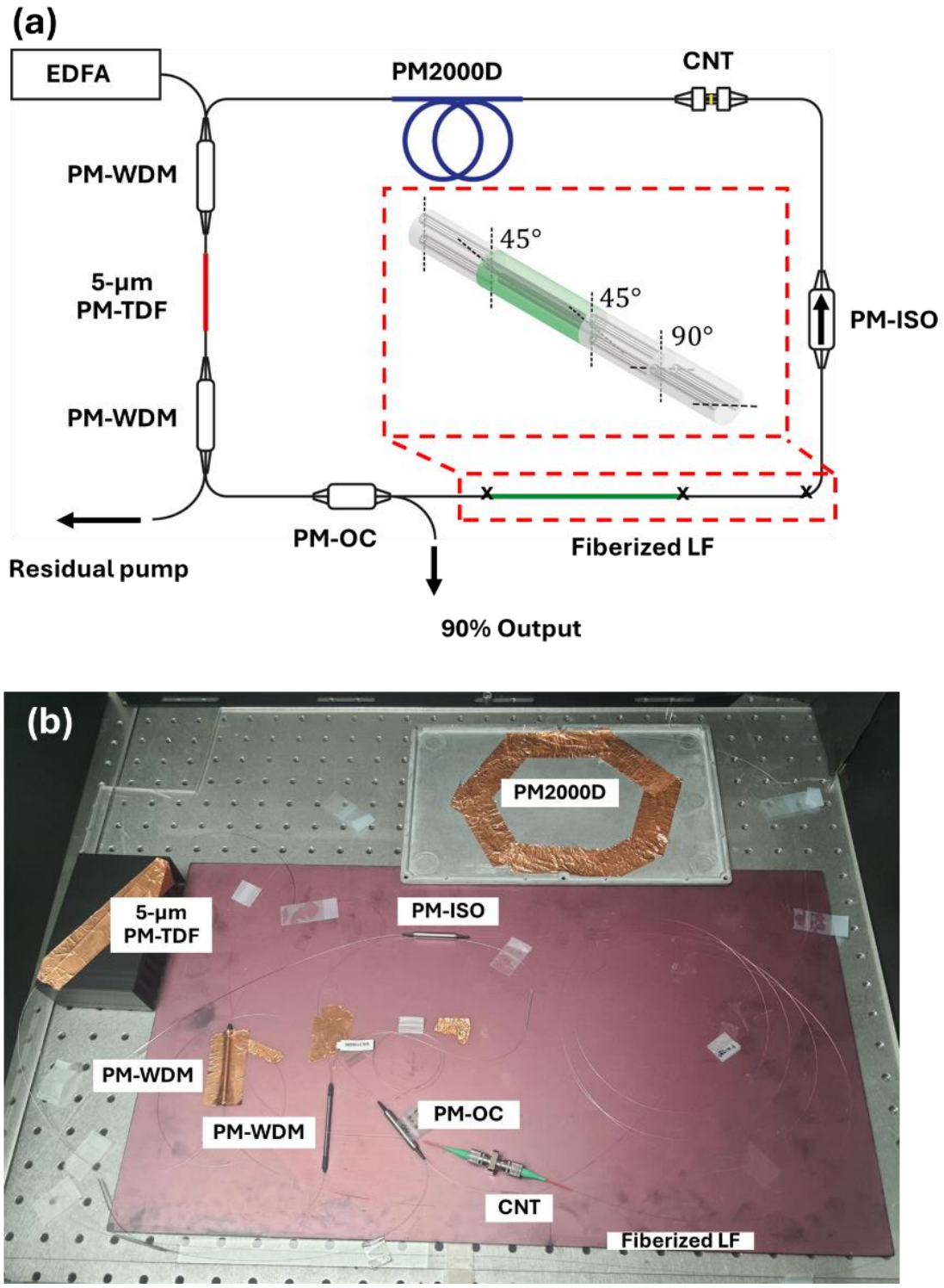

Figure 5.12 (a) Schematic of an all-fiberised, polarisation maintaining (PM) dissipative-soliton thulium-doped mode-locked cavity with carbon nanotube saturable absorber, and (b) picture of the cavity. EDFA: erbium-doped master oscillator fibre amplifier; PM-WDM: PM-wavelength-division-multiplexer; PM-TDF: PM-thulium-doped fibre; PM-OC: PM-output coupler; and PM-ISO: PM-isolator. The content in this figure was reproduced from my own publication [197], published by Elsevier Ltd. under a Creative Common license.

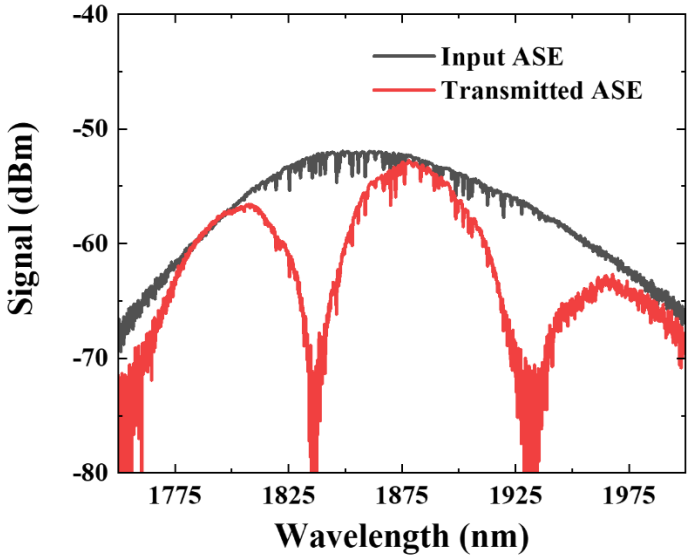

Figure 5.13 Measured amplified spontaneous emission (ASE) signal at (black curve) input, and (red curve) transmitted ASE after the Lyot filter. The content in this figure was reproduced from my own publication [197], published by Elsevier Ltd. under a Creative Common license.

Self-start ML operation was achieved at a pump power of 870 mW, without requiring any PCs or adjustment mechanisms, generating an output power of 7.2 mW. The single-pulse ML operation was stably maintained with increasing pump powers and provided a maximum output power of 21.5 mW. Unstable operation was observed for higher pump powers. Figure 5.14(a) presents the output power efficiency of this laser, demonstrating a slope efficiency of 17.9%. The output spectra were recorded at various output powers using an OSA (AQ6375, Yokogawa), revealing a sharp-edge spectral shape as typical of dissipative solitons [21, 175], as shown in Figure 5.14(b). The spectrum bandwidth expands with increasing output power. At the maximum power, the spectrum has a central wavelength of 1876 nm with a 3-dB bandwidth of 26 nm.

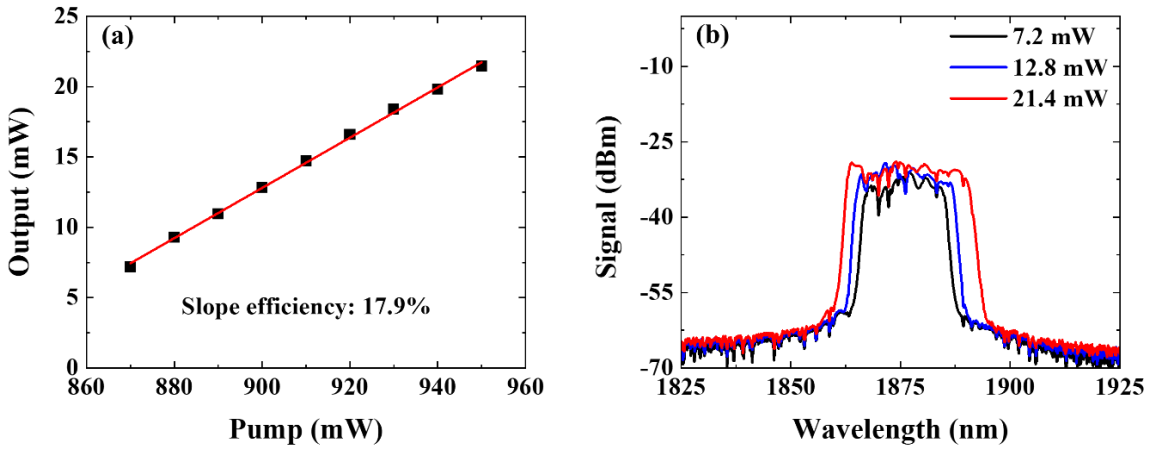

Figure 5.14 (a) output power efficiency of the mode-locked cavity, and (b) output spectra at different powers. The content in this figure was reproduced from my own publication [197], published by Elsevier Ltd. under a Creative Common license.

The ML stability was characterised by the recording of RF spectra using an InGaAs photodiode (ET-5000F, EOT) and a RF spectrum analyser (RSA3303A, Tektronix). The RF spectrum, measured at a resolution of 200 Hz, is presented in Figure 5.15(a). The result reveals a fundamental frequency of 19.2 MHz with a signal-to-noise ratio (SNR) of ~71 dB. The measured frequency is in good agreement with the estimated value calculated from the cavity length. Additionally, the high SNR indicates stable single-pulse ML operation. Figure 5.15(b) presents the RF spectrum, recorded with a wide span range across a 1-GHz bandwidth, without any parasitic instabilities. Consequently, the maximum calculated pulse energy is 1.1 nJ.

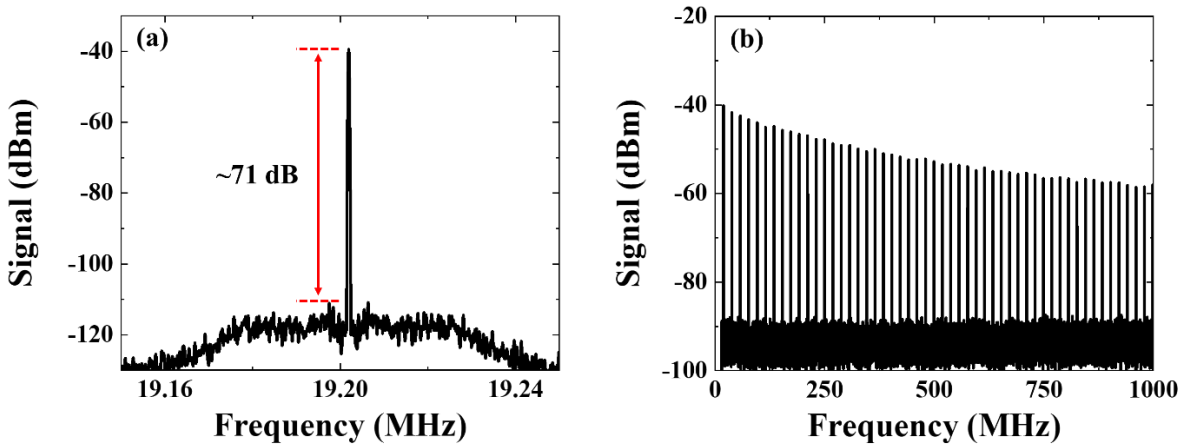

Figure 5.15 Radio frequency (RF) spectrum of the output signal with (a) 100 kHz span at the fundamental frequency and (b) 1 GHz span. The content in this figure was reproduced from my own publication [197], published by Elsevier Ltd. under a Creative Common license.

An output pulse duration was measured using an autocorrelator (pulseCheck NX150, APE). The autocorrelation function (ACF) curve of the output pulse is presented in Figure 5.16(a), exhibiting a width of 5.9 ps, which corresponds to the actual pulse duration of 4.2 ps based on the Gaussian-shape assumption. The pulse can be compressed using a home-built, grating-pair compressor consisting of two transmission gratings with a density of 900 line/mm. Figure 5.16(b) presents the shortest compressed pulse duration of 391 fs under the Gaussian-shape assumption. It is worth mentioning that the compressed pulse duration is 1.96 times larger than the calculated transform-limited pulse. This might be caused by a nonlinear chirp that could not be compensated by the grating-pair compressor, which could possibly be improved by further management of higher-order dispersion in the cavity [64, 195].

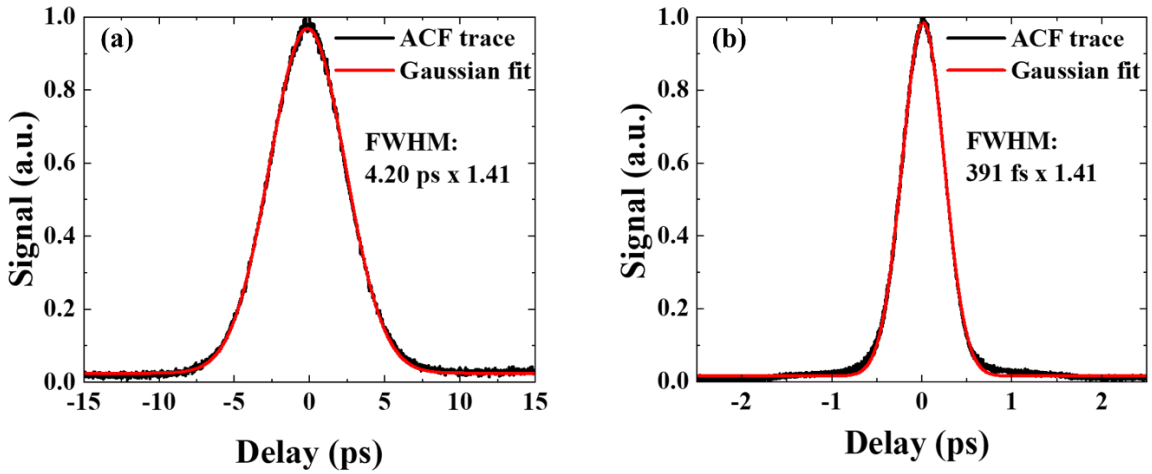

Figure 5.16 (black curve) Autocorrelation function (ACF) trace along with (red curve) Gaussian fit of (a) uncompressed pulse duration, and (b) compressed pulse duration. The content in this figure was reproduced from my own publication [197], published by Elsevier Ltd. under a Creative Common license.

The output power stability was further characterised by monitoring the output power and spectrum over a 6-hour duration in a laboratory environment. Figure 5.17(a) presents the recorded output power over this experiment session, revealing good power stability with a small fluctuation of ±1%. This fluctuation might possibly be attributed to the fluctuations of pump power during the experiment. Furthermore, the output spectrum was acquired at 1-hour intervals, exhibiting good repeatability of the output spectrum, as presented in Figure 5.17(b).

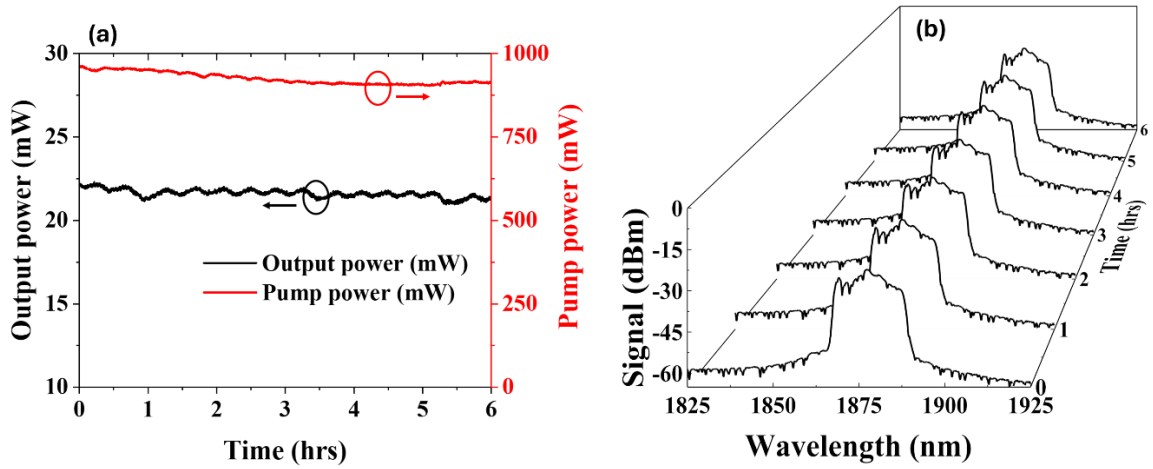

Figure 5.17 (a) Power stability measurement of (black curve) output signal (red curve) pump signal, and (b) Output spectrum with 1-hour interval time for 6 hours. The content in this figure was reproduced/adapted from my own publication [197], published by Elsevier Ltd. under a Creative Common license.

The net dispersion of the cavity was varied to examine the effect of dispersion variation. By adjusting the length of the PM-SMF to achieve a total cavity length of 10.2 and 9.7 m, the estimated net dispersion was determined to be 0.03 and 0.06 ps^2, respectively. Consequently, the

repetition rate of the cavity shifts to 20 and 21.1 MHz, corresponding to the total cavity length. As presented in Figure 5.18, output spectra were recorded at different net dispersions. As expected, a spectral bandwidth decreases with a larger net dispersion [55]. Furthermore, the cavity can tolerate higher pump powers and generates higher output powers [21]. For example, the cavity with a net dispersion of 0.06 ps^2 can maintain ML operation until the pump power reaches 1.2 W, resulting in a maximum pulse energy of 3.2 nJ. However, this configuration yields a longer compressed pulse duration of 566 fs compared to the cavity with lower net dispersions. Figure 5.19(a) presents the trend for the maximum pulse energy and the shortest compressed pulse duration across various net dispersions, confirming the influence of dispersion variation in this dissipative-soliton cavity. Additionally, ACF traces of compressed pulse durations at pulse energies of 2.4 nJ and 3.2 nJ are presented in Figure 5.19 (b) and (c), respectively.

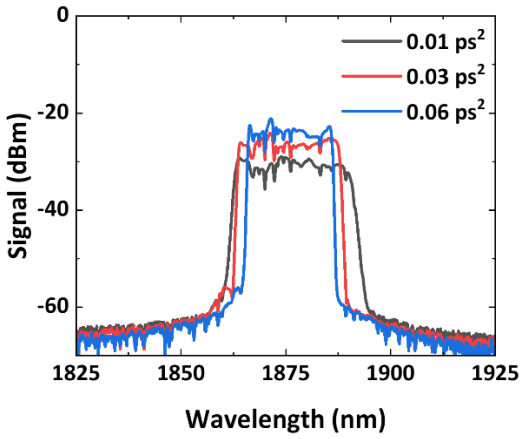

Figure 5.18 Output spectra with different net-cavity dispersions.

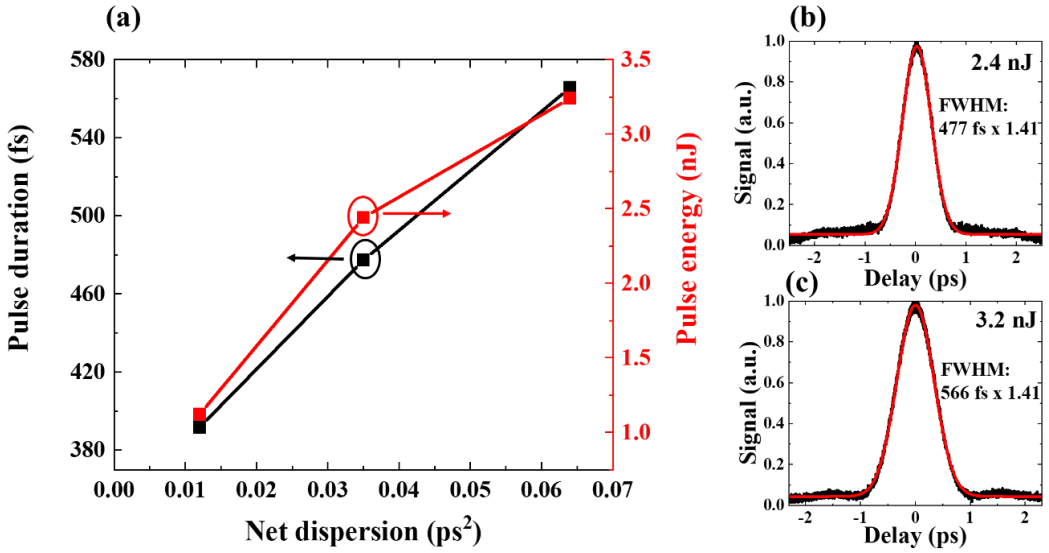

Figure 5.19 (a) output pulse properties with different net-cavity dispersions showing (black curve) compressed pulse duration and (red curve) maximum pulse energy, autocorrelation trace along with Gaussian fit for (b) 2.4 nJ and (c) 3.2 nJ. The content in this figure was reproduced from my own publication [197], published by Elsevier Ltd. under a Creative Common license.

5.4 Summary

I reported the development of an all-fiberised, all-PM ML-TDFL, enabled by CNT-SA. To achieve the goal of generating dissipative solitons, this chapter also discusses the study of a fiberised Lyot filter and, more importantly, a technique to improve the splicing of PM-DCF with PM-SMF reducing the intra-cavity losses. This knowledge will be further implemented in other PhD work, which will be explained later in the following chapters.

In this chapter, a robust, fully fiberised PM dissipative-soliton ML-TDFL operating at 1876 nm is presented. The ML cavity, with a net dispersion of 0.01 ps^2, provides a maximum output pulse energy of 1.1 nJ at a repetition rate of 19.2 MHz. The pulse duration was 4.2 ps and can be compressed down to 391 fs with a grating-pair compressor, under the Gaussian-shape assumption. To the best of my knowledge, this cavity is the first demonstration of a nJ-energy-level, all-PM dissipative-soliton ML-TDFL utilising commercially available PM-DCF and a CNT-SA. The net-cavity dispersion can be further varied to generate a higher pulse energy of 3.2 nJ. However, this results in a longer compressed pulse duration of 566 fs. This stable, 'turnkey' ML-TDFL has demonstrated good stability for a long-run experiment in the laboratory environment. I believe that this cavity design has high potential to be further improved and to serve as a reliable seed cavity for a laser used in biomedical imaging applications.

Chapter 6 1840 nm all-PM mode-locked laser system

In this chapter, I present an all-fiberised polarisation-maintaining mode-locked thulium-doped fibre laser, along with a chirped-pulse amplification system and a grating-pair compressor, as a portable laser system. I developed an all-fiberised PM ML-TDFL that generates ultrafast pulses at 1840 nm. This cavity was utilised to provide a seed signal in a CPA system, where the pulses are effectively stretched and amplified to achieve the desired output power. To facilitate the compression of the pulses, a grating-pair compressor was constructed at the output end of the CPA system. The laser can produce output pulses with average power of ~600 mW. The laser exhibits single-pulse operation with a fundamental repetition rate of 15.15 MHz, matched with the calculated value based on the pulse round-trip time in the cavity. The laser has an output pulse energy of ~40 nJ with a shortest compressed pulse duration of 493 fs, assuming a Gaussian pulse shape. This laser system is designed to be a robust, turnkey light source that can be easily operated by non-specialist users in biomedical imaging experiments, as part of the InLightenUS project. The advancements explored in previous chapters have been incorporated into this laser system. The development of this laser was carried out at the ORC by myself and Dr Lin Xu. The laser has been delivered to our external project partner at the University of Nottingham, where the research group, led by Professor Amanda Wright, is conducting biomedical imaging experiments utilising adaptive optics.

This chapter is outlined in four sections. The first section discusses the background of ML-TDFL lasers for biomedical imaging applications. The second section explains the development of a reliable EDFA pump source. The third section explains the development of the all-PM laser system, including the seed cavity, the pulse stretcher, the amplifiers, and the compressor. The summary of this chapter is given in the final section.

6.1 Background

As previously stated in Section 1.2, ultrafast SWIR pulses have the potential to be used as light sources in biomedical imaging applications. Ultrafast pulses with a central wavelength of 1820 nm and a pulse duration of 150 fs have demonstrated 3-photon biomedical imaging [16]. However, that laser was developed using fluoride-glass fibres, which require free-space components due to the challenge of splicing to standard silica-glass fibres. This would pose difficulties in the practical application of the laser. Previously in our research group, we have demonstrated an all-fiberised ML-TDFL at a central wavelength of 1840 nm with a pulse energy of 105 nJ, and a pulse duration of 416 fs [17]. This laser has exhibited outstanding performance in revealing detailed information from complex biomedical samples through nonlinear multiphoton

imaging. However, the laser was based on non-PM fibres, which are sensitive to physical perturbations. Moreover, this can lead to variations in laser output properties [198]. Therefore, all-PM ML-TDFL are preferred for reliable sources in biomedical imaging experiments.

6.2 Development of stable continuous-wave pump source

A reliable pump source is an essential component in a laser system. As discussed in the previous chapter, the output power of an all-PM ML-TDFL can vary in response to the fluctuation in pump power. In this section, I explain the development of a reliable EDFA that delivers a continuous-wave (CW) signal at ~1560 nm with minimal output power fluctuations. Additionally, this EDFA needs to have a robust and compact design for practical applications.

A schematic of the EDFA is presented in Figure 6.1(a). A wavelength-stabilised laser diode (976-nm LD; M976±0.5-9-F105/22-T1-P, Photontec Berlin GmbH) was utilised to generate a high-power CW pump signal at a central wavelength of 976 nm. The pump signal was coupled through a (2+1)x1 pump-signal combiner into a 2-m length of double-clad erbium-doped fibre (EDF; TC1500Y(11/125)HD, Fibercore). A CW seed signal at 1561 nm was provided by a compact laser diode with an output power of 10 mW. The seed was connected at the signal input pigtail of the combiner. Isolators were employed to mitigate any possible back reflection within the EDFA. Additionally, thermoelectric coolers (TECs) were incorporated to improve thermal stability of the 976-nm LD and the EDF. The EDFA was packaged into a compact enclosed box as presented in Figure 6.1(b).

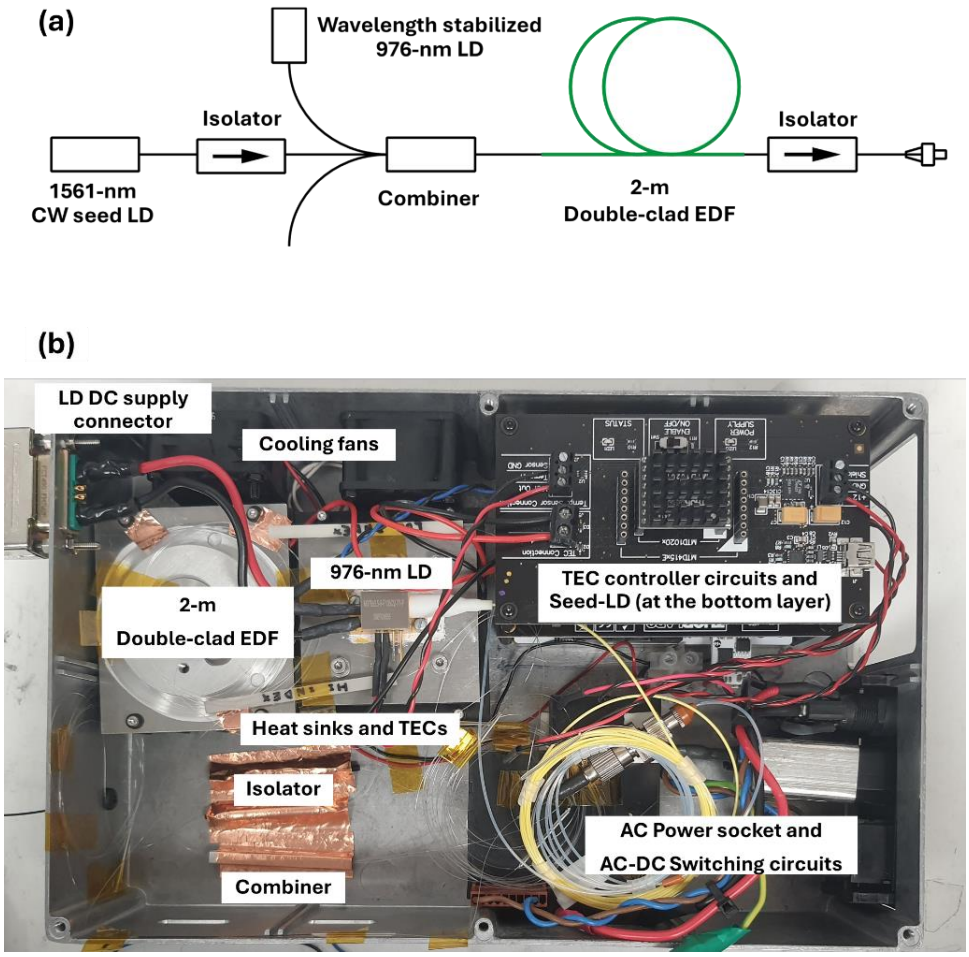

Figure 6.1 (a) Schematic of 1-LD erbium-doped master oscillator fibre amplifier (EDFA), and (b) picture of the EDFA in a final enclosure package. LD: laser diode; EDF: erbium-doped fibre; TEC: thermoelectric cooler.

The output power curve of the 976-nm LD is depicted in Figure 6.2(a). The laser threshold was found at a pump current of 0.5 A, which produced an output power of 0.06 W. The output power increased with the pump current and achieved the maximum output power of 7.13 W at a pump current of 8.5 A. The output spectra at various power levels are presented in Figure 6.2(b), which reveals stabilised signals at a central wavelength of 975.8 nm with a 3-dB bandwidth of 0.2 nm.

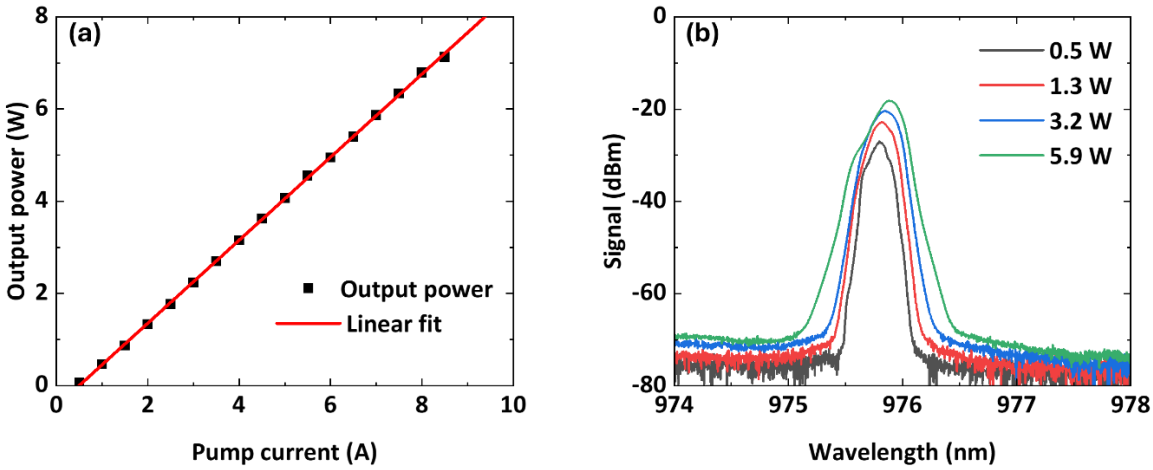

Figure 6.2 (a) Output power curve of the 976-nm pump laser diode (LD), and (b) output spectra of the 976-nm LD at different pump currents

The output power efficiency of the EDFA is depicted in Figure 6.3(a) (grey line). In the forward-pump scheme, the EDFA exhibits a slope efficiency of 10.8% and achieves a maximum output power of ~480 mW. Unfortunately, the power is not sufficient to initiate ML operation of the seed cavity. To achieve higher output powers, the components of the EDFA were reorganized into a backward-pump scheme configuration as depicted in Figure 6.4. Figure 6.3(a) (red line) presents an output slope efficiency of 23.6% with the backward-pump scheme and reaches the maximum output power of ~960 mW. Figure 6.3(b) presents an output spectrum of the EDFA at 850 mW, revealing a central wavelength of 1561 nm with a 3-dB bandwidth of 0.07 nm. The signal has a high optical signal-to-noise (OSNR) of 97 dB above the noise level.

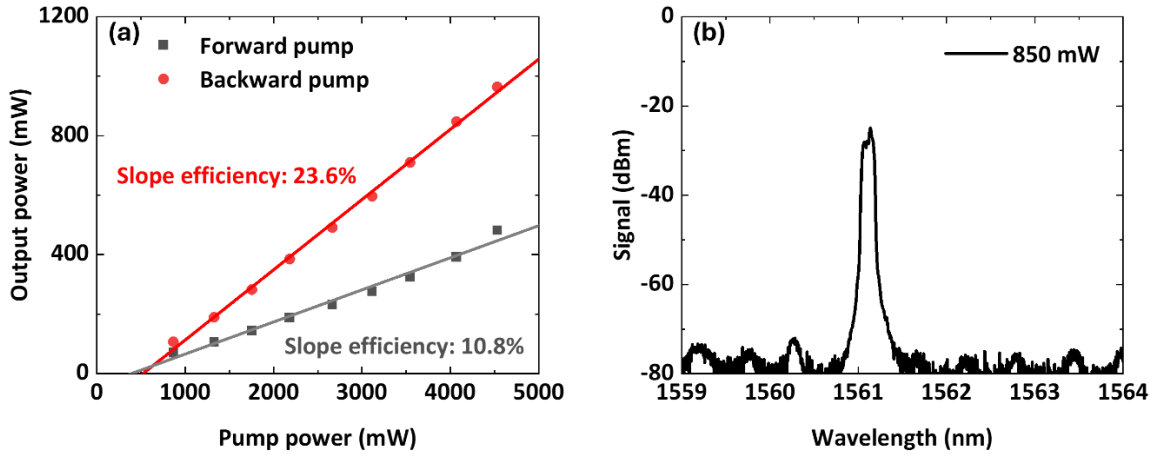

Figure 6.3 (a) Output efficiency of the erbium-doped master oscillator fibre amplifier (EDFA) with different pump scheme, and (b) output spectrum of EDFA at output power of 850 mW

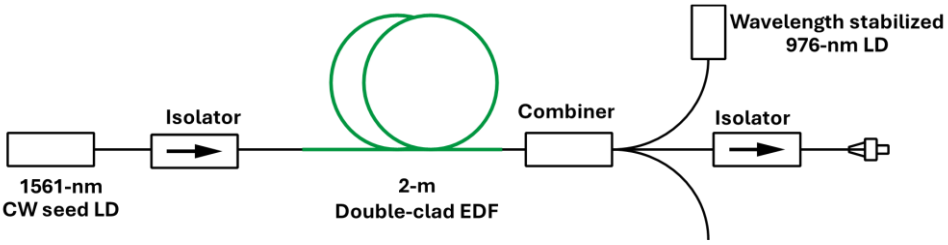

Figure 6.4 Backward-pump scheme of the erbium-doped master oscillator fibre amplifier (EDFA). LD: laser diode; EDF: erbium-doped fibre.

The stability of output power from this EDFA was evaluated for 1.5 hours within a laboratory environment. Figure 6.5 presents a comparison of the power stabilities of various EDFAs in our laboratory, highlighting the outstanding performance of this EDFA. Table 6.1 concludes the fluctuations observed in these EDFAs. The developed EDFA exhibits high power stability with a minimal fluctuation of 0.14%. This stability makes it suitable for using as a pump source for the 1840-nm all-PM ML-TDFL. The detailed information of this cavity will be explained in the following section.

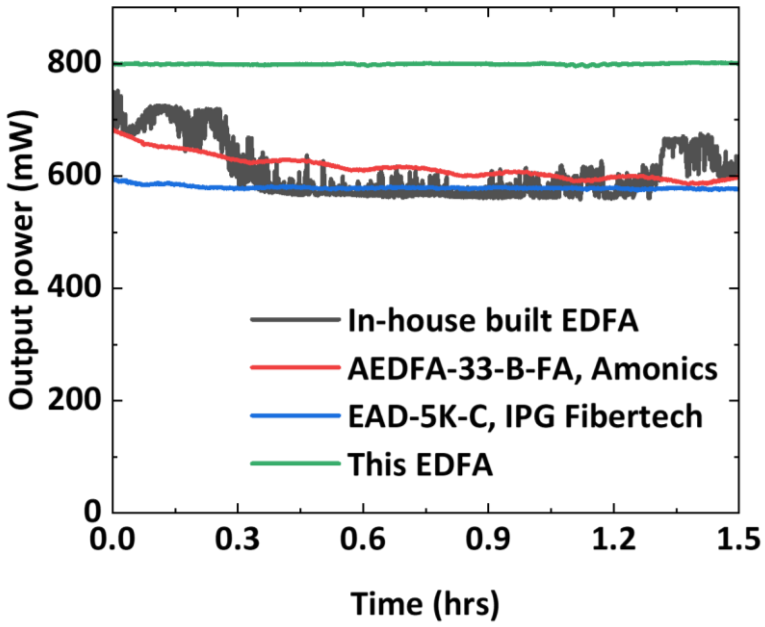

Figure 6.5 Output power stability of the developed erbium-doped master oscillator fibre amplifier (EDFA), compared to previous in-house built EDFA and commercial EDFAs. This experiment was observed in a normal laboratory environment.

Table 6.1 Stability comparison of the erbium-doped fibre amplifiers

EDFA	Average power (mW)	SD	Fluctuation (%)
In-house built EDFA	609.5	50.5	8.29
AEDFA-33-B-FA, Amonics	615.4	21.9	3.56
EAD-5K-C, IPG Fibertech	579.6	3.14	0.54
This EDFA	**799.4**	**1.14**	**0.14**

6.3 1840 nm all-PM mode-locked laser system

In this section, I explain the development of an 1840 nm all-PM ML laser system, which has been designed to be a portable light source for biomedical imaging experiments. This laser is expected to deliver high-energy, ultrashort pulses in the SWIR and exhibits a robust, turnkey operation. All technical advancements explored in the previous chapter have been incorporated into this laser to enhance its reliability.

6.3.1 1840 nm all-PM mode-locked cavity

A schematic of an all-fiberised PM ML-TDFL is depicted in Figure 6.6(a). The CW pump signal at a wavelength of 1561 nm was provided by the compact EDFA, as explained in the previous section. The pump signal was coupled into the cavity through a 1560/1840 nm PM-WDM. To enable the generation of the SWIR, a 1-m length of the PM-thulium-doped fibre (PM-TDF; PM-TSF-9/125, Coherent) was employed. Another PM-WDM was connected at the end of the TDF to filter any residual pump. A PM-OC was employed to extract 30% of the oscillating power for laser output. Additionally, a fiberised LF, as explained in Section 2.4, was introduced by the offset-splice method of a 11-cm length PM-SMF. The LF was optimised to achieve a maximum transmission at ~1840 nm. A PM-ISO was used to ensure unidirectional oscillation in the cavity. A CNT (ADSWNT), used as a SA, was attached between two angled-fibre-end facets. The net cavity dispersion was controlled by a 4.5-m length of PM2000D, which was carefully integrated into the cavity with the bridge-fibre splice method (explained in Section 5.3.2). Other pigtails were connected by the PM-SMFs. The total length of this cavity was measured to be ~13.5 m with a net dispersion of ~0.02 ps^2. The cavity was securely assembled in a compact enclosure, as presented in Figure 6.6(b), to be employed as a seed cavity for the laser system.

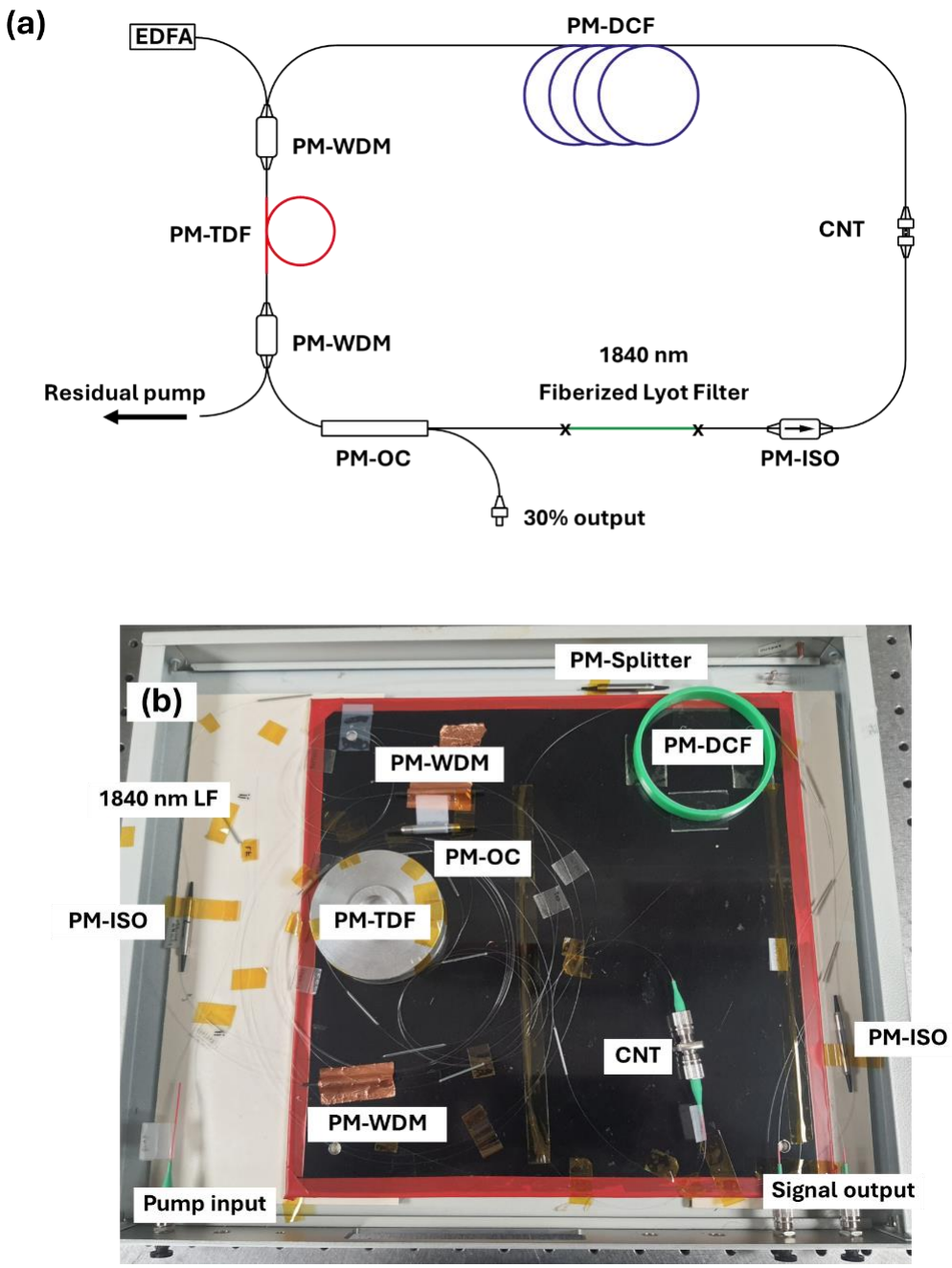

Figure 6.6 (a) Schematic of a 1840-nm all-fiberised all-polarisation-maintaining (PM) thulium-doped mode-locked cavity, and (b) picture of the cavity in a final laser setup package. EDFA: erbium-doped master oscillator fibre amplifier; PM-WDM: PM-wavelength-division-multiplexer; PM-TDF: PM-thulium-doped fibre; PM-OC: PM-output coupler; and PM-ISO: PM-isolator; CNT: carbon nanotubes saturable absorber; LF: Lyot filter.

At the ML threshold power of ~700 mW, the cavity exhibited a dissipative-soliton ML operation at a central wavelength of 1840 nm with a 3-dB bandwidth of 17.4 nm, as presented in Figure 6.7(a). This cavity is designed for a turnkey operation and demonstrates a self-start without requiring any PC in the cavity. Furthermore, ML operation was stable and persistent, resistant to physical perturbations. The average output power of the cavity is measured to be 1.5 mW. The radio frequency (RF) spectrum, acquired with a span range of 100 kHz and a resolution bandwidth of 200 Hz, presents a fundamental frequency at 15.15 MHz as shown in Figure 6.7(b). This

fundamental frequency corresponds to the estimated value based on the cavity length. The RF spectrum exhibits a signal-to-noise ratio (SNR) of 66 dB, indicating stable single-pulse operation. The 1-GHz span RF spectrum is presented in Figure 6.7(c), revealing no sign of parasitic lasing. Accordingly, the pulse energy was calculated to be 0.1 nJ. The uncompressed pulse duration was measured by an autocorrelator. The autocorrelation (ACF) trace of the output pulses is presented in Figure 6.7(d), revealing a width of ~6 ps, which is equivalent to the pulse duration of ~4.3 ps, based on the Gaussian-pulse assumption. This output pulse can be further amplified in a CPA system, which will be explained in the next section.

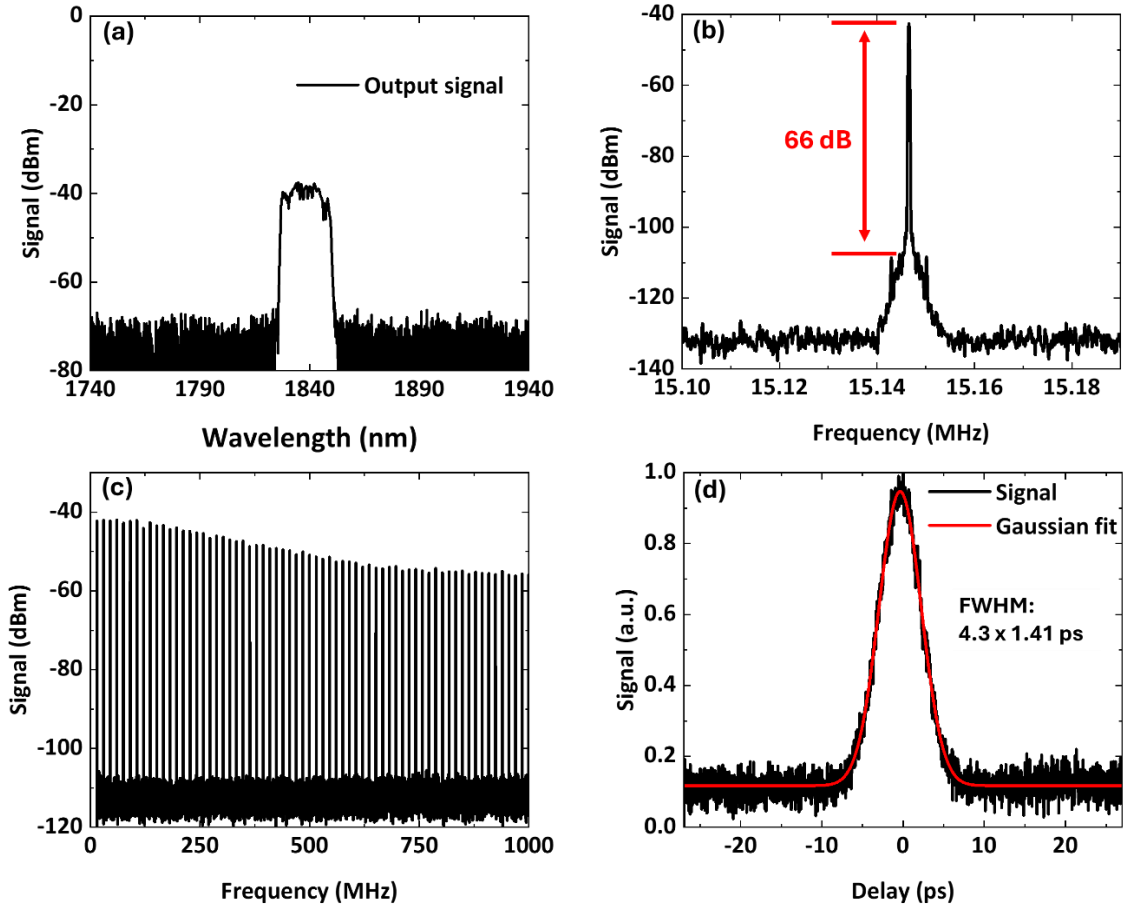

Figure 6.7 (a) Output spectrum of the mode-locked cavity, (b) frequency (RF) spectrum at the fundamental frequency acquiring with 100-kHz span range (resolution bandwidth 200 Hz), (c) RF spectrum with 1-GHz span range (resolution bandwidth 20 kHz), and (d) uncompressed pulse duration of the output pulses.

6.3.2 Amplifiers and pulse compressor

6.3.2.1 Pulse stretcher

The temporal width of the output pulse was expanded using a pulse stretcher to mitigate undesired nonlinearity in the amplifiers. A PM-ISO was employed at the laser output to prevent any potential back reflection into the cavity. Initially, the stretcher was intended to be constructed

by using a chirped fibre Bragg grating (CFBG). The CFBG has a positive chirp of ~3 ps^2 with a single reflection. However, the CFBG was not manufactured with a conventional PM-SMF and exhibited a reflectivity of only 15%. Consequently, the insertion loss of this CFBG was very high when used as a stretcher. Instead, a 26-m length of PM2000D was employed as the pulse stretcher. The bridge-fibre splice method was incorporated to minimise the insertion loss. The output power, measured after the stretcher, was ~0.8 mW. An ACF trace of the stretched pulses is presented in Figure 6.8, which corresponds to the Gaussian-shaped pulse duration of 28.2 ps. Subsequently, the stretched pulse can be efficiently amplified.

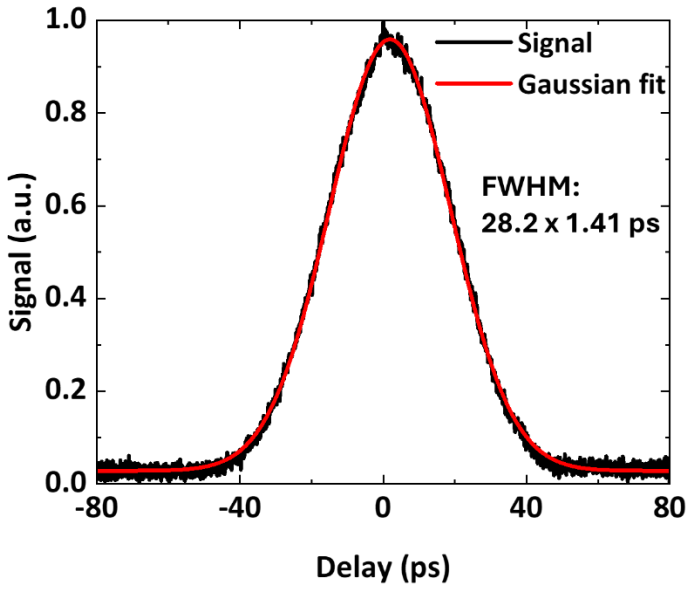

Figure 6.8 Stretched pulse duration using the 26-m length PM2000D.

6.3.2.2 First-stage amplifier

The first-stage amplifier was employed to pre-amplify the stretched pulse. This amplifier enables higher powers and improves the efficiency of the final amplifier. A schematic of the first-stage amplifier is presented in Figure 6.9(a). A 2-LD EDFL was constructed with the configuration explained in Section 3.2.1. This EDFL produced a CW laser signal at a wavelength of ~1560 nm and a maximum output power of 1 W. This signal was delivered as a pump for the amplifier through a PM-WDM into a 2-m length of 9-µm core PM-TDF (PM-TSF-9/125, Coherent), facilitating optical gain for the SWIR. A PM-ISO was spliced to the output of the PM-TDF to prevent any possible back reflection. The pre-amplifier system and the 2-LD EDFL were mounted on a compact, thermally stabilised platform, as depicted in Figure 6.9 (b). The output efficiency of the first-stage amplifier is presented in Figure 6.10. The amplified output power increased with the pump power, yielding a slope efficiency of 2.7%. The maximum output power was measured to be ~22 mW. Despite the low slope efficiency, this amplifier generated sufficient output power for further amplification in the second-stage amplifier.

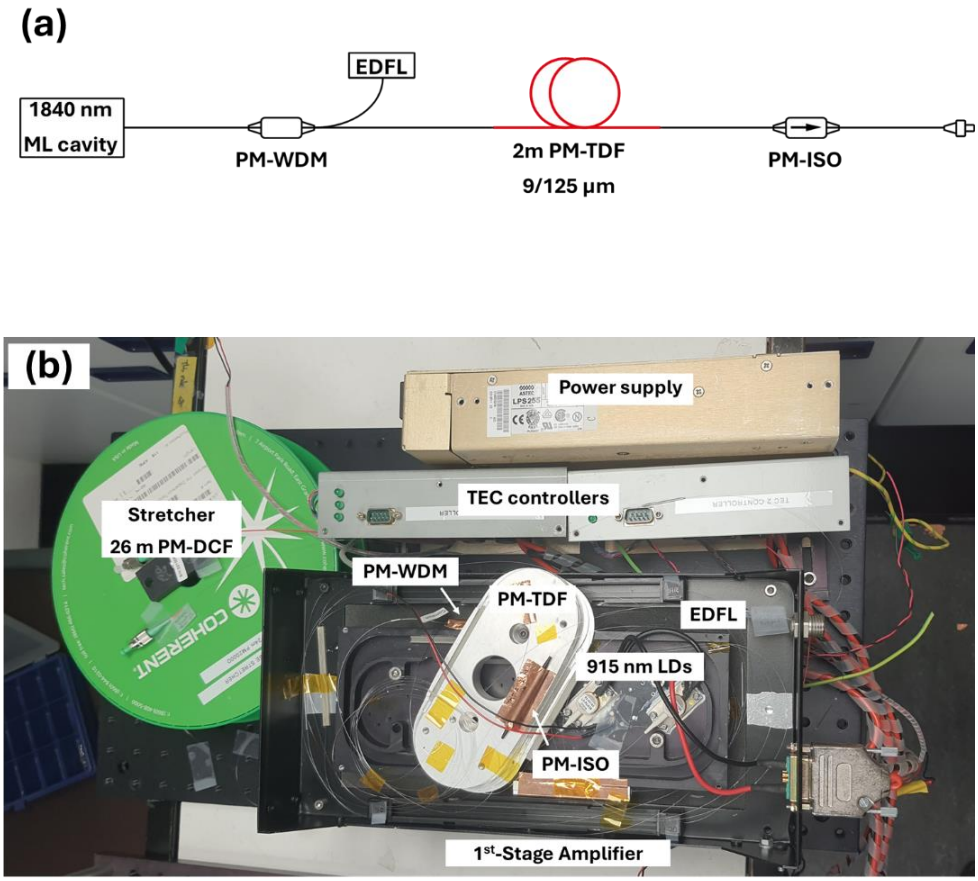

Figure 6.9 (a) Schematic of the first stage amplifier, and (b) picture of the first stage amplifier set on the same platform with the erbium-doped fibre pump laser (EDFL) (the stretcher was set in the green fibre spool). PM-DCF: polarisation-maintaining dispersion compensation fibre; TEC: thermoelectric coupler; PM-WDM: polarisation-maintaining wavelength-division-multiplexer; PM-TDF: polarisation-maintaining thulium-doped fibre; LD: laser diode; PM-ISO: polarisation-maintaining isolator.

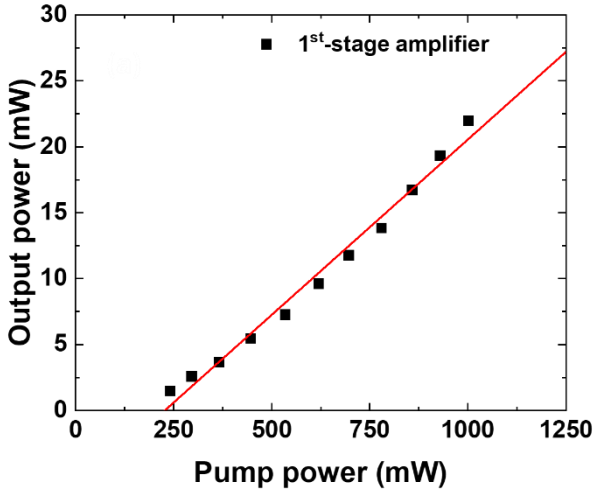

Figure 6.10 Output power efficiency of the first stage thulium-doped fibre amplifier.

6.3.2.3 Second-stage amplifier

The second-stage amplifier was employed to amplify the signal to the desired 1-W output power. A schematic of the second-stage amplifier is presented in Figure 6.11(a). A 6-LD EDFL was constructed with the configuration as explained in Section 3.2.1. to provide a pump signal at a wavelength of 1560 nm with a maximum power of ~5.5 W. The pump signal was coupled through a PM-WDM into the amplifier. To minimise the nonlinearity in the amplifier, a short section (15 cm) of double-clad PM-TDF (PM-TDF-10P/130-HE, Coherent) was selected as a gain fibre. It is worth noting that this TDF was measured to have high pump absorption (~99% of pump power was absorbed). This fibre has a large core size of ~10 μm and provides high pump absorption. Therefore, the SWIR signal can be efficiently amplified. A short section of angled pigtail was spliced as an output end. Free-space optics were employed at the output of the amplifier. An aspheric lens was set on a 3-axis translational stage to collimate an output beam, delivered from the fibre patch chord. A dichroic mirror was utilised to filter the residual pump. Figure 6.12 presents the output power efficiency of the second-stage amplifier, exhibiting an increasing output power with a slope efficiency of 31.4%. The amplifier generates an output power of 1 W at the pump power of 3.8 W. It is worth mentioning that the output power was limited to 1 W to prevent possible damage to the fibre patch chord, which might cause difficulties for laser delivery and maintenance in practical applications. The 6-LD EDFL and the second-stage amplifier were set on a compact, thermally stabilised-platform, as shown in Figure 6.11(b).

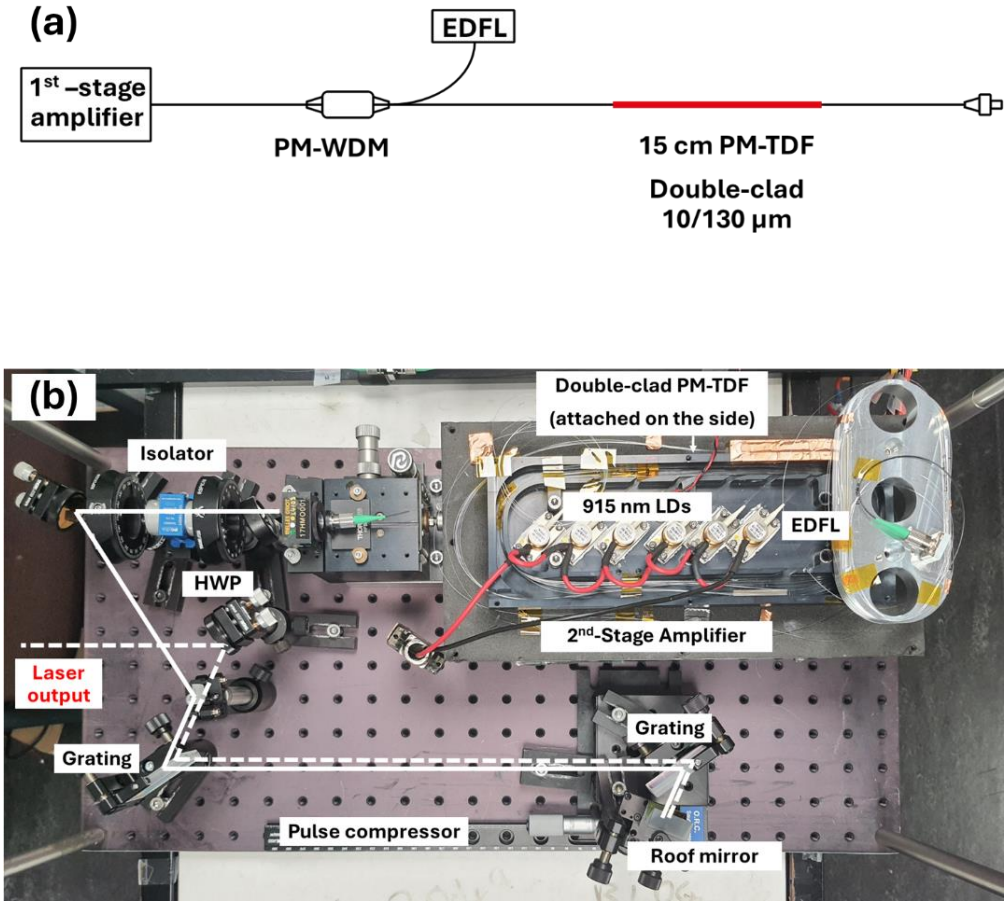

Figure 6.11 (a) Schematic of the second stage amplifier, and (b) picture of the second stage amplifier set on the erbium-doped fibre pump laser (together with the grating-pair compressor as a free-space optical setup). HWP: half-waveplate; PM-WDM: polarisation-maintaining wavelength-division-multiplexer; PM-TDF: polarisation-maintaining thulium-doped fibre; LD: laser diode; PM-ISO: polarisation-maintaining isolator.

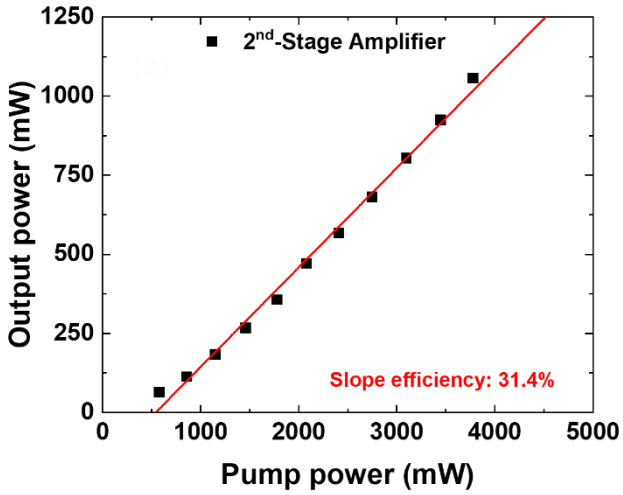

Figure 6.12 output efficiency of the second stage thulium-doped fibre amplifier.

Output spectra at each position in the laser system are presented in Figure 6.13. The results reveal that there is no notable nonlinearity distortion in the amplifiers. The final output spectrum of this laser has a high OSNR of ~30 dB.

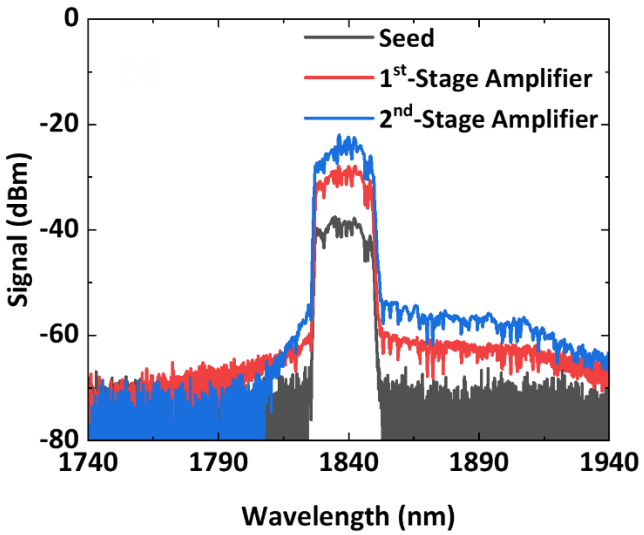

Figure 6.13 Comparison of output spectrum at each stage in the laser system

6.3.2.4 Pulse compressor

The output pulse duration can be de-chirped to the hundreds-of-fs level by using a grating-pair compressor, setting with free-space optics components after the amplifier, as shown in Figure 6.11 (b). An isolator was employed to ensure the directional transmission of the signal and to prevent any potential back reflection. A half-waveplate (HWP) was placed at the entrance of the isolator to optimise the transmitted power regarding to its polarisation-dependent loss. Gold-coated mirrors were used to guide the transmitted light to incident onto the transmission grating with a density of 900 lines/mm. The grating transmission was optimised by adjusting another HWP employed at the output of the isolator. Another identical grating was mounted in parallel to the first grating. The separation distance between these gratings can be adjusted to achieve the shortest compressed pulse duration. A reflective hollow roof mirror is used to reflect this signal back to the grating pair at a slightly different position and complete double-pass propagation as the 'Treacy configuration' compressor (Section 2.6.3). Figure 6.14 depicts the ACF trace of the shortest compressed pulse duration, equivalent to the pulse duration of ~493 fs, with Gaussian-pulse assumption. Due to the insertion loss of guided-optics components in the compressor, the average power of the compressed pulse was ~600 mW, equivalent to the pulse energy of ~40 nJ (with an estimated peak power of ~81 kW).

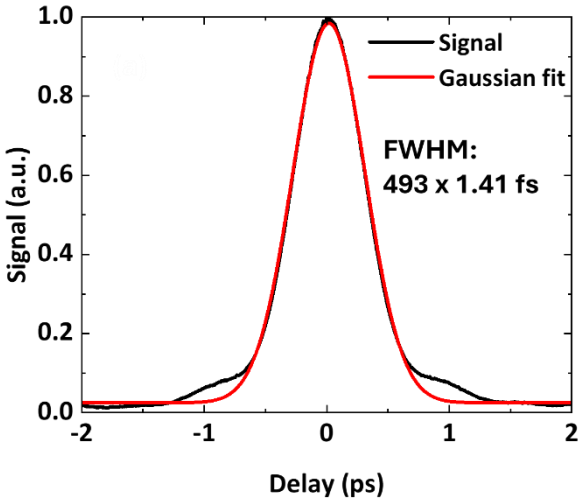

Figure 6.14 Compressed pulse duration at the output pulses.

The schematic of the laser system is presented in Figure 6.15(a). Each stage of the system was mounted on a 30 x 60 cm optical breadboard and placed in a stacked configuration, as shown in Figure 6.15(b). The total height of this laser was 50 cm. The laser has been delivered to our external project partner laboratory at the University of Nottingham, where it is employed as a reliable light source in biomedical imaging experiments with adaptive optics. The laser has provided consistent output pulse properties, confirming the robustness of this system.

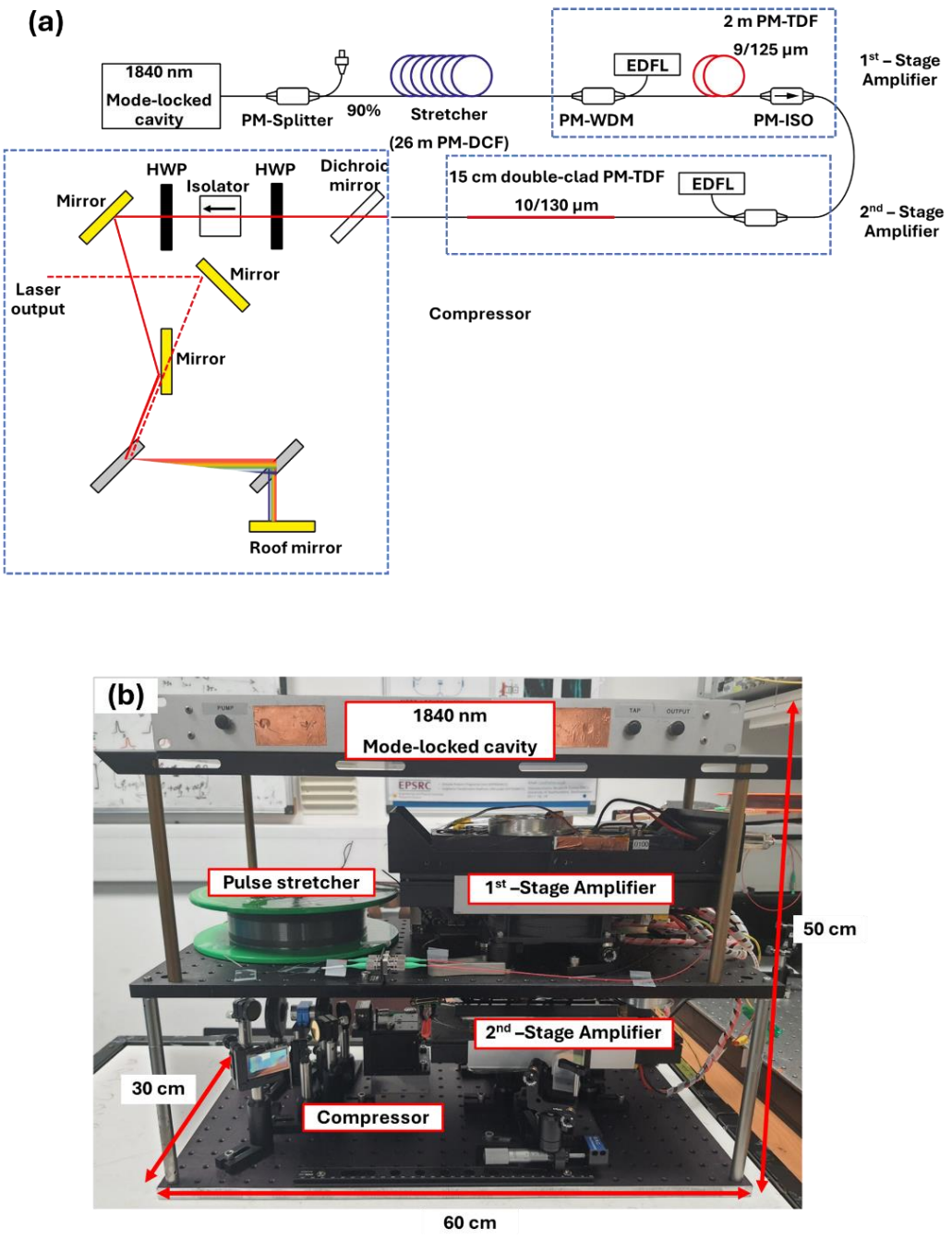

Figure 6.15 (a) Schematic of the 1840-nm all-polarisation-maintaining laser system, and (b) picture of the laser system.

6.4 Summary

In this chapter, I have demonstrated the development of a 1840-nm all-PM laser system, which can be employed for functioning as a reliable light source in biomedical imaging experiments. The laser is robust and can be operated as a 'turnkey' light source. The laser generated output pulses at a central wavelength of 1840 nm with a pulse energy of 40 nJ and a pulse duration of 493 fs. The The laser has been delivered to our external project partner at the University of Nottingham. The biomedical imaging experiments are still ongoing by the time of the thesis submission.

Chapter 7 All-PM dissipative-soliton mode-locked fibre laser enabled by NALM

In this chapter, I present an experiment to develop an all-fiberised PM dissipative-soliton ML-TDFL, enabled by a nonlinear amplifying loop mirror saturable absorber. To the best of my knowledge, this is the first demonstration of the nJ-level dissipative soliton with an all-fibre, all-PM ML-TDFL at the SWIR, enabled by NALM-SA. Various advanced techniques have been incorporated to achieve the desired pulse properties. Single-pulse ML laser operation with a central wavelength of 1860 nm and a pulse energy of 1.5 nJ was demonstrated. The output pulse duration was compressed to a pulse duration of 539 fs. This cavity design also has great potential to be developed for biomedical imaging applications, with the advantages of having wide spectral wavelengths, high power handling, and less degradation.

This chapter consists of three sections. The first section explains the background of the NALM-based ML-TDFL. Detailed information on ML cavity development is given in the second section. This chapter is summarised in the final section. It is worth noting that the contents in this chapter have been published in [207]

7.1 Background

A saturable absorber is one of the key elements in passively mode-locked fibre lasers. In the previous chapters of this thesis, I have reported on ML-TDFLs using material-based SAs, i.e., SESAM (Chapter 3) and CNTs (Chapter 4). These SAs offer the advantage of controllable optical properties through the material structure design [76] and fabrication process [32]. However, the material-based SAs may encounter several potential technical problems, i.e., limited operating bandwidth [79], low damage threshold [76], or short lifetime [80]. To resolve these issues, fibre-based SAs can be utilised [81]. The saturable loss of fibre-based SAs depend on Kerr nonlinearity in optical fibres [25, 208, 209]. Therefore, fibre-based SAs offer significant improvements in power handling, wavelength limitations, and lifetime [82]. ML-TDFLs have been demonstrated using various fibre-based SAs, including nonlinear polarisation rotation [49, 60, 210], nonlinear optical loop mirror (NOLM) [37, 211], and nonlinear amplifying loop mirror (NALM) [35, 160, 212].

Net cavity dispersion is another important factor that controls the output pulse properties of ML lasers. Typically, single-mode fibres provide anomalous dispersion at 2-μm wavelengths [22]. Several all-fiberised PM ML-TDFLs have been demonstrated using all-anomalous dispersion fibres [25, 35, 37]. However, these cavities operate in the conventional-soliton regime, which

limits pulse energy to the pJ-level. To achieve higher pulse energies, dispersion management is required [21]. Stretched pulse ML cavities can be achieved by managing the net cavity dispersion to be close to zero [21]. In this regime, the oscillating pulses are periodically stretched and compressed, resolving the limitations of conventional soliton [174]. All-PM stretched-pulse ML-TDFL has been demonstrated in a figure-of-nine NALM cavity [213]. A near-zero net dispersion was satisfied by employing a 0.6-m length of PM dispersion compensation fibre (PM-DCF). This cavity generates ML operation at a wavelength of 1990 nm with a high repletion rate (121.3 MHz), and a low output pulse energy (0.3 nJ). The net cavity dispersion can be further increased into normal dispersion to achieve a dissipative soliton [21]. An all-PM dissipative-soliton ML-TDFL has been reported in a figure-of-eight configuration with a net dispersion of 0.14 ps^2 [205]. This cavity generates ML operation at a central wavelength of 1950 nm. However, the output power was only 0.12 mW at a repetition rate of 16.52 MHz, consequently, the output pulse energy was calculated to be only ~7 pJ. This issue might be caused by a high splice loss between the PM-DCF and other SMFs due to a large mode field diameter (MFD) mismatch.

7.2 NALM-based all-PM mode-locked fibre laser

In this section, I explain the development of an all-fiberised PM dissipative-soliton ML-TDFL, enabled by NALM-SA. This cavity was designed to demonstrate a pulse energy exceeding 1 nJ. The cavity includes one of the solutions to overcome the limitations of material-based SAs, namely a NALM-SA, in this experiment a 2x2 tuneable coupler (TC; FTDC-P-155-NO, Phoenix Photonics) was used. Figure 7.1(a) shows the image of the TC, allowing the manual adjustment of the coupling ratio via a calibrated tuning knob. The coupling ratio at different knob positions is presented in Figure 7.1(b). The effective transmission and the modulation depth of the NALM-SA can be controlled by changing the coupling ratio, according to the formula as stated in equation (2.32) (see Section 2.3.2.4). Figure 7.1(c) presents the calculated power-dependent transmittance derived from the equation. With varied coupling ratios, the results reveal different behaviours of saturable absorption and modulation depth in the NALM-SA. It exhibits a larger modulation depth at a smaller coupling ratio, indicating more favourable SA properties that assist ML initiation. However, higher powers are required to achieve the maximum transmission. In contrast, a larger coupling ratio results in a higher transmission, especially at powers below the “overdriven fluence regime”, where the transmission decreases with higher power [208]. Accordingly, NALM-SA associated with the TC can be configured to enhance the ML initiation and optimise the transmission for high output powers.

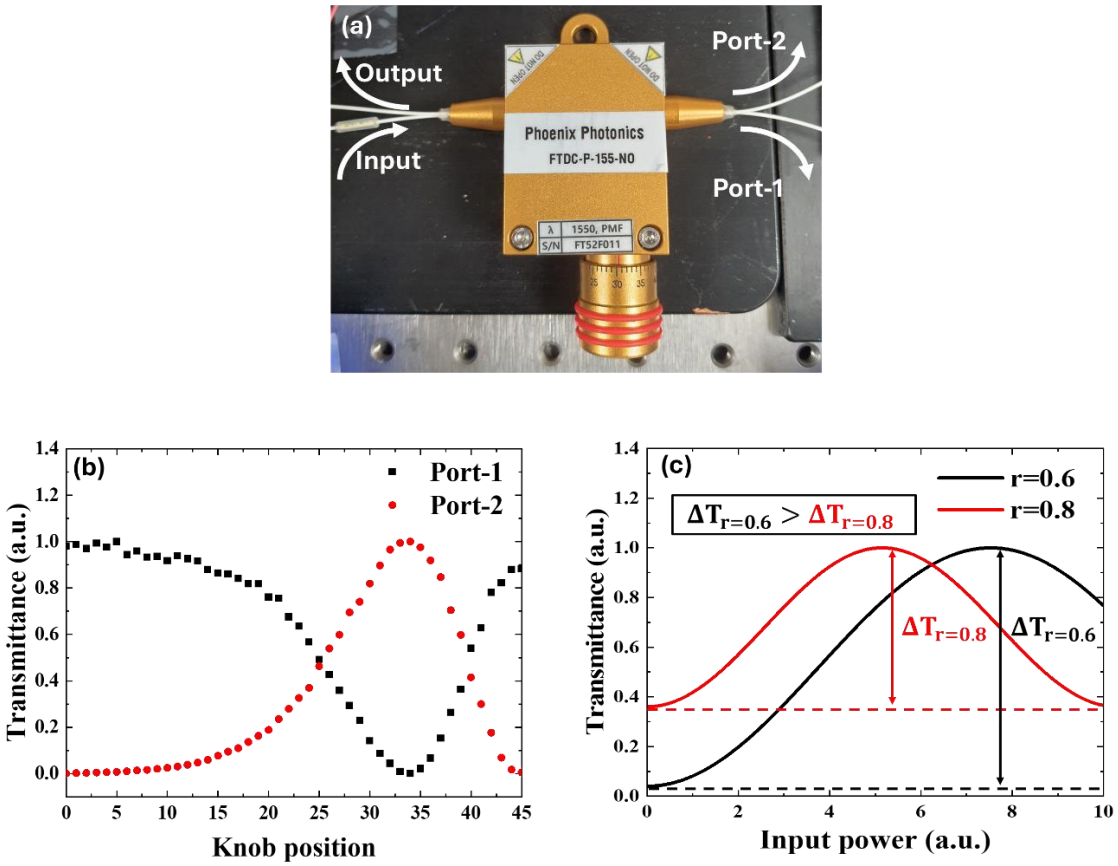

Figure 7.1 (a) Picture of the 2x2 tuneable coupler, (b) transmittance of the tuneable coupler at different knob positions, and (c) transmittance of the NALM-SA at different pump powers with various coupling ratio (r). ΔT represents the modulation depth. The content in this figure was reproduced from my own publication [207]. © 2025 Optica Publishing Group (Creative Commons Attribution 4.0 License)

Figure 7.2 presents a schematic of the NALM-based all-PM ML-TDFL, consisting of two fibre loops. A PM isolator (PMI) was employed in the unidirectional ring (UR; left) to ensure the oscillation direction. A PM output coupler (PM-OC) was spliced in the UR to extract 70% of oscillating power as the laser output. A fiberised Lyot filter (LF) was constructed using a 0.2-m length of PM-SMF positioned on the fibre tail between the PM-OC and the PMI. The offset-spliced method (explained in Section 5.2.2) was incorporated to prevent temporal walk-off and polarisation-dependent group velocity dispersion in the pulse-mode operation [165, 166]. Figure 7.3 illustrates a comparison of the wideband spectrum (black curve) and filtered spectrum after the LF (red curve). The results reveal a periodic bandpass filter with the maximum transmission at a central wavelength around 1860 nm with an insertion loss ~0.3 dB. From this measurement, the FSR and the FWHM are determined to be 40.4 nm and 20.9 nm, respectively. These measured values are in good agreement with the theoretically calculated FSR and FWHM, which are 40.7 nm and 20.4 nm, respectively [202, 203].

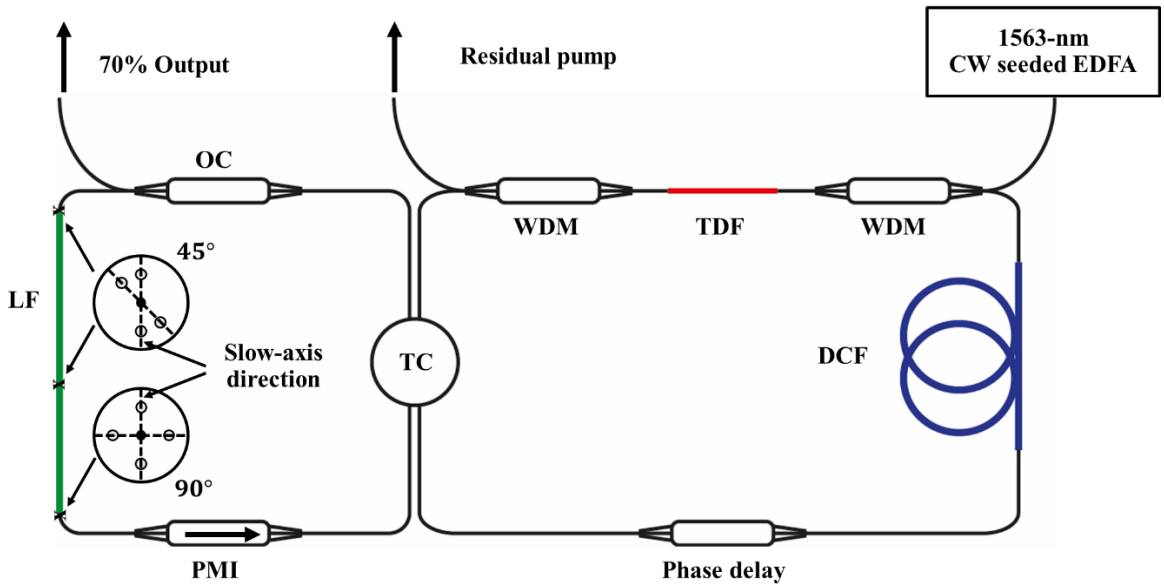

Figure 7.2 Schematic of an all-fiberised, polarisation-maintaining (PM) thulium-doped fibre laser based on a nonlinear amplifying loop mirror (NALM). TC: tuneable coupler; WDM: wavelength-division-multiplexer; TDF: thulium-doped fibre; DCF: dispersion compensation fibre; EDFA: erbium-doped master oscillator fibre amplifier; OC: output coupler; PMI: polarisation maintaining isolator; LF: Lyot filter. The content in this figure was reproduced from my own publication [207]. © 2025 Optica Publishing Group (Creative Commons Attribution 4.0 License)

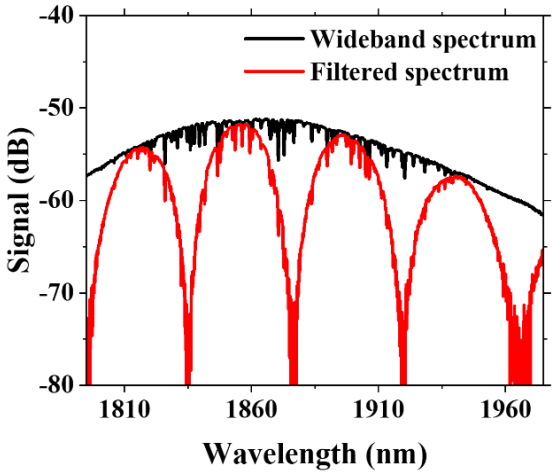

Figure 7.3 (black curve) wideband input spectrum, and (red curve) filtered spectrum with the Lyot filter. The content in this figure was reproduced from my own publication [207]. © 2025 Optica Publishing Group (Creative Commons Attribution 4.0 License)

The oscillating signal from the UR was coupled into the NALM loop (right loop in Figure 7.2) through the TC, with a controllable coupling ratio, as previously explained. A 1563-nm CW-seeded EDFA (EDFA; EAD-5K-C, IPG Fibertech) was employed to supply a pump signal with a maximum power of 7 W. The pump signal was coupled through a 1560/1840-nm PM-wavelength-division-multiplexer (PM-WDM) into a 15-cm length of PM thulium-doped fibre (TDF; PM-TDF-10P/130-HE, Coherent) to select the SWIR. The PM-TDF has low insertion loss when spliced to PM-SMF and provides sufficient gain with a short length, hence reducing the nonlinearity. It is worth noting that this short TDF section also minimises the re-absorption effect and favours the ML operation at

short wavelengths [112]. Another PM-WDM was connected at the end of the TDF to filter out the residual pump. A nonreciprocal phase delay was employed to introduce an additional half of a π phase difference between counter-propagating pulses as a bias to reduce the ML threshold [82]. A 5-m length of PM-DCF (PM2000D, Coherent) was utilised to manage the net cavity dispersion. The splice connections between PM2000D and PM-SMF were incorporated with the bridge-fibre splice method, as explained in Section 5.3.2. The total splice loss at 1860 nm was ~2.2 dB, which was significantly improved compared to a direct splice, which has a total loss of ~5.3 dB. This cavity has a total length of 13.1 m with an estimated net dispersion of ~0.02 ps^2.

With a pump power of 1.4 W and a coupling ratio of 0.6, the cavity generated a self-start, double-pulse ML operation. Subsequently, the single-pulse ML operation was realised by gradually reducing the pump power to 1 W and the output power optimised by adjusting the coupling ratio to 0.8. The single-pulse output power increases with pump power, yielding a linear slope efficiency of 9.5%, as shown in Figure 7.4(a). The maximum output power was measured to be ~23.8 mW at a pump power of 1.1 W. It is worth noting that the residual pump was measured to be ~8 mW at the maximum pump power. The output spectra at different powers are presented in Figure 7.4(b), exhibiting the sharp-edge, flat-top shape typical of a dissipative soliton [175]. At the maximum output power, the spectrum exhibits a central wavelength of 1860 nm with a 3-dB bandwidth of 18.6 nm.

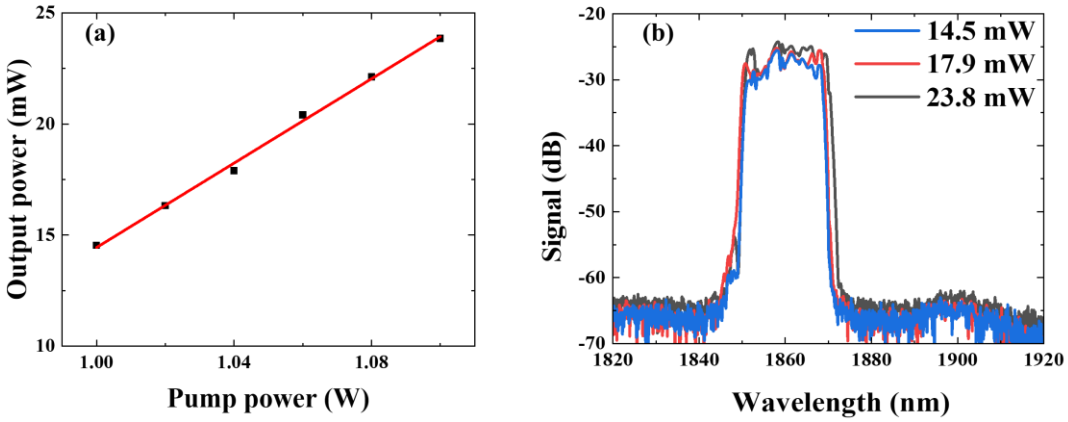

Figure 7.4 (a) Output powers and (b) output spectra of the laser at different powers. The content in this figure was reproduced from my own publication [207]. © 2025 Optica Publishing Group (Creative Commons Attribution 4.0 License)

An oscilloscope trace was recorded using a 10-GHz bandwidth InGaAs photodiode (ET-5000F, EOT) with a 1-GHz mixed signal oscilloscope (MSO7104A, Agilent Technologies). Figure 7.5(a) presents a stable pulse train, indicating an intracavity round-trip time of 64.2 ns, corresponding to a repetition rate of 15.5 MHz. The repetition rate is in good agreement with the estimated value from the total cavity length. Additionally, this repetition rate agrees with the measured radio frequency (RF) spectrum, recorded by a 3-GHz-bandwidth RF spectrum analyser (RSA3303A,

Tektronix). Figure 7.5(b) illustrates a 100-kHz-span RF spectrum, acquired at 200-Hz-bandwidth resolution, revealing a fundamental frequency at 15.55 MHz. The RF spectrum has a high signal-to-noise ratio (SNR) of ~70 dB, indicating stable mode-locked operation. Figure 7.5(c) depicts a 1-GHz-span RF spectrum, which confirms stable ML operation without any parasitic instabilities. Therefore, the maximum output pulse energy is calculated to be 1.5 nJ.

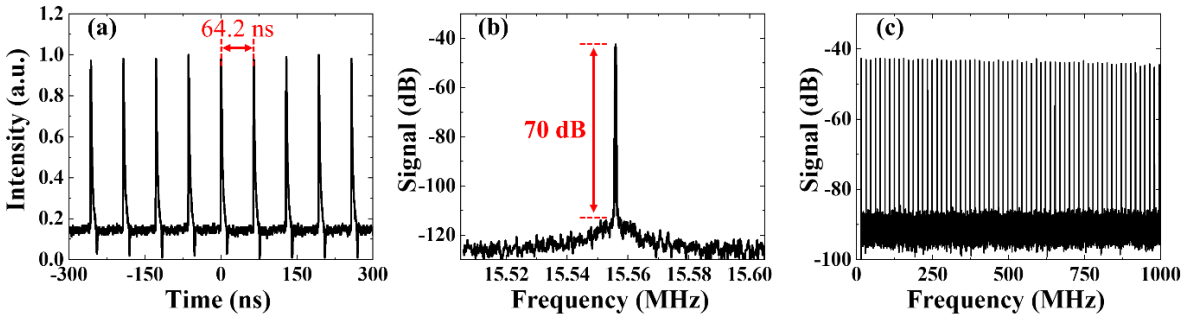

Figure 7.5 (a) Oscilloscope trace, (b) radio frequency (RF) spectrum with 100-kHz span at the fundamental frequency, and (c) RF spectrum with 1-GHz span of the laser output signal. The content in this figure was reproduced from my own publication [207]. © 2025 Optica Publishing Group (Creative Commons Attribution 4.0 License)

The output pulse duration was measured using an autocorrelator (pulseCheck NX150, APE). An autocorrelation (ACF) trace with a FWHM of 9.8 ps is presented in Figure 7.6(a), equivalent to an actual pulse duration of 7 ps based on the Gaussian-shape assumption. To de-chirp the output pulses, a grating-pair compressor, consisting of a pair of 900 line/mm transmission grating, was utilised. Figure 7.6(b) presents the ACF trace for the compressed pulse, achieving the shortest pulse duration of 539 fs. The time-bandwidth product (TBP) of the compressed pulse is 2 times larger than the Fourier transform limit. This might be attributed to some nonlinear chirp in the pulse that could be improved by managing the higher-order dispersion inside the cavity [64, 195].

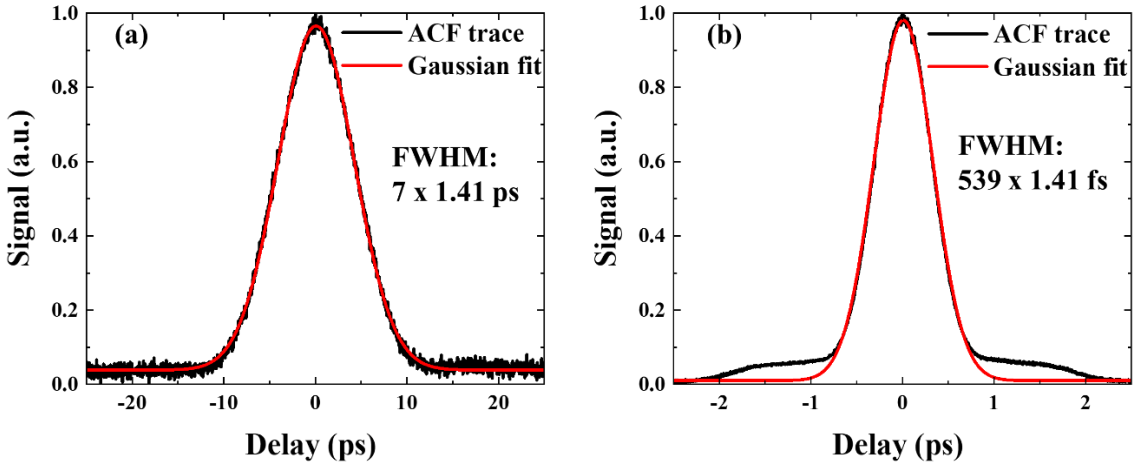

Figure 7.6 Autocorrelation trace of (a) the uncompressed pulses and (b) compressed pulses with the grating-pair compressor. The content in this figure was reproduced from my own publication [207]. © 2025 Optica Publishing Group (Creative Commons Attribution 4.0 License)

The single-pulse output properties were continuously monitored over 6 hours in a normal laboratory environment to observe laser stability. Figure 7.7(a) presents the output power stability of the ML operation, revealing stable output power with a small fluctuation of ±1.5%, which is attributed to pump power fluctuation. Figure 7.7(b) demonstrates a good repeatability of the output spectrum, acquired with 1-hour time intervals, over the experiment session.

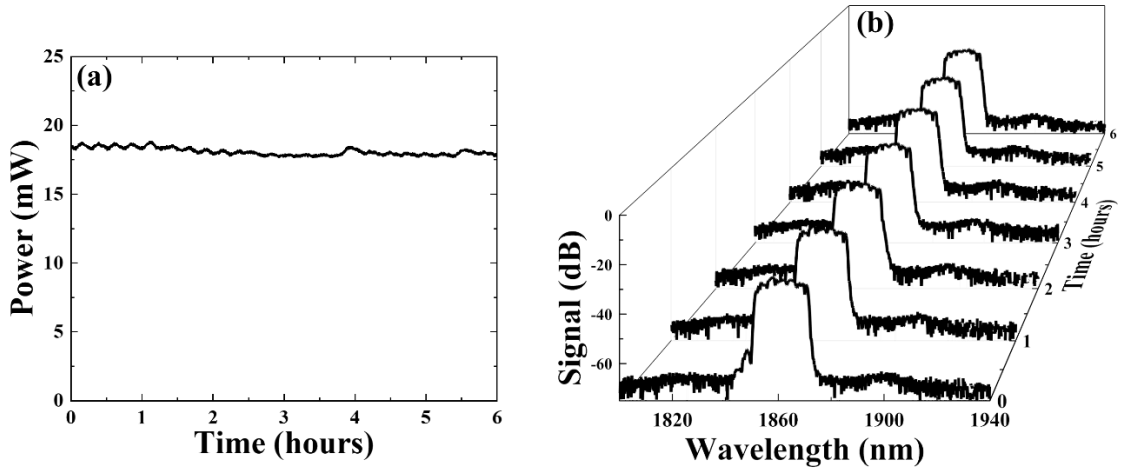

Figure 7.7 (a) Output power stability and (b) output spectra measured at 1-hour time intervals for 6 hours in normal laboratory environment. The content in this figure was reproduced from my own publication [207]. © 2025 Optica Publishing Group (Creative Commons Attribution 4.0 License)

7.3 Summary

In this chapter, I reported the demonstration of a nJ-pulse-energy, all-fibre, all-PM dissipative-soliton ML-TDFL, switched by a NALM-SA. The cavity generates ultrashort pulses at a central wavelength of 1860 nm with a pulse energy of 1.5 nJ and a compressed pulse duration of 539 fs. The ML operation in this cavity was enabled by a fibre-based SA that mitigated the technical challenges of material-based SA. I believe that this cavity design can be further optimised, especially for the self-start mechanism and ML operation at short wavelengths, which has great potential to support nonlinear biomedical imaging experiments.

Chapter 8 Conclusions and future works

8.1 Summary of the thesis

In summary, I have studied ML-TDFLs with different cavity designs, which generated ultrashort dissipative-soliton pulses within the SWIR region. These cavities have potential to support applications in deep tissue biomedical imaging experiments. I presented an all-fiberised SESAM-based non-PM ML-TDFL, generating a dissipative-soliton mode-locking at a central wavelength of 1875 nm. The cavity delivers output pulses with an energy exceeding 10 nJ and a compressed pulse duration of 548 fs. In order to achieve 10-nJ-energy pulses while maintaining ML operation at relatively short wavelengths (i.e., <1900 nm), the cavity needs to be carefully designed. This cavity holds high potential to enhance the overall simplicity of the laser system and supports the imaging applications. However, the wavelength choice was limited by SESAM availability.

To mitigate the limitations of wavelength in SESAMs, I explored new CNT-SAs, which were developed by our research collaborator at the Cambridge Graphene Centre, University of Cambridge. These CNT-SAs exhibit great potential for facilitating ML operation within the SWIR range, especially at short wavelengths toward 1800 nm. Additionally, the CNT-SAs demonstrated various wavelength-dependent transmissions and saturable absorption mechanisms based on their physical properties, which are beneficial for ML cavity design. By utilising the CNT-SA, I have demonstrated a compact, all-fiberised ML-TDFL operating at a central wavelength of 1847 nm with a compressed pulse duration of 381 fs. This cavity provides self-starting ML operation and has been employed as a seed laser in the MOFA system, delivered for biomedical imaging experiments.

I have presented, to the best of my knowledge, the first nJ- level all-PM dissipative-soliton ML-TDFL enabled by CNT-SA. To address the difficulty of splicing commercially available PM-DCF to PM-SMF, I incorporated a bridge-fibre splice method that reduces splice loss and ensures high PM performance. The cavity was carefully designed to feature a net normal dispersion and included a bandpass filter within the all-fiberised design, facilitating the dissipative-soliton operation. This cavity generates ultrashort pulses at a central wavelength of 1876 nm, a compressed pulse duration of 391 fs, and a pulse energy of 1.1 nJ. Due to the all-PM configuration, this cavity exhibited a ‘turnkey’ ML operation and demonstrated high tolerance to perturbations. The ML operation can be stably maintained for several hours in a laboratory environment. The findings from this experiment were published in *Optics and Laser technology* [197].

I have developed an all-PM ML-TDFL MOFA system that can be delivered to function as a reliable source in biomedical imaging experiments. A ML cavity was optimised to operate at a central

wavelength of 1840 nm with an uncompressed pulse duration of 4.3 ps. This cavity was implemented in the MOFA system to supply the seed signal for the CPA, where the output pulses were chirped and amplified to achieve tens of nJ pulse energies. Subsequently, the amplified pulses were de-chirped with a grating-pair compressor. At the laser output, the pulses have a compressed pulse duration of 493 fs with an average power of ~600 mW, equivalent to the pulse energy of ~40 nJ. This laser was delivered to the University of Nottingham, and utilised for biomedical imaging experiments, and since has exhibited good robustness and reliability without any major issues.

Finally, I have demonstrated an all-PM ML-TDFL using NALM-based SA. This fibre-based SA has great potential to resolve wavelength-dependent limitations and enhanced power handling within the cavity. When suitably designed, the cavity achieved 1.5-nJ-pulses with a central wavelength of 1860 nm and a compressed duration of 539 fs. This work has been reported in *Optics Express* [207]. This cavity design can be further developed to support shorter operating wavelengths, which should enhance the performance of deep-layer biomedical imaging. Table 8.1 presents an overview of key performances for ML-TDFLs developed in the experiments.

Table 8.1 Overview of key performances of mode-locked thulium-doped fibre lasers developed in the experiments

Fibre type	**SA**	**λ (nm)**	**E_p (nJ)**	**τ (fs)**	**RR (MHz)**	**Self-start with single pulse**	**High robustness**
Non-PM	SESAM	1875	10.3	548	18.44	Yes	No
Non-PM	CNT	1847	0.05	381	20.37	Yes	No
All-PM	CNT	1876	1.1	391	19.20	Yes	Yes
All-PM	CNT	1840	0.1*	493	15.15	Yes	Yes
All-PM	NALM	1860	1.5	539	15.55	No**	Yes

SA denotes the saturable absorber, λ represents the central wavelength, E_p is the pulse energy, τ is the compressed pulse duration, and RR is the repetition rate.

* Pulse energy was amplified to ~40 nJ at the laser output, i.e., after the MOFA and pulse compressor.

** The cavity generated a self-start with double-pulse ML operation.

8.2 Future work

8.2.1 SESAM-based all-PM ML-TDFL

In this thesis, I have demonstrated all-PM ML-TDFLs using different SAs. By utilising the CNT-SA, the 'turnkey' ML-TDFLs generated single-pulse ML operation once the ML threshold is satisfied. However, these CNT-SAs need to be specifically designed and fabricated by our research collaborator as they are not yet commercially available. Furthermore, the CNT-SA has limited capability to support several nJs pulse energies due to their damage threshold limits [76]. To mitigate this issue, power handling can potentially be improved by utilising fibre-based SAs, however, the challenge is a clear self-start mechanism that is turnkey, rather than reliant upon adjustment to initiate a single-pulse ML operation. These limitations could potentially be resolved by using SESAMs, which are capable of enabling 10-nJ-energy ML pulses, as I have demonstrated in Chapter 3. Additionally, the SESAM is a commercially available material that can be designed and fabricated by suppliers. The structure of the distributed Bragg reflector can be carefully adjusted to support desired wavelengths, while ensuring proper saturable absorption mechanism and spectral response. An idealised schematic of an all-PM ML-TDFL is presented in Figure 8.1. By incorporating with the bridge-fibre splice method (explained in Section 5.3.2), the connection between PM2000D and PM-SMF can be optimised.

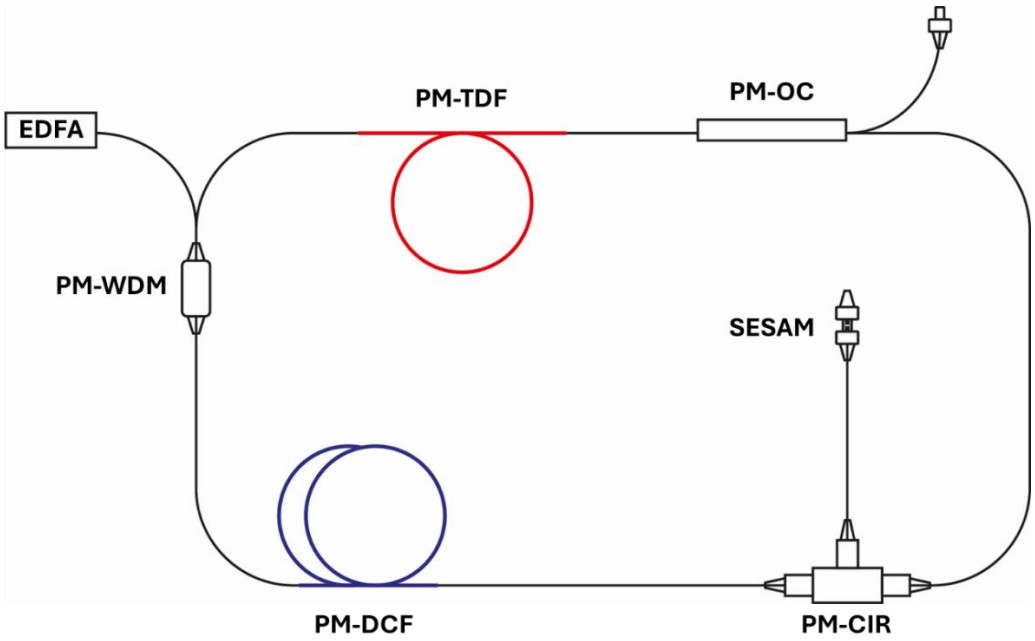

Figure 8.1 Idealised schematic of an all-polarisation maintaining (PM) mode-locked thulium-fibre laser with semiconductor saturable absorber mirror (SESAM). EDFA: erbium-doped master oscillator fibre amplifier; PM-WDM: PM-wavelength-division-multiplexer; PM-TDF: PM-thulium-doped fibre; PM-OC: PM-output coupler; and PM-CIR: PM circulator.

8.2.2 Short-wavelength all-PM ML-TDFL with combined filters

In order to improve the performance of biomedical imaging experiments, ultrafast pulses at wavelengths below 1800 nm are preferred. Generally, these wavelengths can be supported by the TDFs. However, the cavity needs to be carefully designed, including employing suitable SAs. In the thesis, I have utilised several types of SAs for supporting ML operation at short wavelengths. However, it is still challenging to achieve dissipative-soliton ML operation at wavelengths below 1800 nm. For a balanced dissipative effect, the cavity needs to be controlled to have a net normal dispersion with a proper bandpass filter. For instance, a dissipative-soliton ML-TDFL has been demonstrated at a central wavelength of 1746 nm with a compressed pulse duration of 370 fs, however, it had an output pulse energy of 0.2 nJ [19]. This cavity required a 1740-nm bandpass filter to confine the operating wavelength.

As demonstrated in this thesis, the Lyot filter can be used as a bandpass filter function with varying bandwidths, depending on the fibre lengths. However, the maximum transmission is controlled by the overall wavelength-dependent loss of the cavity. To facilitate a bandpass filter at wavelengths of interest, the LF can be combined with a fiberised 1800-nm short-pass filter to eliminate longer wavelengths. Figure 8.2 presents an idealised schematic of an all-PM ML-TDFL with the combined filters. By incorporating with a proper cavity optimisation, the all-fiberised dissipative-soliton ML-TDFL can be achieved at short wavelengths.

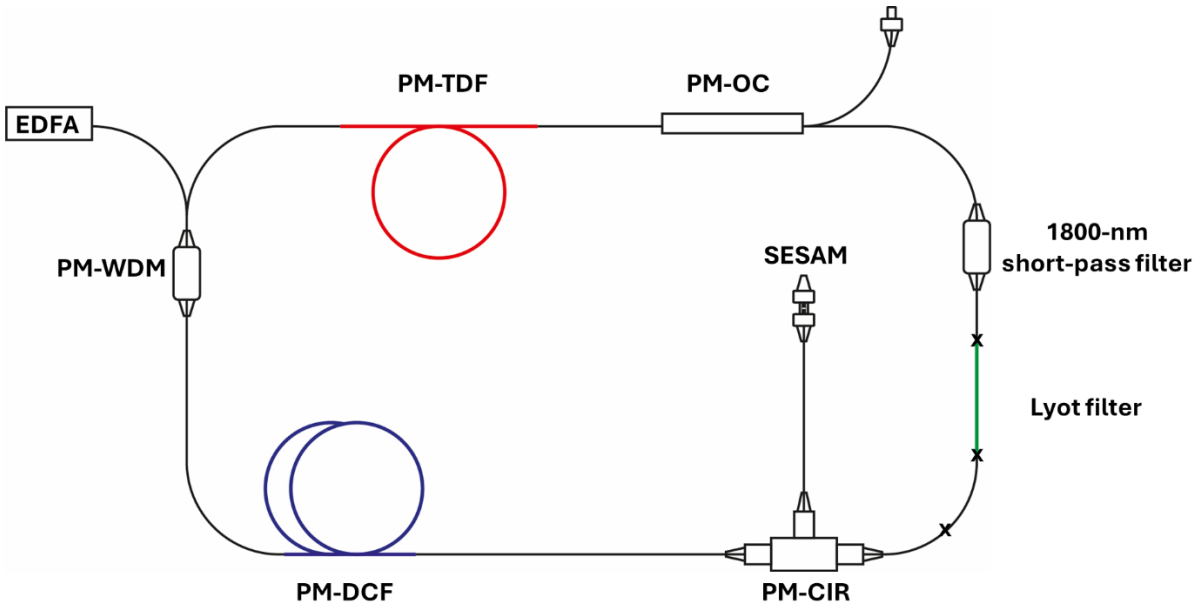

Figure 8.2 Idealised schematic of an all-polarisation maintaining (PM) mode-locked thulium-fibre laser with semiconductor saturable absorber mirror (SESAM). EDFA: erbium-doped master oscillator fibre amplifier; PM-WDM: PM-wavelength-division-multiplexer; PM-TDF: PM-thulium-doped fibre; PM-OC: PM-output coupler; and PM-CIR: PM circulator.

8.3 List of publications

Journals

- Duanyang Xu, Konstantinos N. Bourdakos, Anna Crisford, Peter Johnson, Ibrahim Abughazaleh, **Panuwat Srisamran**, Richard O. C. Oreffo, Sumeet Mahajan, David J. Richardson, Lin Xu, "All-fiberized 1840-nm femtosecond thulium fiber laser for label-free nonlinear microscopy", Biomedical Optics Express, 14**(9)**, 4520-4530 (2023).
  DOI: https://doi.org/10.1364/BOE.495879
- Matthew D. Gerard, Hiroki Cook, James A. Read, Ibrahim H. Abughazaleh, **Panuwat Srisamran**, Siddhi Chugh, Sijing Liang, Qiang Fu, Richard O. C. Oreffo, David J. Richardson, Sumeet Mahajan, and Lin Xu, "Single-cell high-precision ablation using nanosecond-pulsed thulium-doped fiber laser", Optical Engineering, 63**(8)**, 086102 (2024).
  DOI: https://doi.org/10.1117/1.OE.63.8.086102
- **Panuwat Srisamran**, Ibrahim Abughazaleh, Matthew D. Gerard, Duanyang Xu, Yongmin Jung, David J. Richardson, and Lin Xu, "Polarization-maintaining dissipative-soliton mode-locked thulium fiber laser with a nonlinear-amplifying-loop-mirror cavity operating at 1860 nm", Optics Express, 33**(8)**, 16880-16888, (2025).
  DOI: https://doi.org/10.1364/OE.559358
- **Panuwat Srisamran**, Ibrahim Abughazaleh, Matthew Gerard, Duanyang Xu, Yongmin Jung, Jing He, Jeremiah Marcellino, Boyang Mao, Andrea C. Ferrari, David Richardson, and Lin Xu, "Nanojoule-energy-level, polarization-maintaining, dissipative-soliton mode-locked thulium fiber laser at 1876 nm", Optics and Laser Technology, 189, 112978, (2025).
  DOI: https://doi.org/10.1016/j.optlastec.2025.112978

Conferences

- **Panuwat Srisamran**, Duanyang Xu, Ibrahim Abughazaleh, Matthew Gerard, Sijing Liang, David Richardson, and Lin Xu, "1875-nm high-energy mode-locked thulium fiber laser", in EPJ Web of Conference., 267, 02013 (2022).
  DOI: https://doi.org/10.1051/epjconf/202226702013
- L. Xu, D. Xu, K.N. Bourdakos, P.B. Johnson, A. Crisford, I. Abughazaleh, **P. Srisamran**, Q. Fu, S. Mahajan, D. J. Richardson, "1840-nm femtosecond thulium fiber laser system for label-free third-harmonic generation microscopy", in Conference on Lasers and Electro-Optics, Technical Digest Series (Optica Publishing Group, 2022).
  DOI: https://doi.org/10.1364/CLEO_AT.2022.JM4E.5

- Konstantinos N. Bourdakos, Lin Xu, Anna Crisford, Duanyang Xu, Ibrahim Abughazaleh, Peter B. Johnson, Hiroki Cook, **Panuwat Srisamran**, Richard O. C. Oreffo, David J. Richardson, Sumeet Mahajan, “Deep tissue imaging with multiphoton microscopy in the short-wavelength infrared windows”, Proc. SPIE 12333, Frontiers in Biophotonics and Imaging II, 123330E (11 January 2023).
  DOI: https://doi.org/10.1117/12.2647553
- Ibrahim Abughazaleh**,** **Panuwat Srisamran**, Matthew Gerard, Duanyang Xu, Yongmin Jung, David Richardson, and Lin Xu, “Pre-chirp managed thulium fiber amplifier for 1.8 μm ultrashort pulse generation,” in Conference on Lasers and Electro-Optics, Technical Digest Series (Optica Publishing Group, 2024).
  DOI: https://doi.org/10.1364/CLEO_AT.2024.JW2A.38
- Ibrahim H. Abughazaleh, **Panuwat Srisamran**, Duanyang Xu, Yongmin Jung, Richardson and Lin Xu, "Efficient pulse amplification and temporal compression in a 1790 nm femtosecond thulium fiber amplifier," in Conference on Lasers and Electro-Optics Pacific Rim, Technical Digest Series (Optica Publishing Group, 2024).
- **Panuwat Srisamran**, Ibrahim Abughazaleh, Matthew Gerard, Duanyang Xu, Yongmin Jung, Jing He, Jeremiah Marcellino, Boyang Mao, Andrea Ferrari, David Richardson, Lin Xu, “All-polarization-maintaining dissipative-soliton mode-locked thulium fiber laser at 1876 nm,” Proc. SPIE, PC12865G (2024).
  DOI: https://doi.org/10.1117/12.3002585
- Ibrahim H. Abughazaleh, **Panuwat Srisamran**, Matthew D. Gerard, Duanyang Xu, Yongmin Jung, Jing He, Jeremiah Marcellino, Boyang Mao, Andrea C. Ferrari, David J. Richardson, and Lin Xu, "Compact 1790-nm dissipative-soliton mode-locked thulium fiber laser," Proc. SPIE, PC1287501 (2024).
  DOI: https://doi.org/10.1117/12.3000615
- Matthew D. Gerard, Hiroki Cook, James A. Read, Ibrahim Abughazaleh, **Panuwat Srisamran**, Sijing Liang, Qiang Fu, Richard O. C. Oreffo, David J. Richardson, Sumeet Mahajan, and Lin Xu, "Single-cell high precision ablation using nanosecond-pulsed thulium-doped fiber laser", Proc. SPIE PC12840 (2024).
  DOI: https://doi.org/10.1117/12.3000343
- **Panuwat Srisamran**, Ibrahim Abughazaleh, Matthew D. Gerard, Duanyang Xu, Yongmin Jung, David Richardson, and Lin Xu, " Polarization-Maintaining Dissipative-Soliton Mode-Locked Thulium Fiber Laser with a NALM cavity," in Conference on Lasers and Electro-Optics (CLEO), 4263271 (2025).

References

1. D. C. Kirsch, S. Chen, R. Sidharthan, Y. Chen, S. Yoo, and M. Chernysheva, "Short-wave IR ultrafast fiber laser systems: Current challenges and prospective applications," J Appl Phys **128**(2020).
2. A. Parriaux, K. Hammani, and G. Millot, "Two-micron all-fibered dual-comb spectrometer based on electro-optic modulators and wavelength conversion," Commun Phys **1**(2018).
3. D. Grassani, E. Tagkoudi, H. R. Guo, C. Herkommer, F. Yang, T. J. Kippenberg, and C. S. Bres, "Mid infrared gas spectroscopy using efficient fiber laser driven photonic chip-based supercontinuum," Nat Commun **10**(2019).
4. J. P. Cariou, B. Augere, and M. Valla, "Laser source requirements for coherent lidars based on fiber technology," C R Phys **7**, 213-223 (2006).
5. S. Ishii, K. Mizutani, H. Fukuoka, T. Ishikawa, B. Philippe, H. Iwai, T. Aoki, T. Itabe, A. Sato, and K. Asai, "Coherent 2 μm differential absorption and wind lidar with conductively cooled laser and two-axis scanning device," Appl Opt **49**, 1809-1817 (2010).
6. K. Pankaj, C. Jeffrey, A. Faleh, A. S. Robert, W. Christina, S. Lawrence, K. Dennis, and C. R. Martin, "Atmospheric absorption spectroscopy using Tm:fiber sources around two microns," Proc. SPIE **7924**, 79240L (2011).
7. B. Voisiat, D. Gaponov, P. Gečys, L. Lavoute, M. Silva, A. Hideur, N. Ducros, and G. Račiukaitis, "Material processing with ultra-short pulse lasers working in 2 μm wavelength range," Proc. SPIE **9350**, 935014 (2015).
8. D. Flamm, M. Sailer, D. G. Grossmann, S. Rübling , D. Decker, C. Gaida, M. Blothe, D. Sutter, and S. Nolte, "Ultrafast laser micromachining using wavelengths from ~0.2 μm to ~2 μm," Proc. SPIE **13353**, 1335308 (2025).
9. C. W. Rudy, M. J. F. Digonnet, and R. L. Byer, "Advances in 2-μm Tm-doped mode-locked fiber lasers," Opt Fiber Technol **20**, 642-649 (2014).
10. N. G. Horton, K. Wang, D. Kobat, C. G. Clark, F. W. Wise, C. B. Schaffer, and C. Xu, "*In vivo* three-photon microscopy of subcortical structures within an intact mouse brain," Nat Photonics **7**(2013).
11. S. Golovynskyi, I. Golovynska, L. I. Stepanova, O. I. Datsenko, L. Liu, J. Qu, and T. Y. Ohulchanskyy, "Optical windows for head tissues in near-infrared and short-wave infrared regions: Approaching transcranial light applications," J Biophotonics **11**, e201800141 (2018).
12. D. Theisen, V. Ott, H.W. Bernd, V. Danicke, R. Keller, and R. Brinkmann, "Cw high power IR-laser at 2μm for minimally invasive surgery," Proc. SPIE **5142**, 96-100 (2003).

13. D. Theisen-Kunde, V. Ott, R. Brinkmann, and R. Keller, "Hemostatic properties of a new cw 2 μm laser scalpel for laparoscopic surgery," Proc. SPIE **5863**, 58630G (2005).
14. R. L. Blackmon, P. B. Irby, and N. M. Fried, "Comparison of holmium:YAG and thulium fiber laser lithotripsy: ablation thresholds, ablation rates, and retropulsion effects," J Biomed Opt **16**, 071403 (2011).
15. V. Andreeva, A. Vinarov, I. Yaroslavsky, A. Kovalenko, A. Vybornov, L. Rapoport, D. Enikeev, N. Sorokin, A. Dymov, D. Tsarichenko, P. Glybochko, N. Fried, O. Traxer, G. Altshuler, and V. Gapontsev, "Preclinical comparison of superpulse thulium fiber laser and a holmium:YAG laser for lithotripsy," World J Urol **38**, 497-503 (2020).
16. Y. Nomura, H. Murakoshi, and T. Fuji, "Short-wavelength, ultrafast thulium-doped fiber laser system for three-photon microscopy," OSA Continuum **3**, 1428-1435 (2020).
17. D. Xu, K. N. Bourdakos, A. Crisford, P. Johnson, I. Abughazaleh, P. Srisamran, R. O. C. Oreffo, S. Mahajan, D. J. Richardson, and L. Xu, "All-fiberized 1840-nm femtosecond thulium fiber laser for label-free nonlinear microscopy," Biomed Opt Express **14**, 4520-4530 (2023).
18. D. Creeden, B. R. Johnson, G. A. Rines, and S. D. Setzler, "High power resonant pumping of Tm-doped fiber amplifiers in core- and cladding-pumped configurations," Opt Express **22**, 29067-29080 (2014).
19. J. X. Chen, X. Y. Li, T. J. Li, Z. Y. Zhan, M. Liu, C. Li, A. P. Luo, P. Zhou, K. K. Y. Wong, W. C. Xu, and Z. C. Luo, "1.7-μm dissipative soliton Tm-doped fiber laser," Photon Res **9**, 873-878 (2021).
20. D. C. Kirsch, A. Bednyakova, P. Varak, P. Honzatko, B. Cadier, T. Robin, A. Fotiadi, P. Peterka, and M. Chernysheva, "Gain-controlled broadband tuneability in self-mode-locked thulium-doped fibre laser," Commun Phys **5**, 219 (2022).
21. R. I. Woodward, "Dispersion engineering of mode-locked fibre lasers," J Optics **20**(2018).
22. B. J. Ainslie and C. R. Day, "A review of single-mode fibers with modified dispersion characteristics," J Lightwave Technol **4**, 967-979 (1986).
23. L. E. Nelson, D. J. Jones, K. Tamura, H. A. Haus, and E. P. Ippen, "Ultrashort-pulse fiber ring lasers," Appl Physics B **65**, 277-294 (1997).
24. Y. Ososkov, A. Khegai, K. Riumkin, A. Mkrtchyan, Y. Gladush, D. Krasnikov, A. Nasibulin, M. Yashkov, A. Guryanov, and M. Melkumov, "All-PM fiber Tm-Doped laser with two fiber Lyot filters mode-locked by CNT," Photonics **9**(2022).
25. Z. Łaszczych, M. Krakowski, and G. Soboń, "Mode-locking dynamics in an All-PM figure-nine Tm-doped fiber laser," Appl Sci **12**(2022).
26. S. Peng, X. Liu, H. Y. Fu, and Q. Li, "Robust all-polarization-maintaining linear-cavity mode-locked Tm-Doped fiber laser," in *2023 Asia Communications and Photonics*

Conference/2023 International Photonics and Optoelectronics Meetings (ACP/POEM), 2023, 1-3.

27. J. F. Li, Z. X. Zhang, Z. Y. Sun, H. Y. Luo, Y. Liu, Z. J. Yan, C. B. Mou, L. Zhang, and S. K. Turitsyn, "All-fiber passively mode-locked Tm-doped NOLM-based oscillator operating at 2-μm in both soliton and noisy-pulse regimes," Opt Express **22**, 7875-7882 (2014).
28. G. Sobon, J. Sotor, I. Pasternak, A. Krajewska, W. Strupinski, and K. M. Abramski, "All-polarization maintaining, graphene-based femtosecond Tm-doped all-fiber laser," Opt Express **23**, 9339-9346 (2015).
29. A. E. Akosman and M. Y. Sander, "Low noise, mode-locked 253 MHz Tm/Ho fiber laser with core pumping at 790 nm," IEEE Photonics Technol Lett **28**, 1878-1881 (2016).
30. Q. Wang, J. Geng, Z. Jiang, T. Luo, and S. Jiang, "Mode-locked Tm–Ho-codoped fiber laser at 2.06 μm," IEEE Photonics Technol Lett **23**, 682-684 (2011).
31. H. Ahmad, R. Ramli, N. N. Ismail, S. N. Aidit, N. Yusoff, and M. Z. Samion, "Passively mode locked thulium and thulium/holmium doped fiber lasers using MXene Nb_2C coated microfiber," Sci Rep **11**(2021).
32. G. Sobon, A. Duzynska, M. Swiniarski, J. Judek, J. Sotor, and M. Zdrojek, "CNT-based saturable absorbers with scalable modulation depth for thulium-doped fiber lasers operating at 1.9 μm," Sci Rep **7**, 45491 (2017).
33. M. A. Chernysheva, A. A. Krylov, P. G. Kryukov, N. R. Arutyunyan, A. S. Pozharov, E. D. Obraztsova, and E. M. Dianov, "Thulium-doped mode-locked all-fiber laser based on NALM and carbon nanotube saturable absorber," Opt Express **20**, B124-130 (2012).
34. C. W. Rudy, K. E. Urbanek, M. J. F. Digonnet, and R. L. Byer, "Amplified 2-μm thulium-doped all-fiber mode-locked figure-eight laser," J Lightwave Technol **31**, 1809-1812 (2013).
35. M. Wang, M. Liu, J. Zhao, Y. Chen, D. Ouyang, and S. Ruan, "Stable femtosecond pulse generation relying on a simple NALM-based all PM Tm-doped fiber laser," Results Opt **9**, 100297 (2022).
36. Y. H. Chen, S. X. Chen, K. Liu, S. Raghuraman, Q. J. Wang, D. Y. Tang, and S. Yoo, "Toward high peak power ultrashort pulses using normal dispersion thulium fiber in all-fiber amplifier and compressor,"Proc. SPIE **11260**, 112600Z (2020).
37. M. Michalska and J. Swiderski, "All-fiber thulium-doped mode-locked fiber laser and amplifier based on nonlinear fiber loop mirror," Opt Laser Technol **118**, 121-125 (2019).
38. X. X. Liu, F. Li, X. C. Yu, S. Y. Zhang, and Y. L. Tang, "High-pulse-energy mode-locked and Q-switched large-mode-area thulium fiber laser," Opt Commun **457**(2020).
39. Z. X. Zhu, H. Zhang, M. M. Wang, R. L. Wei, Z. J. Zheng, P. G. Yan, S. C. Ruan, J. Z. Wang, T. Hasan, and Z. P. Sun, "Soliton mode-locked large-mode-area Tm-doped fiber oscillator," IEEE Photonics Technol Lett **32**, 117-120 (2020).

40. Y. Wang, Y. L. Tang, S. Yan, and J. Q. Xu, "High-power mode-locked 2 μm multimode fiber laser," Laser Phys Lett **15**(2018).
41. B. Sun, J. Q. Luo, Y. Zhang, Q. J. Wan, and X. Yu, "65-fs pulses at 2 μm in a compact Tm-doped all-fiber laser by dispersion and nonliearity management," IEEE Photonics Technol Lett **30**, 303-306 (2018).
42. N. Zhang, W. Q. Jiang, Y. F. Meng, and F. Q. Wang, "All-polarization-maintaining mode-locked thulium-doped femtosecond laser at 1.7 μm," Opt Continuum **2**, 1013-1019 (2023).
43. L. M. Yang, P. Wan, V. Protopopov, and J. Liu, "2 μm femtosecond fiber laser at low repetition rate and high pulse energy," Opt Express **20**, 5683-5688 (2012).
44. M. E. Fermann, A. Galvanauskas, G. Sucha, and D. Harter, "Fiber-lasers for ultrafast optics," Appl Phys B **65**, 259-275 (1997).
45. K. Tamura, E. P. Ippen, H. A. Haus, and L. E. Nelson, "77-fs pulse generation from a stretched-pulse mode-locked all-fiber ring laser," Opt Lett **18**, 1080-1082 (1993).
46. K. Tamura, L. E. Nelson, H. A. Haus, and E. P. Ippen, "Soliton versus nonsoliton operation of fiber ring lasers," Appl Phys Lett **64**, 149-151 (1994).
47. J. Sotor, J. Bogusławski, T. Martynkien, P. Mergo, A. Krajewska, A. Przewłoka, W. StrupiŃski, and G. SoboŃ, "All-polarization-maintaining, stretched-pulse Tm-doped fiber laser, mode-locked by a graphene saturable absorber," Opt Lett **42**, 1592-1595 (2017).
48. J. Sotor, G. Sobon, and K. M. Abramski, "Sub-130 fs mode-locked Er-doped fiber laser based on topological insulator," Opt Express **22**, 13244-13249 (2014).
49. J. W. Zhu, S. Y. Ge, J. Wang, W. W. Zhang, H. F. Ren, B. Yan, S. H. Mo, M. Qiu, K. Xia, P. L. Yang, S. X. Dai, S. C. Bai, P. P. Xu, and Q. H. Nie, "Systematic exploration and characterization on the influence of dispersion to pulse characteristics in Tm-doped NPE mode-locked fiber oscillator," Infrared Phys Techn **115**(2021).
50. Q. Wang, J. Geng, T. Luo, and S. Jiang, "2 μm mode-locked fiber lasers," Proc. SPIE **8237**, 82371N (2012).
51. D. S. Zhao, T. S. Wang, R. M. Liu, P. Lin, Q. Yuan, H. Xiong, P. D. Chen, and Y. W. Zhao, "Observation of sub-400fs, wavelength-switchable stretched pulse and bound-state pulse in Tm-doped fiber laser," Appl Optics **58**, 4956-4962 (2019).
52. F. Haxsen, D. Wandt, U. Morgner, J. Neumann, and D. Kracht, "Pulse characteristics of a passively mode-locked thulium fiber laser with positive and negative cavity dispersion," Opt Express **18**, 18981-18988 (2010).
53. R. Gumenyuk, I. Vartiainen, H. Tuovinen, and O. G. Okhotnikov, "Dissipative dispersion-managed soliton 2 μm thulium/holmium fiber laser," Opt Lett **36**, 609-611 (2011).

54. Y. Wang, S. U. Alam, E. D. Obraztsova, A. S. Pozharov, S. Y. Set, and S. Yamashita, "Generation of stretched pulses and dissipative solitons at 2 μm from an all-fiber mode-locked laser using carbon nanotube saturable absorbers," Opt Lett **41**, 3864-3867 (2016).
55. J. Z. Wang, X. Y. Liang, G. H. Hu, Z. J. Zheng, S. H. Lin, D. Q. Ouyang, X. Wu, P. G. Yan, S. C. Ruan, Z. P. Sun, and T. Hasan, "152 fs nanotube-mode-locked thulium-doped all-fiber laser," Sci Rep **6**(2016).
56. W. H. Renninger, A. Chong, and F. W. Wise, "Pulse shaping and evolution in normal-dispersion mode-locked fiber lasers," IEEE J Sel Top Quantum Electron **18**, 389-398 (2012).
57. F. W. Wise, A. Chong, and W. H. Renninger, "High-energy femtosecond fiber lasers based on pulse propagation at normal dispersion," Laser Photonics Rev **2**, 58-73 (2008).
58. B. Gao, R. H. Zhang, J. Y. Huo, C. Y. Ma, Y. Han, Q. R. Hou, F. Deng, G. Wu, and Y. Q. Ge, "Generation and categories of solitons in various mode-locked fiber lasers," Optik **220**(2020).
59. P. Grelu and N. Akhmediev, "Dissipative solitons for mode-locked lasers," Nat Photonics **6**, 84-92 (2012).
60. Y. Tang, A. Chong, and F. W. Wise, "Generation of 8 nJ pulses from a normal-dispersion thulium fiber laser," Opt Lett **40**, 2361-2364 (2015).
61. D. A. Gaponov, R. Dauliat, D. Darwich, T. Mansuryan, R. Jamier, S. Grimm, K. Schuster, and P. Roy, "High-power passively mode-locked dissipative soliton fiber laser featuring cladding-pumped non-CVD thulium-doped fiber," J Opt Soc Am B **32**, 1656-1659 (2015).
62. F. Haxsen, D. Wandt, U. Morgner, J. Neumann, and D. Kracht, "Monotonically chirped pulse evolution in an ultrashort pulse thulium-doped fiber laser," Opt Lett **37**, 1014-1016 (2012).
63. G. Sobon, J. Sotor, T. Martynkien, and K. M. Abramski, "Ultra-broadband dissipative soliton and noise-like pulse generation from a normal dispersion mode-locked Tm-doped all-fiber laser," Opt Express **24**, 6156-6161 (2016).
64. Y. Li, L. Wang, Y. Kang, X. Guo, and L. Tong, "Microfiber-enabled dissipative soliton fiber laser at 2 μm," Opt Lett **43**, 6105-6108 (2018).
65. C. Y. Huang, C. Wang, W. Shang, N. Yang, Y. L. Tang, and J. Q. Xu, "Developing high energy dissipative soliton fiber lasers at 2 micron," Sci Rep **5**(2015).
66. Y. Zhao, D. Zhao, R. Liu, W. Ma, and T. Wang, "Switchable generation of a sub-200 fs dissipative soliton and a noise-like pulse in a normal-dispersion Tm-doped mode-locked fiber laser," Appl Opt **59**, 3575-3581 (2020).
67. M. Tokurakawa, H. Sagara, and H. Tunnermann, "All-normal-dispersion nonlinear polarization rotation mode-locked Tm:ZBLAN fiber laser," Opt Express **27**, 19530-19535 (2019).

68. A. Vaupel, N. Bodnar, B. Webb, L. Shah, and M. Richardson, "Concepts, performance review, and prospects of table-top, few-cycle optical parametric chirped-pulse amplification," Opt Eng **53**(2014).
69. P. J. Delfyett, D. Mandridis, M. U. Piracha, D. Nguyen, K. Kim, and S. Lee, "Chirped pulse laser sources and applications," Prog Quant Electron **36**, 475-540 (2012).
70. J. Limpert, T. Clausnitzer, A. Liem, T. Schreiber, H. J. Fuchs, H. Zellmer, E. B. Kley, and A. Tünnermann, "High-average-power femtosecond fiber chirped-pulse amplification system," Opt Lett **28**, 1984-1986 (2003).
71. D. Gaponov, L. Lavoute, S. Février, A. Hideur, and N. Ducros, "2μm all-fiber dissipative soliton master oscillator power amplifier," Proc. SPIE **9728**, 972834 (2016).
72. Z. Ren, Q. Fu, L. Xu, J. H. V. Price, S. U. Alam, and D. J. Richardson, "Compact, high repetition rate, 4.2 MW peak power, 1925 nm, thulium-doped fiber chirped-pulse amplification system with dissipative soliton seed laser," Opt Express **27**, 36741-36749 (2019).
73. F. Z. Tan, H. X. Shi, P. Wang, J. Liu, and P. Wang, "Chirped pulse amplification of a dissipative soliton thulium-doped fiber laser," Proc. SPIE **9728**, 97280Y (2016).
74. C. Gaida, M. Gebhardt, F. Stutzki, C. Jauregui, J. Limpert, and A. Tunnermann, "Thulium-doped fiber chirped-pulse amplification system with 2 GW of peak power," Opt Lett **41**, 4130-4133 (2016).
75. U. Keller, "Recent developments in compact ultrafast lasers," Nature **424**, 831-838 (2003).
76. K. Y. Lau, X. F. Liu, and J. R. Qiu, "A comparison for saturable absorbers: carbon nanotube versus graphene," Adv Photon Res **3**(2022).
77. S. Yamashita and S. Y. Set, "Advances and challenges of mode-locked fiber lasers," Opt Commun **578**(2025).
78. K. Y. Lau and D. Hou, "Recent research and advances of material-based saturable absorber in mode-locked fiber laser," Opt Laser Technol **137**(2021).
79. U. Keller, K. J. Weingarten, F. X. Kartner, D. Kopf, B. Braun, I. D. Jung, R. Fluck, C. Honninger, N. Matuschek, and J. A. derAu, "Semiconductor saturable absorber mirrors (SESAM's) for femtosecond to nanosecond pulse generation in solid-state lasers," IEEE J Sel Top Quant **2**, 435-453 (1996).
80. S. Y. Ryu, K. S. Kim, J. Kim, and S. Kim, "Degradation of optical properties of a film-type single-wall carbon nanotubes saturable absorber (SWNT-SA) with an Er-doped all-fiber laser," Opt Express **20**, 12966-12974 (2012).
81. S. M. Kobtsev, "Artificial saturable absorbers for ultrafast fibre lasers," Opt Fiber Technol **68**(2022).

82. W. Hänsel, H. Hoogland, M. Giunta, S. Schmid, T. Steinmetz, R. Doubek, P. Mayer, S. Dobner, C. Cleff, M. Fischer, and R. Holzwarth, "All polarization-maintaining fiber laser architecture for robust femtosecond pulse generation," Appl Phys B **123**(2017).
83. D. Duan, J. Wang, Y. Wu, J. D. Ma, and Q. H. Mao, "Approach to high pulse energy emission of the self-starting mode-locked figure-9 fiber laser," Opt Express **28**, 33603-33613 (2020).
84. M. C. Li, L. H. Liu, T. P. Xiao, J. J. Xue, L. T. Liang, H. L. Wang, and M. Xiong, "Single-polarization polarization maintaining optical fiber with large stress birefringence and high homogeneity," Appl Phys Lett **89**(2006).
85. J. Noda, K. Okamoto, and Y. Sasaki, "Polarization-maintaining fibers and their applications," J Lightwave Technol **4**, 1071-1089 (1986).
86. N. Kuse, J. Jiang, C. C. Lee, T. R. Schibli, and M. E. Fermann, "All polarization-maintaining Er fiber-based optical frequency combs with nonlinear amplifying loop mirror," Opt Express **24**, 3095-3102 (2016).
87. E. Baumann, F. R. Giorgetta, J. W. Nicholson, W. C. Swann, I. Coddington, and N. R. Newbury, "High-performance, vibration-immune, fiber-laser frequency comb," Opt Lett **34**, 638-640 (2009).
88. L. Zhang, J. Q. Zhou, Z. K. Wang, X. J. Gu, and Y. Feng, "SESAM mode-locked, environmentally stable, and compact dissipative soliton fiber laser," IEEE Photonics Technol Lett **26**, 1314-1316 (2014).
89. K. Zhao, W. Yan, M. L. Liu, L. S. Wang, H. X. Li, M. S. Zhang, Z. Q. Jia, R. Z. Zhai, and M. Z. Liu, "Tunable ytterbium fiber laser mode-locked with a nonlinear amplifying loop mirror," Opt Laser Technol **148**(2022).
90. Y. J. Pan, Q. Lu, T. Ma, D. Zhang, H. Pan, and L. B. Liang, "All-polarization-maintaining Figure-9 erbium-doped mode-locked fiber laser based on a bidirectionally pumped weak asymmetric NALM," Appl Optics **63**, 8034-8043 (2024).
91. Y. F. Duan, J. Q. Zhou, L. K. Wang, Y. F. Huang, Y. L. Li, Y. Feng, L. Liu, and T. Li, "Dissipative solitons in a compact Er-doped all-fiber figure-of-9 laser," Opt Fiber Technol **64**(2021).
92. C. Huang, Q. Wang, J. Geng, T. Luo, R. Liang, and S. Jiang, "All-PM dissipative soliton fiber laser at 2-Micron," in *Laser Congress 2017 (ASSL, LAC)*, OSA Technical Digest (online) (Optica Publishing Group, 2017), JTu2A.22.
93. G. A. Cervantes, "The basics of x-rays," in *Technical Fundamentals of Radiology and CT,* (IOP Publishing, 2016), pp. 1-1-1-5.
94. G. A. Cervantes, "Radiographic quality," in *Technical Fundamentals of Radiology and CT,* (IOP Publishing, 2016), pp. 2-1-2-11.

95. T. Kagawa, S. Yoshida, T. Shiraishi, M. Hashimoto, D. Inadomi, M. Sato, T. Tsuzuki, K. Miwa, and K. Yuasa, "Basic principles of magnetic resonance imaging for beginner oral and maxillofacial radiologists," Oral Radiol **33**, 92-100 (2017).

96. B. Ihnatsenka and A. P. Boezaart, "Ultrasound: Basic understanding and learning the language," Int J Shoulder Surg **4**, 55-62 (2010).

97. G. Parvathy, A. Nazir, Z. Morani, and A. Nazir, "Unveiling the power of imaging techniques: comparing high-resolution ultrasound and functional MR neurography in peripheral nervous system pathology: a short communication," Ann Med Surg **85**, 5834-5837 (2023).

98. W. R. Zipfel, R. M. Williams, and W. W. Webb, "Nonlinear magic: multiphoton microscopy in the biosciences," Nat Biotechnol **21**, 1368-1376 (2003).

99. W. Denk, J. H. Strickler, and W. W. Webb, "Two-photon laser scanning fluorescence microscopy," Science **248**, 73-76 (1990).

100. C. Lefort, "A review of biomedical multiphoton microscopy and its laser sources," J Phys D Appl Phys **50**(2017).

101. D. Kobat, N. G. Horton, and C. Xu, "In vivo two-photon microscopy to 1.6-mm depth in mouse cortex," J Biomed Opt **16**(2011).

102. E. B. Brown, R. B. Campbell, Y. Tsuzuki, L. Xu, P. Carmeliet, D. Fukumura, and R. K. Jain, "*In vivo* measurement of gene expression, angiogenesis and physiological function in tumors using multiphoton laser scanning microscopy," Nat Med **7**, 864-868 (2001).

103. T. G. Oertner, "Functional imaging of single synapses in brain slices," Experimental Physiology **87**, 733-736 (2002).

104. M. J. Miller, S. H. Wei, I. Parker, and M. D. Cahalan, "Two-photon imaging of lymphocyte motility and antigen response in intact lymph node," Science **296**, 1869-1873 (2002).

105. D. M. McDonald and P. L. Choyke, "Imaging of angiogenesis: from microscope to clinic," Nat Med **9**, 713-725 (2003).

106. A. Majewska, A. Tashiro, and R. Yuste, "Regulation of spine calcium dynamics by rapid spine motility," J Neurosci **20**, 8262-8268 (2000).

107. M. Balu, T. Baldacchini, J. Carter, T. B. Krasieva, R. Zadoyan, and B. J. Tromberg, "Effect of excitation wavelength on penetration depth in nonlinear optical microscopy of turbid media," J Biomed Opt **14**(2009).

108. D. Kobat, M. E. Durst, N. Nishimura, A. W. Wong, C. B. Schaffer, and C. Xu, "Deep tissue multiphoton microscopy using longer wavelength excitation," Opt Express **17**, 13354-13364 (2009).

109. K. Wang, Y. Pan, S. Tong, H. P. Liang, and P. Qiu, "Deep-skin multiphoton microscopy of lymphatic vessels excited at the 1700-nm window in vivo," Biomed Opt Express **12**, 6474-6484 (2021).

110. K. Wang, N. G. Horton, K. Charan, and C. Xu, "Advanced fiber soliton sources for nonlinear deep tissue imaging in biophotonics," IEEE J Sel Top Quant **20**(2014).
111. R. H. Wilson, K. P. Nadeau, F. B. Jaworski, B. J. Tromberg, and A. J. Durkin, "Review of short-wave infrared spectroscopy and imaging methods for biological tissue characterization," J Biomed Opt **20**, 030901 (2015).
112. J. Aubrecht, P. Peterka, P. Honzatko, O. Moravec, M. Kamradek, and I. Kasik, "Broadband thulium-doped fiber ASE source," Opt Lett **45**, 2164-2167 (2020).
113. S. X. Chen, Y. H. Chen, K. Liu, R. Sidharthan, H. Z. Li, C. J. Chang, Q. J. Wang, D. Y. Tang, and S. Yoo, "W-type normal dispersion thulium-doped fiber-based high-energy all-fiber femtosecond laser at 1.7 μm," Opt Lett **46**, 3637-3640 (2021).
114. R. Lingle, D. W. Peckham, A. McCurdy, and J. Kim, "Chapter 2 - Light-Guiding Fundamentals and Fiber Design," in *Specialty Optical Fibers Handbook*, A. Méndez and T. F. Morse, eds. (Academic Press, Burlington, 2007), pp. 19-68.
115. J. Kobelke, K. Schuster, J. Bierlich, S. Unger, A. Schwuchow, T. Elsman, J. Dellith, C. Aichele, R. Fatobene Ando, and H. Bartelt, "Germania and alumina dopant diffusion and viscous flow effects at preparation of doped optical fibers," Adv Electr Electron **15**, 101-106 (2017).
116. B. Dussardier and W. Blanc, "Alternative dopants for silica fibre amplifiers," ICTON 2007: Proceedings of the 9th International Conference on Transparent Optical Networks, Vol 2, 313-316 (2007).
117. S. B. Poole, D. N. Payne, R. J. Mears, M. E. Fermann, and R. I. Laming, "Fabrication and characterization of low-loss optical fibers containing rare-earth ions," J Lightwave Technol **4**, 870-876 (1986).
118. M. Ohashi, K. Shiraki, and K. Tajima, "Optical loss property of silica-based single-mode fibers," J Lightwave Technol **10**, 539-543 (1992).
119. S. C. Rashleigh, "Origins and control of polarization effects in single-mode fibers," J Opt Soc Am **72**, 1808-1808 (1982).
120. C. Emslie, "Chapter 8 - Polarization Maintaining Fibers," in *Specialty Optical Fibers Handbook*, A. Méndez and T. F. Morse, eds. (Academic Press, Burlington, 2007), pp. 243-277.
121. B. Pedersen, A. Bjarklev, J. H. Povlsen, K. Dybdal, and C. C. Larsen, "The design of erbium-doped fiber amplifiers," J Lightwave Technol **9**, 1105-1112 (1991).
122. J. F. Philipps, T. Töpfer, H. Ebendorff-Heidepriem, D. Ehrt, and R. Sauerbrey, "Energy transfer and upconversion in erbium-ytterbium-doped fluoride phosphate glasses," Appl Phys B **74**, 233-236 (2002).

123. Q. Han, W. C. Yan, Y. Z. Yao, Y. F. Chen, and T. G. Liu, "Optimal design of Er/Yb co-doped fiber amplifiers with an Yb-band fiber Bragg grating," Photon Res **4**, 53-56 (2016).

124. P. G. R. Hernandez, S. Pidishety, and J. Nilsson, "Quenching dynamics in highly doped erbium fiber core-pumping, amplifier configuration," AIP Adv **15**(2025).

125. S. D. Jackson and T. A. King, "Theoretical modeling of Tm-doped silica fiber lasers," J Lightwave Technol **17**, 948-956 (1999).

126. S. D. Jackson, "The spectroscopic and energy transfer characteristics of the rare earth ions used for silicate glass fibre lasers operating in the shortwave infrared," Laser Photonics Rev **3**, 466-482 (2009).

127. F. Roy, F. Leplingard, L. Lorcy, A. Sauze, P. Baniel, and D. Bayart, "48% power conversion efficiency in a single-pump gain-shifted thulium-doped fiber amplifier," *OFC 2001. Optical Fiber Communication Conference and Exhibit. Technical Digest,* pp. PD2 (1-2) (2001).

128. A. Sincore, J. D. Bradford, J. Cook, L. Shah, and M. C. Richardson, "High average power thulium-doped silica fiber lasers: Review of systems and concepts," IEEE J Sel Top Quant **24**(2018).

129. G. P. Frith, B. Samson, A. Carter, J. Farroni, and K. Tankala, "High efficiency 110 W monolithic FBG tuned 2 μm fiber laser," in *2007 European Conference on Lasers and Electro-Optics and the International Quantum Electronics Conference*, 2007, 1-1.

130. S. D. Jackson, "Cross relaxation and energy transfer upconversion processes relevant to the functioning of 2 μm Tm3+-doped silica fibre lasers," Opt Commun **230**, 197-203 (2004).

131. Y. Jeong, P. Dupriez, J. K. Sahu, J. Nilsson, D. Y. Shen, W. A. Clarkson, and S. D. Jackson, "Power scaling of 2 μm ytterbium-sensitised thulium-doped silica fibre laser diode-pumped at 975 nm," Electron Lett **41**, 173-174 (2005).

132. Y. H. Tsang, D. J. Coleman, and T. A. King, "High power 1.9 μm Tm3+-silica fibre laser pumped at 1.09 μm by a Yb3+-silica fibre laser," Opt Commun **231**, 357-364 (2004).

133. D. Y. Shen, J. K. Sahu, and W. A. Clarkson, "High-power widely tunable Tm: fibre lasers pumped by an Er, Yb co-doped fibre laser at 1.6 μm," Opt Express **14**, 6084-6090 (2006).

134. T. Yamamoto, Y. Miyajima, and T. Komukai, "1.9-μm Tm-Doped Silica Fiber Laser-Pumped at 1.57-μm," Electron Lett **30**, 220-221 (1994).

135. G. Sobon, P. Kaczmarek, and K. M. Abramski, "Erbium-ytterbium co-doped fiber amplifier operating at 1550 nm with stimulated lasing at 1064 nm," Opt Commun **285**, 1929-1933 (2012).

136. G. Agrawal, "Chapter 2 - Pulse Propagation in Fibers," in *Nonlinear Fiber Optics (Fifth Edition)*, G. Agrawal, ed. (Academic Press, Boston, 2013), pp. 27-56.

137. G. Agrawal, "Chapter 3 - Group-Velocity Dispersion," in *Nonlinear Fiber Optics (Fifth Edition)*, G. Agrawal, ed. (Academic Press, Boston, 2013), pp. 57-85.
138. G. Agrawal, "Chapter 4 - Self-Phase Modulation," in *Nonlinear Fiber Optics (Fifth Edition)*, G. Agrawal, ed. (Academic Press, Boston, 2013), pp. 87-128.
139. S. Kharitonov, A. Billat, and C. S. Bres, "Kerr nonlinearity and dispersion characterization of core-pumped thulium-doped fiber at 2 μm," Opt Lett **41**, 3173-3176 (2016).
140. G. P. Agrawal, "Chapter 5 - Optical Solitons," in *Nonlinear Fiber Optics (Fifth Edition)*, G. Agrawal, ed. (Academic Press, Boston, 2013), pp. 129-191.
141. H. A. Haus, "Mode-locking of lasers," IEEE J Sel Top Quant **6**, 1173-1185 (2000).
142. U. Keller, "Active Modelocking," in *Ultrafast Lasers: A Comprehensive Introduction to Fundamental Principles with Practical Applications*, U. Keller, ed. (Springer International Publishing, Cham, 2021), pp. 225-277.
143. U. Keller, "Passive Modelocking," in *Ultrafast Lasers: A Comprehensive Introduction to Fundamental Principles with Practical Applications*, U. Keller, ed. (Springer International Publishing, Cham, 2021), pp. 419-546.
144. M. Nakazawa, K. Suzuki, and H. A. Haus, "Modulational instability oscillation in nonlinear dispersive ring cavity," Phys Rev A **38**, 5193-5196 (1988).
145. U. Keller, "Saturable Absorbers for Solid-State Lasers," in *Ultrafast Lasers: A Comprehensive Introduction to Fundamental Principles with Practical Applications*, U. Keller, ed. (Springer International Publishing, Cham, 2021), pp. 279-371.
146. S. Suomalainen, M. Guina, T. Hakulinen, O. G. Okhotnikov, T. G. Euser, and S. Marcinkevicius, "1 μm saturable absorber with recovery time reduced by lattice mismatch," Appl Phys Lett **89**(2006).
147. H. D. Xia, H. P. Li, X. X. Zhang, S. J. Zhang, X. G. Tang, and Y. Liu, "Characteristics of dissipative solitons in an all-fiber thulium-doped fiber ring laser," Opt Eng **52**(2013).
148. I. Armas-Rivera, L. A. Rodriguez-Morales, M. Durán-Sánchez, M. Avazpour, A. Carrascosa, E. Silvestre, E. A. Kuzin, M. V. Andres, and B. Ibarra-Escamilla, "Wide wavelength-tunable passive mode-locked Erbium-doped fiber laser with a SESAM," Opt Laser Technol **134**(2021).
149. X. Cao, F. Li, D. D. Song, Y. S. Wang, Q. L. Li, H. L. Zhao, W. Zhao, W. L. Wen, and J. H. Si, "Environmentally stable all-fiber femtosecond laser for industrial application based on a SESAM mode-locked ytterbium-doped laser," Microw Opt Techn Let **66**(2024).
150. L. A. Vazquez-Zuniga and Y. Jeong, "Wavelength-tunable, passively mode-locked erbium-doped fiber master-oscillator incorporating a semiconductor saturable absorber mirror," J Opt Soc Korea **17**, 117-129 (2013).
151. Batop optoelectronics, https://www.batop.de/information/SAM_infos.html, 2022.

152. Batop optoelectronics, https://www.batop.de/products/saturable-absorber/saturable-absorber-mirror/data-sheet/saturable-absorber-mirror-2000nm/saturable-absorber-mirror-SAM-1920-36-10ps.pdf, 2025.
153. S. Y. Set, H. Yaguchi, Y. Tanaka, and M. Jablonski, "Laser mode locking using a saturable absorber incorporating carbon nanotubes," J Lightwave Technol **22**, 51-56 (2004).
154. H. Y. Guo, L. Hou, Y. G. Wang, J. Sun, Q. M. Lin, Y. Bai, and J. T. Bai, "Tunable ytterbium-doped mode-locked fiber laser based on single-walled carbon nanotubes," J Lightwave Technol **37**, 2370-2374 (2019).
155. T. R. Schibli, E. R. Thoen, F. X. Kärtner, and E. P. Ippen, "Suppression of Q-switched mode locking and break-up into multiple pulses by inverse saturable absorption," Applied Physics B **70**, S41-S49 (2000).
156. V. J. Matsas, T. P. Newson, and M. N. Zervas, "Self-starting passively mode-locked fiber ring laser exploiting nonlinear polarization switching," Opt Commun **92**, 61-66 (1992).
157. M. Olivier, M. D. Gagnon, and J. Habel, "Automation of mode locking in a nonlinear polarization rotation fiber laser through output polarization measurements," J Vis Exp (2016).
158. D. Stoliarov, I. Kudelin, A. Koviarov, and E. Rafailov, "Transient dynamics in mode-locked all-PM Er-doped fiber laser with NALM," Opt Commun **547**(2023).
159. X. Y. Yang, J. N. Tao, C. Y. Lv, C. H. Fu, B. L. Lu, and J. T. Bai, "All-normal dispersion widely tunable dual-wavelength mode-locked fiber laser based on NALM," Opt Express **31**, 37537-37548 (2023).
160. M. E. Fermann, F. Haberl, M. Hofer, and H. Hochreiter, "Nonlinear amplifying loop mirror," Opt Lett **15**, 752-754 (1990).
161. Z. M. Zhang, W. Wei, Z. L. Li, L. Q. Tang, L. Ding, X. L. Zeng, and Y. G. Li, "All-fiber vortex laser based on a nonlinear amplifying loop mirror and a coupler," IEEE Photonics Technol Lett **31**, 1049-1051 (2019).
162. B. Lyot, "Optical apparatus with wide field using interference of polarized light," C R Acad Sci Paris **197**, 1593 (1933).
163. X. Sun, Y. Zhu, L. Jin, S. Yamashita, and S. Y. Set, "Polarization-maintaining all-fiber tunable mode-locked laser based on a thermally controlled Lyot filter," Opt Lett **47**, 4913-4916 (2022).
164. S. Kobtsev, "Birefringent filters in fiber systems," J Opt Soc Am B **42**, 489-494 (2025).
165. J. Ye, J. M. Xu, J. X. Song, H. Y. Xu, H. S. Wu, H. W. Zhang, J. Y. Leng, and P. Zhou, "Power scalability of linearly polarized random fiber laser through polarization-rotation-based Raman gain manipulation," Opt Express **26**, 22894-22903 (2018).

166. Z. J. Yan, C. B. Mou, H. S. Wang, K. M. Zhou, Y. S. Wang, W. Zhao, and L. Zhang, "All-fiber polarization interference filters based on 45 degrees-tilted fiber gratings," Opt Lett **37**, 353-355 (2012).
167. S. T. Xu, A. Turnali, and M. Y. Sander, "Group-velocity-locked vector solitons and dissipative solitons in a single fiber laser with net-anomalous dispersion," Sci Rep **12**(2022).
168. Y. S. Fedotov, S. M. Kobtsev, R. N. Arif, A. G. Rozhin, C. Mou, and S. K. Turitsyn, "Spectrum-, pulsewidth-, and wavelength-switchable all-fiber mode-locked Yb laser with fiber based birefringent filter," Opt Express **20**, 17797-17805 (2012).
169. L. F. Mollenauer and R. H. Stolen, "The soliton laser," Opt Lett **9**, 13-15 (1984).
170. R. Paschotta, "Solitons", https://www.rp-photonics.com/solitons.html, 2022.
171. L. F. Mollenauer, J. P. Gordon, and M. N. Islam, "Soliton propagation in long fibers with periodically compensated loss," IEEE J Quantum Elect **22**, 157-173 (1986).
172. N. J. Smith, K. J. Blow, and I. Andonovic, "Sideband generation through perturbations to the average soliton model," J Lightwave Technol **10**, 1329-1333 (1992).
173. U. Keller, "Ultrafast solid-state laser oscillators: a success story for the last 20 years with no end in sight," Appl Phys B **100**, 15-28 (2010).
174. S. K. Turitsyn, B. G. Bale, and M. P. Fedoruk, "Dispersion-managed solitons in fibre systems and lasers," Phys Rep **521**, 135-203 (2012).
175. A. Chong, W. H. Renninger, and F. W. Wise, "Properties of normal-dispersion femtosecond fiber lasers," J Opt Soc Am B **25**, 140-148 (2008).
176. A. Chong, J. Buckley, W. Renninger, and F. Wise, "All-normal-dispersion femtosecond fiber laser," Opt Express **14**, 10095-10100 (2006).
177. L. M. Zhao, D. Y. Tang, T. H. Cheng, and C. Lu, "Gain-guided solitons in dispersion-managed fiber lasers with large net cavity dispersion," Opt Lett **31**, 2957-2959 (2006).
178. B. Proctor, E. Westwig, and F. Wise, "Characterization of a Kerr-Lens mode-locked Ti-sapphire laser with positive group-velocity dispersion," Opt Lett **18**, 1654-1656 (1993).
179. W. H. Renninger and F. W. Wise, "Fundamental limits to mode-locked lasers: Toward terawatt peak powers," IEEE J Sel Top Quant **21**(2015).
180. D. Strickland and G. Mourou, "Compression of amplified chirped optical pulses," Opt Commun **56**, 219-221 (1985).
181. P. Maine, D. Strickland, P. Bado, M. Pessot, and G. Mourou, "Generation of ultrahigh peak power pulses by chirped pulse amplification," IEEE J Quantum Elect **24**, 398-403 (1988).
182. M. D. Perry, D. Pennington, B. C. Stuart, G. Tietbohl, J. A. Britten, C. Brown, S. Herman, B. Golick, M. Kartz, J. Miller, H. T. Powell, M. Vergino, and V. Yanovsky, "Petawatt laser pulses," Opt Lett **24**, 160-162 (1999).

183. G. A. Mourou, T. Tajima, and S. V. Bulanov, "Optics in the relativistic regime," Rev Mod Phys **78**, 309-371 (2006).

184. T. Eidam, J. Rothhardt, F. Stutzki, F. Jansen, S. Hädrich, H. Carstens, C. Jauregui, J. Limpert, and A. Tünnermann, "Fiber chirped-pulse amplification system emitting 3.8 GW peak power," Opt Express **19**, 255-260 (2011).

185. F. Li, W. Zhao, Y. S. Wang, N. Wang, Q. L. Li, Y. Yang, and W. L. Wen, "A large dispersion-managed monolithic all-fiber chirped pulse amplification system for high-energy femtosecond laser generation," Opt Laser Technol **147**(2022).

186. E. Treacy, "Optical pulse compression with diffraction gratings," IEEE J Quantum Elect **5**, 454-458 (1969).

187. C. Saraceno, "White paper: Pulse stretching and compressing using grating pairs," (Ibsen Photonics, 2017). https://ibsen.com/wp-content/uploads/White-paper-Pulse-stretching-and-compressing-using-grating-pairs_v1.pdf

188. Y. Meng, Y. Li, Y. Xu, and F. Wang, "Carbon nanotube mode-locked thulium fiber laser with 200 nm tuning range," Sci Rep **7**, 45109 (2017).

189. W. H. Renninger, A. Chong, and F. W. Wise, "Area theorem and energy quantization for dissipative optical solitons," J Opt Soc Am B **27**, 1978-1982 (2010).

190. B. F. Zhang, D. X. Cao, Z. X. Jiao, and B. Wang, "All-fiberized polarized mode-locked thulium-doped fibre laser," Laser Phys Lett **12**(2015).

191. K. Watanabe, Y. Zhou, Y. Sakakibara, T. Saito, and N. Nishizawa, "Dispersion-managed, high-power, Tm-doped ultrashort pulse fiber laser using single-wall-carbon-nanotube polyimide film," OSA Continuum **4**, 137-148 (2021).

192. M. D. Burns, P. C. Shardlow, P. Barua, T. L. Jefferson-Brain, J. K. Sahu, and W. A. Clarkson, "47 W continuous-wave 1726 nm thulium fiber laser core-pumped by an erbium fiber laser," Opt Lett **44**, 5230-5233 (2019).

193. S. T. Xu, T. Lim, A. Turnali, and M. Y. Sander, "High-energy, frequency-doubled thulium-doped fiber chirped-pulse amplification system at 950 nm," Optica **11**, 519-522 (2024).

194. G. J. Spühler, T. Südmeyer, R. Paschotta, M. Moser, K. J. Weingarten, and U. Keller, "Passively mode-locked high-power Nd:YAG lasers with multiple laser heads," Applied Physics B **71**, 19-25 (2000).

195. Q. Lin and I. Sorokina, "High-order dispersion effects in solitary mode-locked lasers: side-band generation," Opt Commun **153**, 285-288 (1998).

196. T. Hasan, Z. P. Sun, F. Q. Wang, F. Bonaccorso, P. H. Tan, A. G. Rozhin, and A. C. Ferrari, "Nanotube-polymer composites for ultrafast photonics," Adv Mater **21**, 3874-3899 (2009).

197. P. Srisamran, I. Abughazaleh, M. Gerard, D. Xu, Y. Jung, J. He, J. Marcellino, B. Mao, A. C. Ferrari, D. Richardson, and L. Xu, "Nanojoule-energy-level, polarization-maintaining,

dissipative-soliton mode-locked thulium fiber laser at 1876 nm," Opt Laser Technol **189**, 112978 (2025).

198. S. Kobtsev, S. Smirnov, S. Kukarin, and S. Turitsyn, "Mode-locked fiber lasers with significant variability of generation regimes," Opt Fiber Technol **20**, 615-620 (2014).
199. M. Michalska, "Dispersion managed thulium-doped fiber laser mode-locked by the nonlinear loop mirror," Opt Laser Technol **138**(2021).
200. C. Cuadrado-Laborde, J. L. Cruz, A. Diez, and M. V. Andres, "Passively modelocked all-PM thulium-doped fiber laser at 2.07 μm," IEEE Photonics J **14**(2022).
201. M. Loch and W. E. Heinlein, "High-resolution measurement of birefringence profiles in stress-induced polarization-maintaining fibers," J Lightwave Technol **7**, 1213-1216 (1989).
202. Y. Zhu, Z. Cui, X. Sun, T. Shirahata, L. Jin, S. Yamashita, and S. Y. Set, "Fiber-based dynamically tunable Lyot filter for dual-wavelength and tunable single-wavelength mode-locking of fiber lasers," Opt Express **28**, 27250-27257 (2020).
203. K. Özgören and F. Ö. Ilday, "All-fiber all-normal dispersion laser with a fiber-based Lyot filter," Opt Lett **35**, 1296-1298 (2010).
204. Y. H. Zhang, Y. Zheng, X. Y. Su, H. W. Zhang, T. R. Sun, M. D. Cui, and J. Y. Peng, "Wavelength tunable all-polarization-maintaining fiber laser at 2 μm," Opt Laser Technol **168**(2024).
205. W. Song, Y. Hou, Q. Zhang, G. Si, Y. Zhang, X. Lu, and P. Wang, "All-polarization-maintaining thulium-doped fiber laser based on nonlinear amplified loop mirror," Proc. SPIE **12501**, 125011B (2022).
206. P. Ciąćka, A. Rampur, A. Heidt, T. Feurer, and M. Klimczak, "Dispersion measurement of ultra-high numerical aperture fibers covering thulium, holmium, and erbium emission wavelengths," J Opt Soc Am B **35**, 1301-1307 (2018).
207. P. Srisamran, I. Abughazaleh, M. D. Gerard, D. Xu, Y. Jung, D. J. Richardson, and L. Xu, "Polarization-maintaining dissipative-soliton mode-locked thulium fiber laser with a nonlinear-amplifying-loop-mirror cavity operating at 1860 nm," Opt Express **33**, 16880-16888 (2025).
208. I. N. Duling, C. J. Chen, P. K. A. Wai, and C. R. Menyuk, "Operation of a nonlinear loop mirror in a laser cavity," IEEE J Quantum Elect **30**, 194-199 (1994).
209. I. N. Duling, "All-fiber ring soliton laser mode-locked with a nonlinear mirror," Opt Lett **16**, 539-541 (1991).
210. S. W. Peng, X. Y. Liu, H. Y. Fu, and Q. Li, "Generation of harmonic mode-locked pulses and noise-like pulses in an all-PM Tm-doped fiber laser via linear-cavity interferometric NPE," Opt Laser Technol **181**(2025).
211. N. J. Doran and D. Wood, "Nonlinear-optical loop mirror," Opt Lett **13**, 56-58 (1988).

212. J. Lin, Z. Zha, H. Liu, J. Zhou, and H. Guo, "Low noise Tm-fiber laser comb via nonlinear amplifying loop mirror," in *2022 Conference on Lasers and Electro-Optics Pacific Rim (CLEO-PR)*, 2022), 1-2.

213. J. Q. Zhou, W. A. Qi, X. Zeng, X. Cheng, H. W. Jiang, S. Z. Cui, and Y. Feng, "All-polarization-maintaining, ultra-compact Tm-doped fiber laser designed for mid-infrared comb," IEEE Photonics Technol Lett **34**, 89-92 (2022).